Modelling and Design Guidelines for Ram Air Ducts Using the Meredith Effect

Applied to an Organic Rankine Cycle Waste Heat Recovery System

L.J. van Dongen

Technische Universiteit Delft

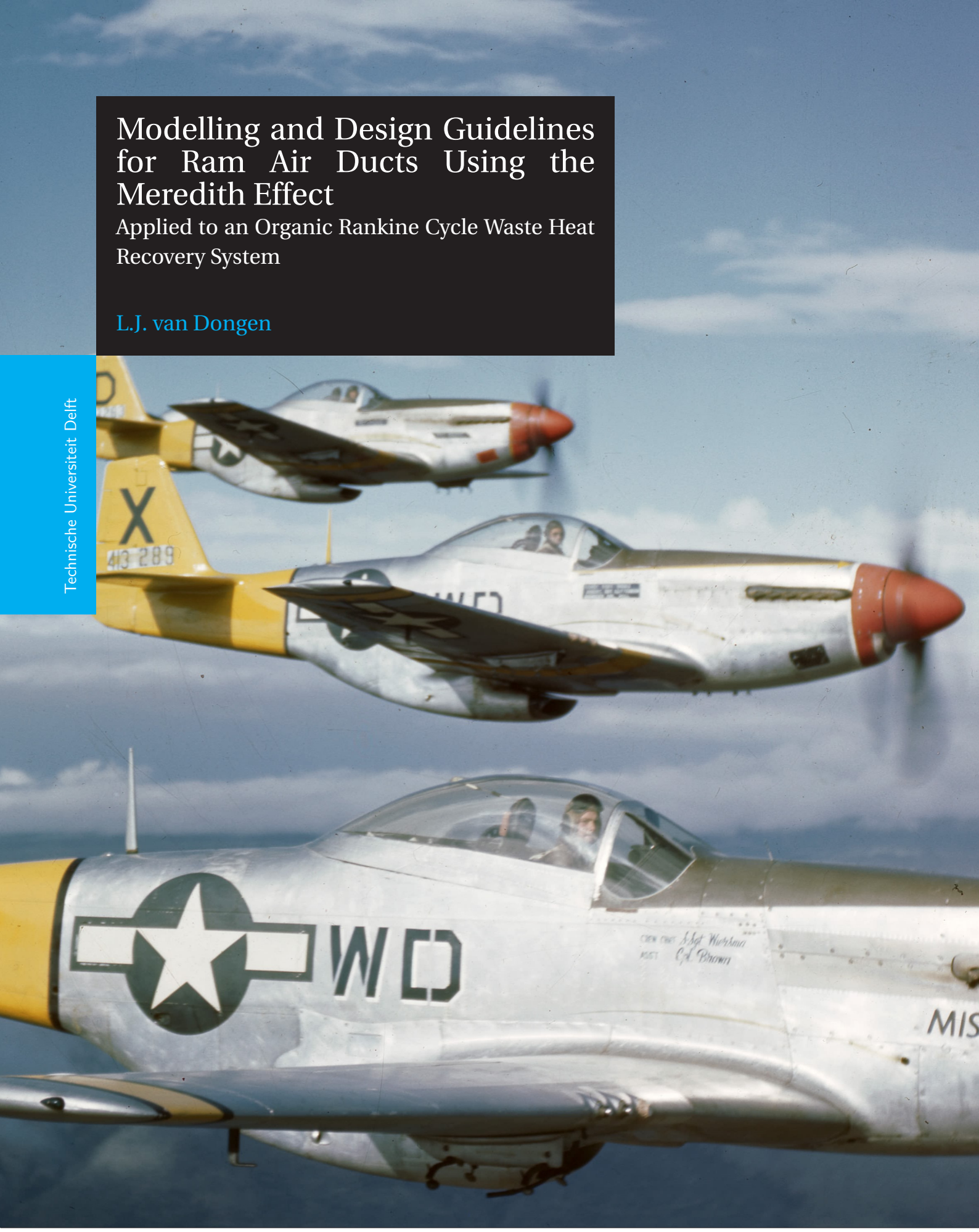

TU Delft Delft University of Technology

Challenge the future

Modelling and Design Guidelines for Ram Air Ducts Using the Meredith Effect

Applied to an Organic Rankine Cycle Waste Heat Recovery System

by

L.J. van Dongen

in partial fulfillment of the requirements for the degree of

Master of Science
in Aerospace Engineering

at the Delft University of Technology,
to be defended publicly on the 24th of May at 9:30.

Supervisor:	Ir. F. Beltrame	TU Delft
Thesis committee:	Dr. I Langella	TU Delft
	Dr. Ir. C. M. de Servi	TU Delft
	Dr. D. Modesti	TU Delft

Cover: Mustang P-51D, 52nd fighter group, 4th fighter squadron [1]. This is also the aircraft which uses the Meredith effect, discovered by F. W. Meredith [2].

An electronic version of this thesis is available at `http://repository.tudelft.nl/`.

TU Delft Delft University of Technology

PREFACE

Dear reader,

This thesis is written in partial fulfilment of my master's degree in Aerospace Engineering. Since the start in 2015, I have grown a lot as a person, not just on the educational front. Looking back, the extracurricular activities were essential in shaping me. Leaving me with new friends and practical experience in engineering. In particular, my time at Forze Hydrogen Racing allowed me to tackle this project better by having improved on critical thinking and organisational skills.

At first, the thesis felt like a means to the end of my educational career, just a box to tick. Luckily, I found a topic that has always been one of my interests in engineering: heat transfer. The topic that is coupled with aerodynamics and thermodynamics combined with an attempt to make the aerospace industry less polluting, changed my view on the task of writing a thesis. In the end, I can look back at a tough but rewarding project, which hopefully will contribute in some way to making aviation sustainable.

First and foremost, I would like to thank you, Fabio, for always being available to help me out whenever or whatever the issue was. In particular, I have appreciated that you made this project feel like a collaboration instead of a solo project. Next to Fabio, I would like to thank you, Carlo, for giving a critical perspective on the research and keeping my nose pointed in the right direction. Next to the "thesis life", there was also a "non-thesis-life". Here, I would like to thank you, Gitte, for supporting me throughout the project and giving advice. I would also like to thank Loulou, Jos, Ruben and Michelle. I would also like to thank my housemates Emile, Senne and Thymen during this year for the joyful lunch breaks, learning about how gold miners provide for their families and learning trivia through watching 2 voor 12. Finally, I would like to express my appreciation to Ruben, who has pushed me to take coffee or lunch breaks with him to talk about other stuff than the thesis.

L.J. van Dongen
Delft, February 2024

SUMMARY

With climate change posing an increasing danger to society, the Advisory Council for Aviation Research and Innovation in Europe (ACARE) has set a target to reduce CO_2 emissions by 75% and NO_x emissions by 90% per passenger kilometre from the aviation sector by 2050 with respect to a baseline aircraft in service in the year 2000 [3]. The **Air**borne **En**ergy Harvesting for **A**ircraft (ARENA) project [4] aims to address this issue by the creation of a waste heat recovery system using the hot exhaust gases of aircraft engines. By harvesting heat energy from otherwise wasted exhaust gases, the fuel consumption of aircraft can be brought down by improved overall efficiency. This thesis, specifically, is focused on integrating the condenser of such a system in the propulsive unit while minimizing the drag associated with the ram air cooling duct. To achieve this, a holistic approach is sought to asses drag recovery performance considering different heat exchanger topologies and duct designs in terms of drag recovery performance.

As a test case, in this thesis, the system will be designed for the **I**nvestigation and **M**aturation **o**f **T**echnologies for **H**ybrid **E**lectric **P**ropulsion (IMOTHEP) **D**istributed fans **R**esearch **A**ircraft with electric **G**enerators by **ON**ERA (DRAGON) concept, a hybrid electric aircraft concept using two turbogenerators mounted at the tail.

Historically, when aircraft propellers were driven by internal combustion engines, thermal management systems were required to keep engine temperatures low. Meredith demonstrated that with well-designed ducting, integrating a heat exchanger could produce thrust [2]. The advent of gas turbine propulsion alleviated concerns regarding waste heat rejection, as the majority of heat in a Brayton cycle is dissipated into the surrounding air [5]. Now, with the rise of more electric aircraft, geared turbofans, and hybrid electric aircraft, renewed attention is being directed towards this issue.

The literature study revealed several significant findings. Firstly, an examination of the Meredith effect highlighted the benefits of aiming for high pressure to enhance thermodynamic efficiency. However, achieving these high pressures comes at the cost of losses and spatial requirements due to non-ideal diffusive components. This observation was supported by an investigation into the pressure drop of a heat exchanger, which demonstrated that lower velocities predominantly result in reduced pressure drops. Additionally, employing porous media modelling to simulate a heat exchanger in computational fluid dynamics was found to be an effective strategy for reducing computational costs. Furthermore, considering that the Meredith effect performs optimally at high-pressure ratios, the scoop-type or ram air intake was identified as the preferred intake design. Lastly, based on considerations of drag and pressure recovery, the optimal intake location was determined to be at the front of the aircraft's belly, resembling the placement of current environmental control system intakes in modern civil aircraft.

These findings fund the rationale of seeking a holistic approach in ducted heat exchanger integration with the objective of drag recovery using the Meredith effect to answer:

> **What is the optimal design for the ram air duct accommodating the condenser of a waste heat recovery system for the IMOTHEP DRAGON concept main engines?**

To address this question, the work is divided into multiple stages. Firstly, an investigation is conducted to determine if a multipass-condenser can reduce pressure drop. The rationale behind this is that adjusting the heat exchanger blockage factor per longitudinal pass offers the potential to regulate flow acceleration caused by heating. Additionally, it can accommodate condensation occurring on the working fluid side, moderating the extremes of working fluid velocity by adjusting the flow area. However, when analysing the results, the hypothesis did not yield any reduction in pressure drop.

Secondly, a lumped parameter model is developed to characterize drag, pressure drop, temperature increase, and length of the ram air duct. This model is used to investigate the sensitivity of the ram air duct geometrical parameters on the drag recovery factor and ram air duct length. Where the drag recovery factor is a

dimensionless number indicative of net positive or net negative thrust. The sensitivity study highlighted that inclining the heat exchanger is the most space-efficient way of increasing the drag recovery factor, while the diffuser area ratio has a similar effect but is less space-efficient. Furthermore, it is found that the mass flow rate ratio has a smaller sensitivity to the drag recovery factor compared to the diffuser area ratio and heat exchanger inclination angle. The smallest sensitivity on the drag recovery was found to be the fin height or dimensional pitch of the heat exchanger.
Subsequently, the lumped parameter model was used to find an optimal preliminary design of the ram air duct for varying spatial constraints. This analysis is performed for different heat exchanger types to determine which heat exchanger type has the highest drag recovery factor. Next to this, the analysis is performed for varying diffuser-blocked area fractions to inspect the effect of an ingested boundary layer. The combined results revealed that the inline plain tube bundle and flat tube offset strip fin heat exchangers yield a more compact solution and attain higher drag recovery factors than other considered heat exchanger types. Furthermore, it was found that for reasonably large diffuser-blocked area fractions, the optimal ram air duct geometry was independent of heat exchanger type. Moreover, the optimal duct geometry for reasonably large diffuser-blocked area fractions can be characterized by utilizing a maximum inclination angle of 70 degrees, maintaining a mass flow rate ratio of 0.7, and maximizing the diffuser area ratio within spatial constraints.

Thirdly, a verification study of the lumped parameter model was performed by setting up a two-dimensional Reynolds Averaging Navier Stokes (RANS) computational fluid dynamics (CFD) analysis. This numerical simulation uses the k-ω SST turbulence in combination with a porous zone to mimic the presence of the heat exchanger. The numerical simulation was performed for the found optimal ram air duct geomtry with a maximum length of 3 meters. The results revealed that for the optimal duct geometry, both models predicted a positive drag recovery factor with a difference of 0.8%. Next to this, the numerical simulation was performed for multiple ram air duct geometries with varying diffuser area ratios, mass flow rate ratios and heat exchanger inclination angles. Across this dataset, the mean absolute difference in drag recovery factor between the two models amounted to 1.082%, with a standard deviation of 0.584%.

Considering all the findings, it can be concluded that the lowest net drag of a condenser integration results in a positive thrust within the specified space constraints, thus reviving Meredith's claim from 1935 [2].

List of Figures

List of Tables

NOMENCLATURE

Roman letters

ΔA_i	Surface area of a cell
$\dot{m}$	Mass flow
$\dot{m}/\dot{m}_0$	Mass flow rate ratio
$\hat{\mathbf{y}}$	Guess vector
$\mathbf{D}$	Viscous resistance coefficient matrix
$\mathbf{F}$	Inertial resistance coefficient matrix
$\mathbf{M}$	Coupling matrix Cell Method
$\mathbf{R}$	Thermal resistance
$\mathbf{T}$	Temperature vector
$\mathbf{x}$	Design vector
A	Area
a	Correlation coefficient Nusselt number
A_B	Blocked area
A_E	Effective area
A_o	Minimum free flow area
a_{xt}	Adimensional pitch
AR	Diffuser area ratio
B	Blocked area fraction
C	Heat capacity rate ($\dot{m}C_p$)
C^*	Heat capacity rate raio
C_a	Angularity coefficient
C'_D	Drag coefficient at zero inlet mass flow, excluding skin friction and diverter drag
C_f	Skin friction parameter ($\tau_w/(\rho u_E^2/2)$)
c_F	Form drag coefficient
C_p	Isobaric specific heat
C_p^*	Optimal pressure recovery coefficient for given non-dimensional length
C_p^{**}	Optimal pressure recovery coefficient for given area ratio
C_v	Velocity coefficient
C_{Dd}	Diverter drag
C_{Dffull}	Datum drag
C_{DF}	Skin friction drag
C_{Dsc}	Drag coefficient of scoop inlet
C_{ds}	Discharge coefficient
C_{fg}	Thrust coefficient
$C_{p,i}$	Ideal pressure recovery coefficient
C_p	Pressure recovery coefficient
$CD_{k\omega}$	Cross-diffusion term
$d()$	Differential parameter
$D(M)$	Compressible flow function (Eq. 2.9)
D_{eq}	Hydraulic diameter
d_H	Hydraulic diameter ($4A$/perimiter)
$d_{1,l}$	Lower highlight height
$d_{1,u}$	Upper highlight height
D_{sc}	Total drag produced by scoop intake (including ram drag)
DRF	Drag recovery factor
E	Effective area fraction, Energy
e_a^{21}, e_a^{32}	Approximate relative error
$e_{\text{fine}}^{21}, e_{\text{fine}}^{32}$	Fine-grid convergence index
$e_{ext}^{21}, e_{ext}^{32}$	Extrapolated relative error
F	Correction factor for LMTD method
f	Fanning friction factor (Eq. 3.10)
F_1	Blend function SST turbulence model
F_2	Blend function SST turbulence model
F_s	GCS safety factor
F_{nozzle}	Total thrust produced by the nozzle
$f_{ext}^{21}, f_{ext}^{32}$	Richardson extrapolate
G	Mass flow rate per unit area (mass flux)
g	Gravity
H	Height
h	Heat transfer coefficient, enthalpy, representative grid size
h_{fin}	Fin height
J_i	Diffusion flux of species i

K	Specific permeabillity
k	Thermal conductivity, turbulent kinetic energy
K_c	Contraction loss coefficient at heat exchanger entrance
K_e	Expansion loss coefficient at heat exchanger exit
k_f	Correction factor for effect of smooth shaped inlet lip
k_h	Hydraulic conductivity
k_p	Correction factor for total pressure recovery with Mach number
K_{sc}	Momentum flow correction factor scoop inlet
k_{spsc}	Correction factor for effect of massflow on spillage drag
L	Length, convergence factor
l_β	Void pore length scale
l_σ	Solid pore length scale
l_H	Maximum REV
m	Correlation coefficient Nusselt number
m	Mass
N	Length of the diffuser in Sovran and Klomp [17]
N	Number of cells
n	Correlation coefficient Nusselt number
Nu	Nusselt number
P	Pressure
P	Temperature effectiveness
p	Pressure, order of convergence
Pr	Prandtl number
Q	Volume flow rate
q	Heat flux, dynamic pressure
Q_{duty}	Heat duty
R	Gas constant
r	Relaxation factor
r_0	Minimum REV
r_f	Fouling factor
r_h	Hydraulic radius ($D_H/2$)
r_{12}, r_{23}	Refinement factor
Re	Reynolds number
S	Surface density
s	Entropy
S_e	Energy source term
S_m	Momentum source term
T	Temperature
t	Thickness
t	Time
u	Velocity
U, U_m	Overal heat transfer coefficient
V	Volume, Velocity
v	Specific volume, velocity
W	Width
W	height of the diffuser in Sovran and Klomp [17]
x	X coordinate/direction
Y	Height in Y direction

Greek letters

$(1/\rho)_m$	Mean specific volume w.r.t. flow length (Eq. 3.11)
α_d	Nozzle half angle
β	void space
β_1	Surface density of plate(-fin) heat exchangers (Eq. 3.1)
β_2	Surface density of (shell-and-)tube(-fin) heat exchanger (Eq. 3.2)
Δ	Difference
δ	(Boundary layer) thickness
δ^*	Boundary layer displacement thickness
δ_{ij}	Kronecker delta
ϵ	Effectiveness
$\epsilon_{12}, \epsilon_{23}$	Difference between numerical solution
η_0	Fin efficiency
η_σ	Pressure recovery from [20]
η_P	Total pressure ratio

$\eta_{\sigma,i}$	Ideal pressure recovery from [20]
η_{thermal}	Thermal efficiency
η_{p_t}	Total pressure ratio nozzle
γ	Specific heat ratio
γ_m	Mass-weighted uniformity index
μ	Dynamic viscosity
ν	Kinematic viscosity
ω	Turbulent specific dissipation
$\overline{\overline{\tau}}$	Deviatoric stress tensor
$\overline{\overline{\mathscr{E}}}_0$	Diffuser effectiveness
ϕ	Arbitrary quantity
Ψ	Momentum flow, Thermodynamic state
ρ	Density
σ	Heat exchanger blockage factor, solid matrix
τ_{ij}	Reynolds stress term
θ	Boundary layer momentum thickness, inclination angle, diffuser half angle in Sovran and Klomp [17]
ε	Porosity
ζ_μ	Dynamic viscosity correction coefficient
ζ_C	Form drag correction coefficient
M	Mach number

Sub- and Superscripts

0	free stream value in ESDU Data item 86002 [14]
1	Inlet station diffuser Sovran and Klomp [17]
2	Outlet station diffuser Sovran and Klomp [17]
$\bar{\phi}$	Average value of arbitrary quantity
β	void space
∞	Free stream conditions
$\phi^{(0)}$	Inital value of arbitrary variable
ϕ^*	Final value of arbitrary variable
σ	solid matrix
eff	Effective
sc full	Scoop inlet running at mass flow rate ratio of 1
$\vec{\phi}$	Denotes a vector of an arbitrary quantitiy
alu	Aluminium
c	Cold side, captured
D_{eq}	Hydraulic diameter
e	Effective
f	fouling
h	Hot side
hex	Heat exchanger
i	Inlet, ideal
in	Inlet condition
lm	Logarithmic Mean
loc	Local
m	Mean
m	mean value
mag	Magnitude
max	Maximum
min	Minimum
o	Overall, outlet
out	Outlet condition
pl	flat plate
ref	Reference
s	Static
sc	Scoop
sh	sharp lips
t	Total, turbulent
t,t	Total condition at throat of the inlet
Tu	Theoretical value lower highlight
Tu	Theoretical value upper highlight
w	Wall

Abbreviations

ACARE	**A**dvisory **C**ouncil for **A**viation **R**esearch and Innovation in **E**urope
ARENA	**Air**borne **En**ergy Harvesting for **A**ircraft
CFD	**C**omputational **F**luid **D**ynamics
DLR	**D**eutsches Zentrum für **L**uft- und **R**aumfahrt
DP	**D**esign **P**oint

DPM **D**etailed **P**hysics **M**odel

DRAGON **D**istributed fans **R**esearch **A**ircraft with electric **G**enerators by **ON**ERA

ECS **E**nvironmental **C**omtrol **S**ystem

ESDU **E**ngineering **S**ience **D**ata **U**nit

FTLF **F**lat **t**ube microchannel **l**ouvred **f**in

FTOSF **F**lat **t**ube microchannel **o**ffset **s**rip **f**in

FV **F**inite **V**olume

GCI **G**rid **c**onvergence **i**ndex

GCS **G**rid **c**onvergence **s**tudy

IMOTHEP **I**nvestigation and **M**aturation **o**f **T**echnologies for **H**ybrid **E**lectric **P**ropulsion

LMTD **L**ogarithmic **m**ean **t**emperature **d**ifference

LPM **L**umped **P**arameter **M**odel

MB **M**oving **B**oundary

MDA **M**ulti-**D**isciplinary **A**nalysis

MDF **M**ulptiple **D**iscipline **F**easible

MTD **M**ean **t**emperature **d**ifference

NTU **N**umber of **t**ransfer **u**nits

ORC **O**rganic **R**ankine **C**ycle

PTBI **P**lain **T**ube **B**undle **I**nine

PTBS **P**lain **T**ube **B**undle **S**taggered

RANS **R**eynolds **A**veraging **N**avier **S**tokes

REV **R**epresentative **E**lementary **V**olume

XDSM E**x**tended **D**esign **S**ructure **M**atrix

CONTENTS

1

INTRODUCTION

With climate change posing an increasing danger to society, the Advisory Council for AviationResearch and Innovation in Europe (ACARE) has set a target to reduce CO_2 emissions by 75% and NO_x emissions by 90% per passenger kilometre from the aviation sector by 2050 with respect to a baseline aircraft in service in the year 2000 [3]. While thermal efficiencies of aero-engines have risen significantly in the past years by about 1.3% in terms of fuel burn per passenger kilometre, the increase was mostly governed by an increase in the overall pressure ratio, turbine inlet temperature, component efficiencies and higher bypass ratios as mentioned in Yin and Rao [21]. These steps forward are encountering material limits, as well as an increase in NO_x emissions given by higher turbine inlet temperatures. Therefore, growing forward in this direction is not an option, calling for new innovative solutions to decrease emissions. The **Air**borne **En**ergy Harvesting for **A**ircraft (ARENA) project [4] aims to address this issue by the creation of a waste heat recovery system using the hot exhaust gases of aircraft engines. By harvesting heat energy from exhaust gases, aircraft fuel consumption can be reduced by improved overall efficiency. The waste heat will be recovered using an Organic Rankine cycle, as shown in Figure 1.1. The thermal energy of the exhaust gases is recovered by an evaporator, energy is extracted in a turbine, and the working fluid is condensed using a condenser and finally to complete the cycle the working fluid passes through a pump raising the pressure.

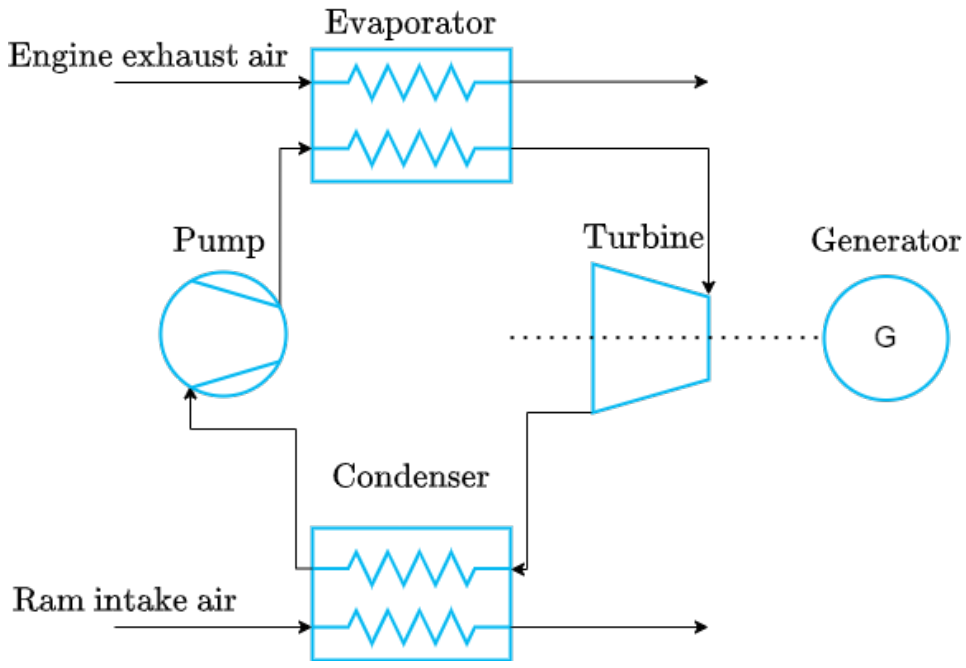

Figure 1.1: Schematic representation of the waste heat recovery system

This cycle, most conventionally known as a Rankine cycle, has been used extensively for converting thermal energy into shaft work using water/steam as a working fluid. More recently, Organic Rankine cycles have started to emerge, where the name is due to the fact that the working fluid in the cycle is organic, having different thermophysical properties to water. These systems excel at recovering heat from medium-low temperature heat sources, require low maintenance costs and operate at favourable operating pressures [22]. While organic Rankine cycles are considered a mature technology [22], they are not yet used in aviation. In fact, where Lecompte et al. [22] delineate focus areas for optimizing an ORC waste heat recovery system, aspects such as weight, compactness, volume, and their correlation with pressure drop, pivotal for airborne applications, remain unaddressed.
Therefore, the ARENA project aims to fill these knowledge gaps [4]. The project focuses on three work packages, namely, System modelling and performance, heat exchangers and the organic Rankine cycle turbomachinery.
This thesis addresses part of the second work package objective, namely the integration of the condenser into the aircraft propulsion unit. It employs a holistic approach to assess drag implications by examining heat exchanger topology and exploiting the Meredith effect for drag recovery [2]. As a test case, in this thesis, the system will be designed for the **I**nvestigation and **M**aturation **o**f **T**echnologies for **H**ybrid **E**lectric **P**ropulsion (IMOTHEP) **D**istributed fans **R**esearch **A**ircraft with electric **G**enerators by **ON**ERA (DRAGON) concept, a hybrid electric aircraft concept using two turbogenerators mounted at the tail as seen in Figure 1.2 to generate power for the electric distributed propulsion system situated in the wing.

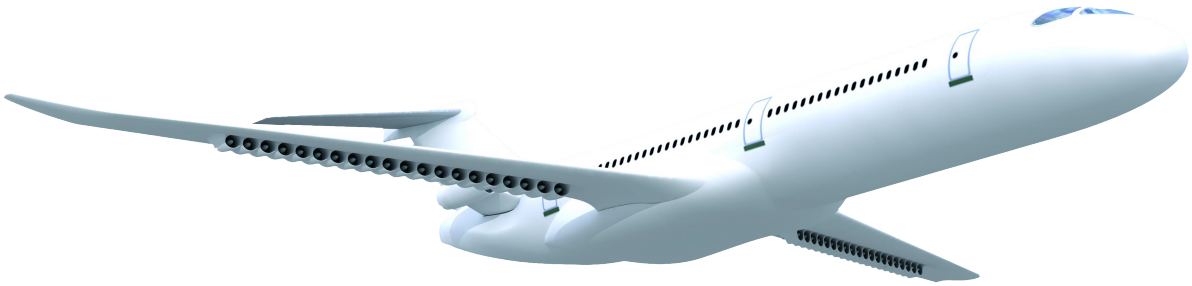

Figure 1.2: DRAGON concept of the IMOTHEP project [6]

The top-level requirements, as well as the mid-cruise condition for the DRAGON concept, are listed in Table 1.1 [23]. These requirements are used throughout the literature study to narrow the scope of the research to present the most relevant literature possible.

Top-level parameters			Mid Cruise conditions		
Range	2750	NM	Altitude	10000	m
Number of Passengers	150		Mach number	0.78	
Design Payload	13608	kg	Power requirement	7	MW
Span limit	36	m	Exhaust gas temperature	640	K

Table 1.1: Operating conditions and top-level requirements for the ONERA DRAGON concept

I

STATE OF THE ART

2

MEREDITH EFFECT MODELLING

The Meredith effect, first described by F. W. Meredith in 1935 [2], is an effect where the integration of a heat-rejecting radiator into a ram air duct produces thrust instead of a drag penalty. This was particularly applicable in piston-engine aircraft where the temperatures in the radiator were high. Meredith showed that with well-designed ducting, it is possible to convert rejected heat into thrust. Göthert [24] similarly investigated the advantages of ducted radiators.

For a long period after Meredith's [2] and Götherts [24] contribution, not much research was devoted to this. As Kellermann et al. [5] mention, with the introduction of gas turbine propulsion, the interest in thermal management decreased. This is because, in an open Brayton cycle, waste heat is rejected into the atmosphere. Today, with increasing research being devoted to more electric aircraft (MEA), geared turbofans, hybrid electric aircraft, and fully electric aircraft, there is a need for components cooling onboard, often at relatively low temperatures. This is raising again interest in the low-drag integration of heat exchangers [5] [25]. A way to fulfil this need is through the Meredith effect as recognized by more recent contributions [5], [26], [27], [28].

To address the Meredith effect, first, the behaviour of a heated flow in a constant cross-section pipe with friction is presented in Section 2.1. Here, it is shown that with friction and heat addition, the total pressure decreases and that only with heating does the total temperature increase. Next, the thermodynamic perspective on the Meredith effect is presented by drawing the analogy with the Brayton cycle in Section 2.2, revealing that a high-pressure ratio in the diffuser is favourable for thermodynamic efficiency. Finally, methodologies for modelling ram air ducts are compared in section 2.3.

2.1. HEATED FLOW IN A CONSTANT CROSS-SECTION PIPE WITH FRICTION

This section illustrates the physical phenomena involving a flow in a pipe in the case of heat addition and subjected friction, utilizing a quasi-one-dimensional model described in the book "Internal Flow: Concepts and Applications" by Greitzer et al. [29].

The assumptions made by Greitzer et al. [29] are the following: The flow is assumed to be a perfect gas with constant specific heats, c_p, c_v, while the skin friction coefficient, C_f, is that of circular ducts as described by White [15]. Figure 2.1 gives a schematic view of the control volume considered used for the derivation of the model. In this figure, dq, is the added heat, dx, is the length of the control volume and, d_H, is the hydraulic diameter and is defined as $d_H = 4A/\text{wetted perimeter}$. Finally, the flow is assumed to be compressible. The other variables are the specific heat ratio, γ, mach number, M, total pressure, p_t, total temperature, T_t, static temperature, T, static pressure, p and density, ρ.

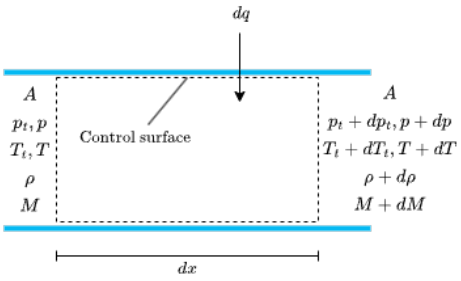

Figure 2.1: Control volume for constant area duct with heat addition

The variation of M, ρ, p, p_t, T and T_t in the duct is described by the following equations from Greitzer et al. [29]. The influence coefficients are multiplied by their respective independent variables. These equations are a function of two independent terms. The specific heat addition, $dq/(c_p T_t)$, and the friction term, $4C_f dx/d_H$. Considering low subsonic flow, Equation 2.1 shows that both heat addition and friction increase the Mach number. Consistently with what occurs in Rayleigh and Fanno flow.

$$\frac{dM^2}{M^2} = \frac{\left(1+\frac{\gamma-1}{2}M^2\right)\left(\gamma M^2+1\right)}{1-M^2}\frac{dq}{c_p T_t} + \frac{\gamma M^2\left[1+\frac{\gamma-1}{2}M^2\right]}{1-M^2}4C_f\frac{dx}{d_H} \tag{2.1}$$

On the other hand, Equation 2.2, shows that the total pressure has an opposite trend with respect to heat and friction.

$$\frac{dp_t}{p_t} = -\frac{\gamma M^2}{2}\frac{dq}{c_p T_t} - \frac{\gamma M^2}{2}4C_f\frac{dx}{d_H} \tag{2.2}$$

The total temperature is only influenced by heat addition shown in Equation 2.3.

$$\frac{dT_t}{T_t} = \frac{dq}{c_p T_t} \tag{2.3}$$

The density, shown in Equation 2.4, shows a decreasing trend with friction and heat addition.

$$\frac{d\rho}{\rho} = -\frac{1+\frac{\gamma-1}{2}M^2}{1-M^2}\frac{dq}{c_p T_t} - \frac{\gamma M^2}{2(1-M^2)}4C_f\frac{dx}{d_H} \tag{2.4}$$

Equations 2.5 and 2.6 show that the static temperature and static pressure decrease with heating and friction.

$$\frac{dT}{T} = -\frac{\left(1+\frac{\gamma-1}{2}M^2\right)\left(\gamma M^2-1\right)}{1-M^2}\frac{dq}{c_p T_t} - \frac{\gamma M^4(\gamma-1)}{2\left(1-M^2\right)}4C_f\frac{dx}{d_H} \tag{2.5}$$

$$\frac{dp}{p} = -\frac{\gamma M^2\left(1+\frac{\gamma-1}{2}M^2\right)}{1-M^2}\frac{dq}{c_p T_t} - \frac{\gamma M^2\left[1+(\gamma-1)M^2\right]}{2\left(1-M^2\right)}4C_f\frac{dx}{d_H} \tag{2.6}$$

Greitzer et al. [29] present Equation 2.7, which relates the corrected mass flow change, $\dot{m}\sqrt{T_t}/(Ap_t\sqrt{\gamma})$, to changes in mass flow, $\frac{d\dot{m}}{\dot{m}}$, total temperature, $\frac{dT_t}{2T_t}$, area, $\frac{dA}{A}$, and total pressure, $\frac{dp_t}{p_t}$. This equation holds true only for small variations in these variables. It illustrates that the increase in corrected mass flow is directly proportional to the addition of mass flow and the rise in total temperature, while inversely proportional to changes in area and total pressure.

$$\frac{d[\dot{m}\sqrt{T_t}/(Ap_t)]}{[\dot{m}\sqrt{T_t}/(Ap_t)]} = \left(\frac{d\dot{m}}{\dot{m}} + \frac{dT_t}{2T_t} - \frac{dA}{A} - \frac{dp_t}{p_t}\right) \tag{2.7}$$

In the case of pipe-flow, the corrected mass flow is solely influenced by the changes in total temperature and total pressure. Combining these observations, the adjusted expression for the corrected mass flow in terms

of heat additions and friction is given by Equation 2.8. From this it can be observed that heat addition to the flow and exerted friction on the flow both increase the corrected mass flow.

$$\frac{d[\dot{m}\sqrt{T_t}/(Ap_t)]}{[\dot{m}\sqrt{T_t}/(Ap_t)]} = \left(\frac{dq}{2c_pT_t} + \frac{\gamma M^2}{2}\frac{dq}{c_pT_t} + \frac{\gamma M^2}{2}4C_f\frac{dx}{d_H}\right) \tag{2.8}$$

Coupling this with the definition of corrected mass flow shown in Equation 2.9 and plotted in Figure 2.2, it can be seen that an increase in corrected mass flow corresponds drives the Mach number to unity.

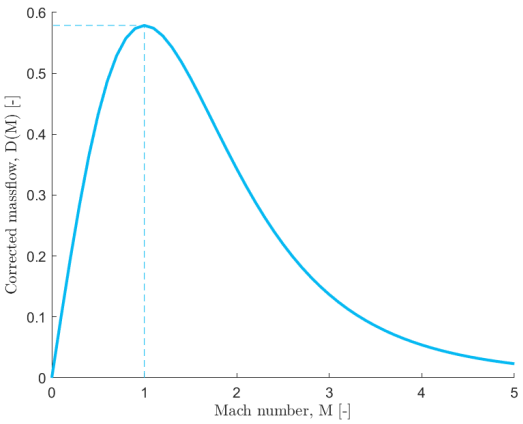

$$D(M) = \frac{\dot{m}\sqrt{RT_t}}{Ap_t\sqrt{\gamma}} = \frac{M}{\left(1+\left(\frac{\gamma-1}{2}\right)M^2\right)^{\frac{\gamma+1}{2(\gamma-1)}}} \tag{2.9}$$

Figure 2.2: Corrected mass flow versus Mach number for $\gamma = 1.4$

Based on the explanation above, Table 2.1 shows what would happen to flow in a heat exchanger in a qualitative manner.

	Heat addition	Friction
p_t	↓	↓
T_t	↑	-
p	↓	↓
T	↓	↓
M	↑	↑
ρ	↓	↓
$D(M)$	↑	↑

Table 2.1: Influence of heat and friction on constant area pipe model for low subsonic flow

2.2. THE THERMODYNAMIC PROCESS

Figure 2.3 illustrates the thermodynamic process associated with the flow in the ram air duct housing a heat exchanger.

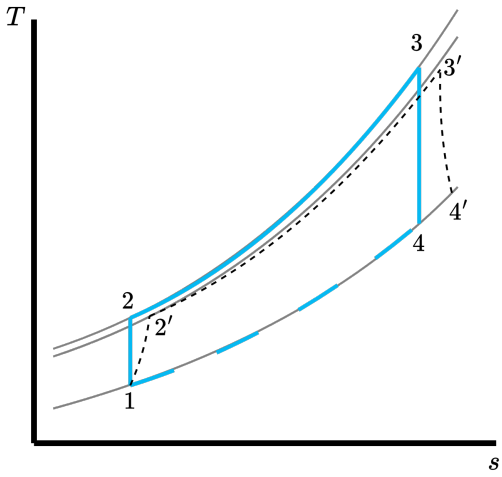

Figure 2.3: T-s diagram of the Brayton or Joule cycle

With reference to the ideal cycle efficiency shown in blue in Figure 2.3, it is possible to define the ideal cycle efficiency as in Equation 2.10. Using the assumption of constant specific heat, the definition is simplified to the term on the right-hand side of Equation 2.10. Moreover, using the same assumption in combination with the observation that processes 1-2 and 3-4 occur between the same isobars, it is possible to establish Equations 2.11 and 2.12. These equations further simplify the thermodynamic efficiency to Equation 2.13. This derivation is presented in more detail in Chapter 9 of Moran et al. [30].

$$\eta_{thermal} = \frac{(h_3 - h_4) - (h_2 - h_1)}{(h_3 - h_2)} = 1 - \frac{T_4 - T_1}{T_3 - T_2} \tag{2.10}$$

$$T_2 = T_1 \left(\frac{p_2}{p_1}\right)^{\frac{\gamma-1}{\gamma}} \tag{2.11}$$

$$T_4 = T_3 \left(\frac{p_4}{p_3}\right)^{\frac{\gamma-1}{\gamma}} = T_1 \left(\frac{p_2}{p_1}\right)^{\frac{\gamma-1}{\gamma}} \tag{2.12}$$

$$\eta_{\text{thermal}} = 1 - \frac{1}{p_2/p_1^{\frac{\gamma-1}{\gamma}}} \tag{2.13}$$

Increasing the pressure ratio over the duct thus improves the ideal efficiency and raises the heat exchanger inlet temperature. The objective is to transfer heat away from the working fluid, so the air side must remain cooler than the working fluid. This imposes a theoretical limit on the pressure ratio across the ram air duct. Nevertheless, for the application of interest in this study, this constraint is not critical as the working fluid temperature is sufficiently higher than the total temperature of the ram air.

The actual process contains irreversibility and is depicted in dashed black lines in Figure 2.3. Due to irreversibilities the process 1-2' arrives at a lower isobar. Subsequently, the flow undergoes heating between stations 2' and 3' in combination with pressure losses. Finally, the flow expands in the nozzle during process 3'-4', arriving at atmospheric pressure at a higher temperature due to entropy generation.

The implications are that, ideally, when arriving at station 3', there should be enough momentum left in the flow to expand and accelerate back to the same or higher freestream velocity to offset drag created by the system. To achieve this, it is recommended to have the highest possible pressure recovery and as little pressure losses in the duct.

2.3. MODELLING THE MEREDITH EFFECT

This section provides an overview of literature modelling ram air ducts with explicit reference to the Meredith effect. Table 2.2 presents the various publications that investigate this effect together with information on

Author	Drela [27]	Schiltgen et al.[26]	Kellerman et al. [5]	Scocciomarro [31]
Year	1996	2016	2021	2023
Inlet	2D CFD	Semi-empirical method with additive drag for high speed condition. [32]	Semi-empirical method [33] [34]	Semi-empirical method by ESDU report 86002 [14]
Diffuser		Semi-empirical method with nominal pressure ratio and adjusted pressure ratio for takeoff and low speed conditions [35], [36]	Semi-empirical method from Pittaluga [37]	Semi-empirical method by Sovran and Klomp [17]
Heat Echanger tilt	-	-	-	semi-emperical method by Nichols [19]
Heat Exchanger	Enthaply increase in the ram air with a check on outlet temperature not being higher than the specified coolant temperature	Thermal resistance analysis and ϵ-NTU method. Aerother-modynamics modelled with general 1D compressible flow equations. [7][38]	ϵ-NTU method, Core mass velocity equation from Shah and Sekulic [7] and data from Kays and London [39]	ϵ-NTU method using [7], with inlet and outlet pressure drop contribution neglected
Nozzle	2D CFD		Semi-empirical from [40]	Isentropic relation with no losses

Table 2.2: Modelling of ram air ducts by publications considering the Meredith effect

how the individual components of the ducted heat exchanger were modelled. The components are the inlet, diffuser, heat exchanger and nozzle. In addition, it is specified whether the heat exchanger is tilted or not. Notably, most of the publications model the heat exchanger using the $\epsilon - NTU$ method. Additionally, only one publication considers heat exchanger tilt. In the case of Schiltgen et al. [26] and Kellerman et al. [5], the analysis of the heat exchanger ducting is part of a larger multidisciplinary optimization of a hybrid electric aircraft. Drela [27] conducted research focusing on high-altitude piston-powered aircraft, aiming to investigate the interaction between an airfoil and an aft or front-mounted radiator on the wing.

Drela [27] draws general recommendations for the design of the radiator core geometry and conclusions regarding the relation between pressure loss and as well as between heat transfer and drag. More in detail, Drela [27] uses dimensionless groups to assess the effect of heat transfer and friction on the flow with respect to the heat exchanger depth, shown in Equations 2.14, 2.15 and 2.16. The equations use definitions of average friction coefficient, C_f, Stanton number, St, and hydraulic radius, r_h, found in more detail in his publication [27]. Other variables include the Prandtl number, Pr, dynamic viscosity at the inlet, μ_1, density at the inlet, ρ_1, velocity at the inlet, V_1, and passage length, l. Variable σ denotes the heat exchanger blockage factor and is defined as the ratio between the passage area in the heat exchanger core and the frontal area of the core. Using this, it is shown that from a certain heat exchanger depth or passage length, heat rejection begins to decrease while pressure losses due to friction continue to increase, setting a practical upper limit to the heat exchanger depth. This cut-off point is characterized by entrance flow length, namely the length after which the flow is fully developed. Furthermore, Drela [27] states that a scaled passage length of $\xi \simeq O(1)$ functions as a good balance between the frontal area of the heat exchanger and the pressure drop over the heat exchanger.

$$K_f = \frac{C_f}{2}\left(\frac{\rho_1 V_1 l}{\sigma \mu_1}\right)^{1/2} \quad (2.14) \qquad K_h = St\,\mathrm{Pr}^{2/3}\left(\frac{\rho_1 V_1 l}{\sigma \mu_1}\right)^{1/2} \quad (2.15) \qquad \xi^2 \equiv \frac{l}{r_h}\frac{\sigma}{\mathrm{Pr}}\frac{\mu_1}{\rho_1 V_1 r_h} \quad (2.16)$$

The relation between pressure loss and drag, Equation 2.17 [27] relates the drag of the heat exchanger core to the pressure drop over the heat exchanger and the ramjet thrust, the first and second terms on the right-hand side of the equation, respectively. In this equation, $\dot{H}$, is the heat transfer rate and P, the acceleration term defined as $2[(V_2/V_1) - 1]]$. Subscript ∞ denotes the freestream condition, and subscript 1 denotes the

heat exchanger inlet station. The relation elucidates that the ram jet thrust is proportional to $\dot{H}M_\infty^2$, which is constrained by the required heat duty to reject and free stream Mach number. This shows that creating a ram air duct with no drag penalty is about efficiently introducing the thermal energy to the flow. An important connotation here is that other sources of pressure loss and drag in the ram air duct are neglected in this relation.

$$D_{\text{core}}\, V_\infty \simeq \frac{\dot{m}}{2} V_\infty^2 P \left(\frac{V_1}{V_\infty}\right)^2 - \dot{H}\frac{\gamma-1}{2}M_\infty^2 \tag{2.17}$$

Equation 2.18 [27] expresses the relation between heat transfer and drag for a heat exchanger with $\xi \simeq O(1)$ as a function of the aforementioned dimensionless group (Equations 2.14,2.15,2.15), the heat exchanger temperature T_r, velocity ratio V_1/V_∞ and heat exchanger blockage factor, σ. Using this relation, Drela [27] quantifies the benefits of ensuring a high deceleration from freestream to heat exchanger inlet velocity, a heat exchanger having relatively low skin friction coefficient, K_f, compared to the heat transfer coefficient K_h, a near unity heat exchanger blockage factor σ and using a high heat exchanger temperature T_r.

$$D_{\text{core}}\, V_\infty \simeq \dot{H}\left[\frac{V_\infty^2 Pr^{2/3}}{c_p\,(T_r - T_1)}\frac{1}{\sigma^2}\frac{K_f}{K_h}\left(\frac{V_1}{V_\infty}\right)^2 - \frac{\gamma-1}{2}M_\infty^2\right] \tag{2.18}$$

Related to the velocity ratio V_1/V_∞, Schiltgen et al. [26] found that the diffuser area ratio and heat exchanger inlet Mach number were important parameters in their optimisation study of a ducted radiator. The first parameter in their study was defined as the ratio between the inlet area and the heat exchanger frontal area. The second parameter, the area ratio of the nozzle is independently controlled by a variable exit area nozzle. The combination of the two parameters defined the split between compression happening by pre-diffusion and the diffuser, where the compression occurring in the pre-diffusion attributes to the drag of the duct. With a weighted objective function including drag of the ram air duct, weight of the duct and pump power required for recirculating the coolant, a diffuser area ratio of ~ 0.3 and heat exchanger inlet Mach number of 0.1 were found to be optimal in the on design condition of their study.

Kellerman et al. [5] performed a sensitivity study on the thermal management system of hybrid electric. In their study, they parameterized the ram air duct, amongst other parameters, with the pressure ratio over the heat exchanger,Π_c and hot side hydraulic diameter $d_{H,h}$. Here, Π_c controls the duct geometry by adjusting the amount of pre-diffusion and diffuser area ratio, which results in a change in heat exchanger inlet velocity and, subsequently, a change in pressure drop over the heat exchanger. For lower Π_c the ram air duct exhibited an increase in drag from the baseline value in combination with a decrease in system weight. For higher Π_c the drag decreased but at some point, due to large pre-diffusion and diffuser area ratios, drag increased due spillage drag and internal losses. In addition, due to the large diffuser area ratio, the system weight also increased. This statement somewhat contradicts claims by Drela [27], as a lower V_1/V_∞ does not necessarily result in lower drag. The impact on the aircraft's fuel burn was similar at the two extremes of Π_c. Next, it was shown that increasing $d_{H,h}$ almost always results in less fuel burn. This is because a lower $d_{H,h}$ brings the heat exchanger blockage factor closer to unity, which brings down velocities in the heat exchanger core. Moving on, Kellerman et al. [5] elaborate that redundancy considerations in thermal management can significantly impact the system mass, as well as mentioning that integrating a ram air duct in the airframe will be one of the largest challenges. Combining the latter statement with the fact that at the two extreme values of Π_c, the fuel, burn is similar, introducing a performance index based on special requirements can prove decisive.

3

HEAT EXHANGER TYPES, SIZING AND MODELING

This chapter discusses heat exchanger types, physics, and modelling. Section 3.1 categorizes heat exchanger types. Section 3.2 delves into relevant physical phenomena associated with heat exchangers. Following that, Section 3.3 discusses methods for sizing and rating a heat exchanger. The final section of this chapter, Section 3.4, focuses on CFD simulation of heat exchangers using porous media. This section introduces the fundamental concept of modelling heat exchangers using porous media, discusses methods found in the literature for implementing this approach, and addresses issues related to turbulence modelling.

3.1. HEAT EXCHANGER TYPES

The choice of heat exchanger type, topology, and flow arrangement significantly impacts system performance, making it a crucial consideration during the design of a ram air duct. Classifications presented in Shah and Selukic Shah and Sekilic [7] and Zohuri [41] are used to narrow the scope of heat exchanger selection.

A first classification involves the heat transfer process. A primary differentiation exists between direct contact heat transfer and indirect heat transfer. Since the two fluids are not in direct contact, the process qualifies as an indirect heat transfer mechanism. Additionally, heat is directly rejected to the air while the working fluid changes phase.

A second classification is done according to the number of fluids present. In this case, there are only two fluids present.

A third classification involves the compactness of the heat transfer surface area. Compactness is defined as the available surface area for heat transfer divided by the total volume taken up by the heat exchanger. Mathematically this is represented by Equations 3.1 and 3.2. Two definitions are presented: β_1 is valid for plate heat exchangers and plate-fin heat exchangers, and β_2 is valid for tube fin and shell-and-tube heat exchangers. Here, A_h and A_c are the heat transfer surface area of the hot side and cold side, respectively. V_{total}, V_h and V_c are the total volume of the heat exchanger, the volume of the hot-side fluid in the heat exchanger and the volume of the cold-side fluid in the heat exchanger, respectively. The key takeaway is that a heat exchanger classifies as compact from a certain threshold value of β.
Shah and Sekulic [7] mention that compact heat exchangers offer advantages such as reduced space, weight, support structure, footprint, energy requirements, and costs. These benefits hold significant value in aircraft applications, particularly in reducing space and weight penalties of the ram air duct.

$$\beta_1 = \frac{A_h}{V_h} \text{ or } \beta_1 = \frac{A_c}{V_c} \tag{3.1}$$

$$\beta_2 = \frac{A_h}{V_{total}} \text{ or } \beta_2 = \frac{A_c}{V_{total}} \tag{3.2}$$

A fourth classification is done according to the dominant heat transfer mechanism present in the heat exchanger. The categories are divided into single-phase convection, two-phase convection, and combined convection and radiative heat transfer. As the heat exchanger cooled by the ram air ingested in the duct, it can be stated as a first approximation that forced convection is the dominant heat transfer mechanism. Furthermore, there is a phase change in the working fluid. During the phase change in the working fluid, the temperature stays constant (Under the assumption of no pressure losses). Consequently, there might be a scenario where the cold fluid attains the same temperature as the condensing hot fluid. This phenomenon is called temperature pinch, as defined by Shah and Sekulic [7]. Figure 3.1 provides a schematic representation of this effect.

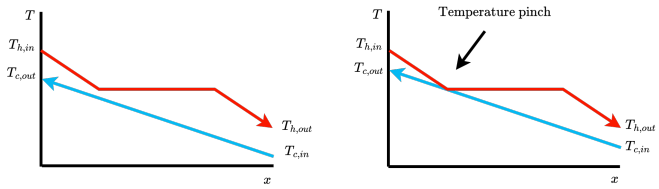

Figure 3.1: Schematic representation of two scenarios with and without temperature pinch. This case is based on a temperature profile for a counter-flow heat exchanger, where the hot side undergoes a phase change while the cold side remains in a single phase.

Figure 3.4 depicts heat exchanger classifications based on the mentioned 4 categories, However, a fifth and final classification is more challenging to categorize systematically and is therefore not included in this figure.

A fifth classification is given in the form of flow arrangement. In general, there is a distinction between single-pass and multi-pass heat exchangers. If multiple single-pass flow heat exchangers are connected together, essentially, a multi-pass configuration is obtained [7]. Therefore, first, the single-pass configurations are examined, namely parallel flow, counter flow, cross flow, split flow, and divided flow. The latter two configurations are particularly relevant for shell-and-tube heat exchangers and are therefore omitted. Schematics depicting these configurations are illustrated in Figure 3.2.

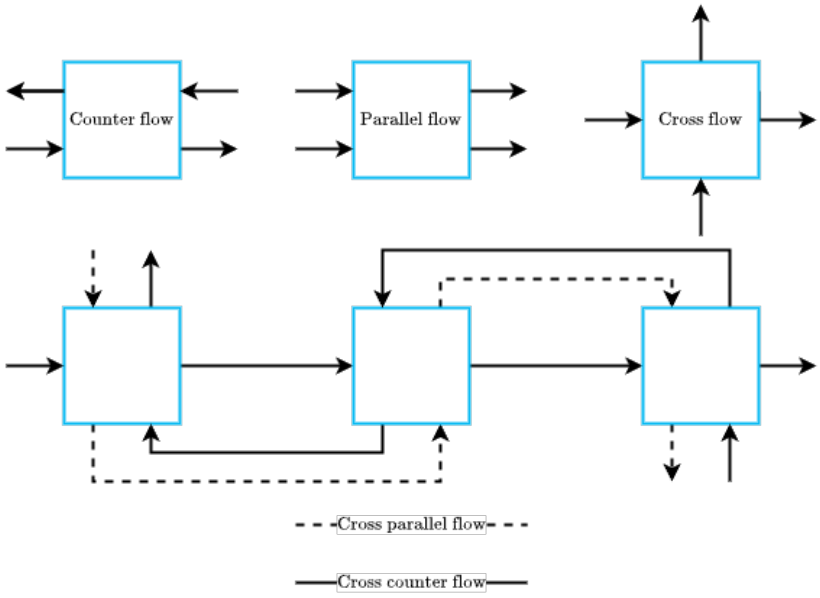

Figure 3.2: Most common single pass configurations and a multipass configuration

By connecting together crossflow heat exchangers, two possible flow paths are created, see Figure 3.2. In one case, the two fluids generally flow in the same direction, known as cross parallel flow, and in the other

case, they flow in the opposite direction, known as cross counter flow. It is important to note that this is not an exhaustive list of all combinations possible but a demonstration of the main flow arrangements and how they can be combined to form other flow arrangements. In practice, all kinds of exotic flow arrangements can be constructed.
The significance of these options becomes evident upon inspecting the temperature profiles for single-phase heat exchangers, as shown in Figure 3.3. This highlights that each configuration entails a distinct average temperature difference, a crucial factor driving heat exchange. However, in scenarios involving phase-changing fluids where temperature mostly remains constant, one could argue that there are not many differences between the single-pass configurations.

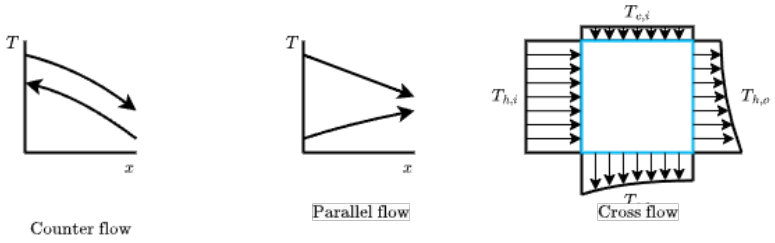

Figure 3.3: Typical temperature distribution for counter-, parallel and cross flow heat exchangers

A final classification involves the construction type. Using the aforementioned categorization for the application at hand the design option space is narrowed to a compact, indirect, two-fluid, multiphase heat exchanger. Within this category there are several construction types, including extended surface heat exchangers, printed circuit heat exchangers, and microchannel heat exchangers. Although not explicitly mentioned by Shah and Sekulic [7], the latter type was later advocated by Sekulic [42] in 2017. The different types are discussed one by one in the following text.

Printed circuit heat exchangers are constructed of plates with fine grooves stacked together. These fine grooves typically range from 0.1 to 2 mm in magnitude and offer significant design flexibility. An example of this is presented by Chu et al. [43], where the grooves of the air side wher in the form of NACA four-digit airfoils.

Microchannel heat exchangers are defined by tubes with very small hydraulic diameters. Sekulic [42] notes the absence of a consensus on the exact definition of when a tube is considered to be of microchannel size. Though, based on the specifications provided by manufacturerers, the channels are normally smaller than 2 mm. The rationale for using very small hydraulic diameters is based on the fact that the heat transfer coefficient is inversely proportional to the diameter of the tube [5] [44]. It should be noted here that the increase in heat transfer coefficient is on one side of the fluid and, therefore, does not rule out the usage of extended surfaces. Typical examples of integration are flat tube microchannels with extended surfaces shown in [42] or tube bundles with exotic shapes [45], [46].

Extended surface heat exchangers take their name from the fact that the primary surface is extended with extra material to enhance heat transfer. Here, the primary surface is defined as the dividing wall between the two fluids. Extending this primary surface increases the total surface area of the heat exchanger, increasing its compactness. The rationale for using extended surfaces lies in matching the thermal resistance on both sides of the heat exchanger. For example, in the case of a gas-to-fluid heat exchanger, the gas side would typically have a heat transfer coefficient one order lower than the fluid side [7]. Adding extended surfaces, or fins, increases the gas-side heat transfer conductance. Consequently, this decreases the bottleneck in the heat transfer process. Section 3.2.1 discusses the concept of thermal resistance in more detail, elucidating further why it is important to match heat transfer coefficients on both sides of the heat exchanger.

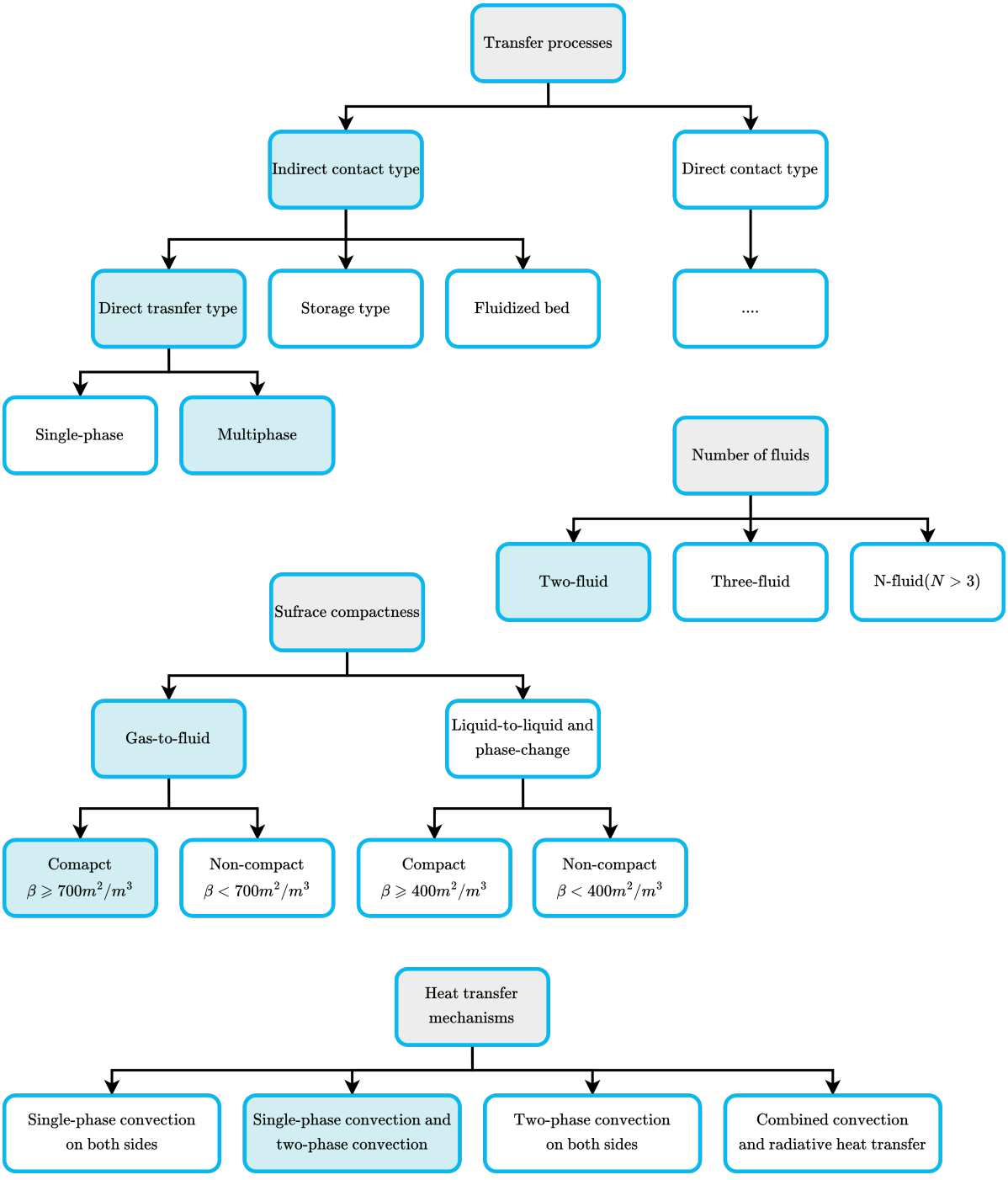

Figure 3.4: Classification of the heat exchanger according to the first four categorisations [7]

3.2. PHYSICAL PHENOMENA ASSOCIATED WITH HEAT EXCHANGERS

This section will discuss relevant physical phenomena associated with heat exchangers, starting with introducing the electrical analogy for heat transfer applied to heat exchangers in Section 3.2.1. Thereafter, Section 3.2.2 will discuss the air-side pressure drop across a heat exchanger in more detail. Finally, Section 3.2.3 will examine the implications of phase change in the hot side fluid.

3.2.1. THERMAL RESISTANCE

Using the electrical analogy, an overarching thermal resistance can be formulated, facilitating the analysis of the heat transfer process. As depicted in Figure 3.5, five distinct media are involved in heat transfer: the

hot-side fluid, the hot-side fouling, the wall, the cold-side fouling and cold-side fluid. The fouling media originate from the accumulation of scale, rust formation, suspended particles in fluids, chemical reactions between fluid and heat exchanger and/or biological growth [7]. Notably, this fouling film is typically less conductive than the wall material, requiring its inclusion in the computation of the heat transfer coefficient.

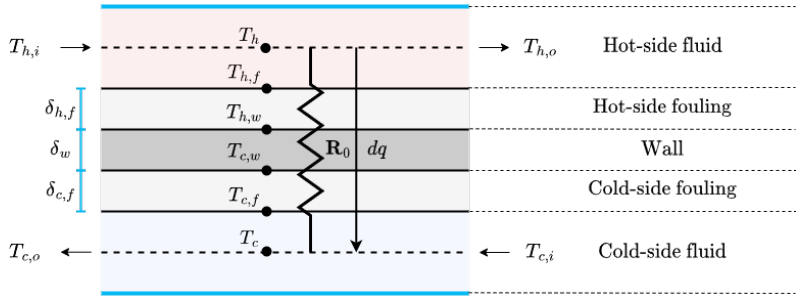

Figure 3.5: Normenclature of station temperature, wall and fouling thicknesses and resistance, reproduced from [7]

In Equation 3.3, the overall relationship between the total thermal resistance and individual resistances is given. Here, R_0, is the total thermal resistance, R_h, is the thermal resistance of the hot-side fluid, $R_{h,f}$, is the thermal resistance of the fouling film on the hot-side, R_w, is the thermal resistance of the wall, $R_{c,f}$, is the thermal resistance of the fouling film on the cold-side and finally, R_c, is the thermal resistance of the cold-side fluid. These resistances produce a mean heat transfer coefficient U_m over the heat transfer area A.

$$\mathbf{R}_o = \mathbf{R}_h + \mathbf{R}_{h,f} + \mathbf{R}_w + \mathbf{R}_{c,f} + \mathbf{R}_c = \frac{1}{U_m A} \tag{3.3}$$

Equation 3.3 can be rewritten into Equation 3.4 in which new variables are introduced. Following the nomenclature in Shah and Sekulic [7] in Equation 3.4, the variable η_0 represents the fin efficiency, this quantity models the added heat transfer capability by the addition of extended surfaces. This implies that the fin efficiency η_0 for heat exchangers with only primary surfaces is unity. h denotes the heat transfer coefficient, and $r_f = 1/h_f$ denotes the fouling factor. The parameters δ_w, k_w and A_w correspond to the wall thickness, wall conductivity and wall area, respectively. It's important to note that the wall thermal resistance definition given in Equation 3.4 applies to flat walls with a single material. Furthermore, it should be noted that all variables are assumed to be their local value.

$$\mathbf{R}_o = \frac{1}{(\eta_o h A)_h} + \frac{1}{(\eta_o h_f A)_h} + \frac{\delta_w}{k_w A_w} + \frac{1}{(\eta_o h_f A)_c} + \frac{1}{(\eta_o h A)_c} \tag{3.4}$$

The temperature differences shown in Figure 3.5 can be used to calculate the heat transfer rate, q, given the thermal resistances as shown in Equation 3.5. Here, T_h represents the hot-side fluid temperature, $T_{h,f}$ denotes the hot-side fouling temperature, $T_{h,w}$ signifies the hot-side wall temperature, $T_{c,w}$ stands for the cold-side wall temperature, $T_{c,f}$ indicates the cold-side fouling temperature, and T_c denotes the cold-side fluid temperature.

$$q = \frac{T_{h,e} - T_{h,f}}{\mathbf{R}_h} = \frac{T_{h,f} - T_{w,h}}{\mathbf{R}_{h,f}} = \frac{T_{w,h} - T_{w,c}}{\mathbf{R}_w} = \frac{T_{w,c} - T_{c,f}}{\mathbf{R}_{c,f}} = \frac{T_{c,f} - T_{c,e}}{\mathbf{R}_c} \tag{3.5}$$

A conclusion that can be drawn from equation 3.5 is that even when only a single thermal resistance is significantly higher than all other thermal resistances, it can have a large impact on the total heat transfer, thus demonstrating the rationale of using extended surfaces as mentioned in Section 3.1.

3.2.2. AIR-SIDE PRESSURE DROP

The pressure drop across the heat exchanger is an important performance metric as discussed in Section 2.3. To get a sense of the governing parameters, the individual contributions to the fluid pressure drop are discussed next.

When a fluid enters a heat exchanger, it experiences a sudden contraction, pressure losses due to friction and heating, acceleration due to heating and a sudden expansion when leaving the heat exchanger. These

factors all play a role in the overall pressure drop of the heat exchanger as shown in Figure 3.6 where the overall pressure drop is defined according to Equation 3.6. It can be seen from Figure 3.6 that the pressure drop is split up into a core entrance pressure drop, a core pressure drop and a core exit pressure rise. The first and last components are split up into changes in pressure due to a change in flow area and pressure losses associated with flow separation. The core pressure drop is split up into pressure losses associated with friction and pressure change due to the change in momentum rate in the core part of a heat exchanger

$$(\Delta p)_{\text{core}} = (\Delta p)_{1-2} + (\Delta p)_{2-3} - (\Delta p)_{3-4} \tag{3.6}$$

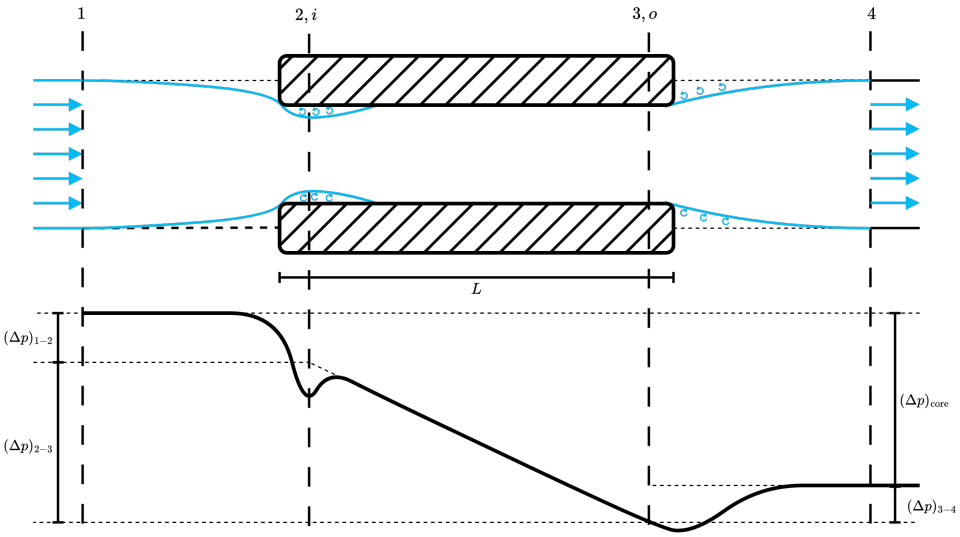

Figure 3.6: Pressure drop components associated with one passage of a heat exchanger based on a flat tube heat exchanger, reproduced from [7]

Shah and Sekulic [7] presented a detailed derivation of the pressure drop elaborating on the individual components of Equation 3.6 to Equation 3.7.

$$\frac{\Delta p}{p_i} = \frac{G^2}{2\rho_i p_i}\left[\underbrace{1-\sigma^2+K_c}_{\text{entrance effect}} + \underbrace{2\left(\frac{\rho_i}{\rho_o}-1\right)}_{\text{momentum effect}} + \underbrace{f\frac{L}{r_h}\rho_i\left(\frac{1}{\rho}\right)_m}_{\text{core friction}} - \underbrace{\left(1-\sigma^2-K_e\right)\frac{\rho_i}{\rho_e}}_{\text{exit effect}}\right] \tag{3.7}$$

In Equation 3.7, σ denotes the heat exchanger blockage factor, that is, the ratio between the minimum free flow area, A_o, and frontal area of the heat exchanger A_{fr}, see Equation 3.8. G denotes the mass flux, defined in Equation 3.9. The parameters, K_c and K_e, are coefficients associated with the separation losses at the contraction and expansion. These depend on the core shape, fin type, Reynolds number, and heat exchanger blockage factor.

$$\sigma = \frac{A_{o,2}}{A_{fr}} \tag{3.8}$$

$$G = \frac{\dot{m}}{A_{o,2}} \tag{3.9}$$

The fanning friction factor, f, is defined as the ratio of the wall shear stress, τ_w, and the kinetic energy flow per unit volume, see Equation 3.10. τ_w is dependent on various properties of the fluid, including the Reynolds number. The mean specific volume with respect to the flow length is defined as in Equation 3.11. This factor accounts for the change in density that occurs over the length of the flow passage.

$$f = \frac{\tau_w}{G^2/2\rho} \tag{3.10}$$

$$\left(\frac{1}{\rho}\right)_m = \frac{1}{L}\int_0^L \frac{dx}{\rho} \tag{3.11}$$

As the free stream conditions, duct geometry, mass flow, and heat duty represent the design specifications of the problem, and the heat duty largely determines the outlet density, as well as the heat exchanger depth, L, the independent variables in Equation 3.12, are shown in bold.

From this equation, it can be pointed out that K_c, K_e and f should be minimized to reduce the pressure drop across the heat exchanger. Furthermore, it can be demonstrated that all other 'free' variables in Equation 3.12 are related to the heat exchanger blockage factor σ: The definition of the hydraulic radius shown in Equation 3.13 can be rewritten by using the definition of heat exchanger compactness shown in Equation 3.1, revealing that the hydraulic radius is a function of β_1 and σ. Furthermore, by recalling Equation 3.9, it can be shown that for a given frontal area of the heat exchanger, A_{fr}, and mass flow rate $\dot{m}$, the mass flux G is also a function of σ. Having established how the heat exchanger blockage factor contributes to variables G and r_h, it is concluded that bringing the blockage factor closer to unity is beneficial when the minimization of the pressure drop across a heat exchanger is a key objective of the design. This recommendation was also made by Drela [27].

$$\frac{\Delta p}{p_i} = \frac{\mathbf{G^2}}{2\rho_i p_i}\left[\underbrace{1-\boldsymbol{\sigma}^2+\mathbf{K_c}}_{\text{entrance effect}} + \underbrace{2\left(\frac{\rho_i}{\rho_o}-1\right)}_{\text{momentum effect}} + \underbrace{\mathbf{f}\frac{L}{\mathbf{r_h}}\rho_i\left(\frac{1}{\rho}\right)_m}_{\text{core friction}} - \underbrace{\left(1-\boldsymbol{\sigma}^2-\mathbf{K_e}\right)\frac{\rho_i}{\rho_e}}_{\text{exit effect}}\right] \tag{3.12}$$

$$r_h = \frac{2A_{o,2}L}{A_{\text{heat transfer}}} = \frac{2A_{0,2}L}{\beta_1 A_{fr} L} = 2\frac{\sigma}{\beta_1} \tag{3.13}$$

Lastly, Shah and Sekulic [7] provide a crucial insight, indicating that the core friction typically constitutes approximately 90% of the total pressure drop in a heat exchanger for gas flows.

3.2.3. IMPLICATIONS OF PHASE CHANGE

Important considerations for the design of a condenser are highlighted when inspecting the implications of the working fluid's phase change. Ideally, the working fluid enters the heat exchanger as a saturated vapour and leaves as a saturated liquid. In reality, however, the fluid enters as a superheated gas, subsequently it turns into a two-phase fluid and exits as a liquid. The processes in the condenser include fluid desuperheating, condensing and subcooling, as shown in Figure 3.7. This figure also highlights the large change in the density of the working fluid in the heat exchanger and the constant temperature during condensation. Here, the former implies large velocity differences of the working fluid between the exit and entry of the exchanger, and the latter implies the onset of a temperature pinch point within the condenser as shown in Figure 3.1. In addition, Shah [7] points out that the heat transfer coefficient of the working fluid is largely dependent on its phase state.

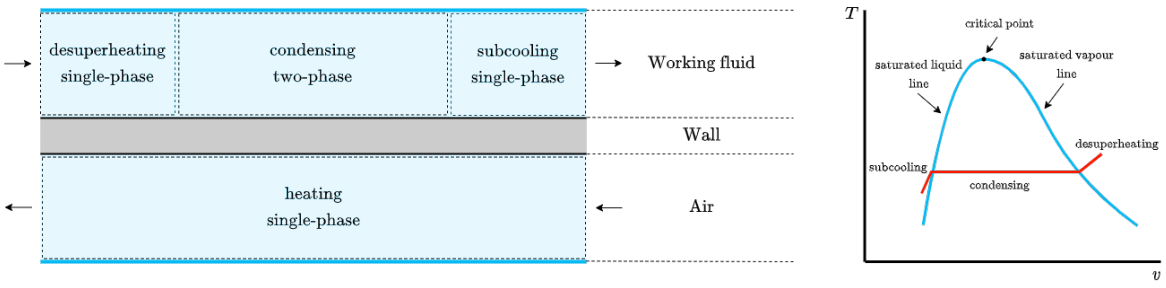

Figure 3.7: Detailed visualisation of different states within a multiphase-single phase condenser

3.3. SIZING AND RATING OF HEAT EXCHANGERS

The difference between the rating and sizing of heat exchangers lies in the different dependent variables. Specifically, in a rating problem, the size and inlet conditions of both sides of the heat exchanger are known, and the outlet conditions are unknowns. Conversely, in the sizing problem, both inlet and outlet conditions are known, and the goal is to find the size of the heat exchanger. Equation 3.14 summarizes the rating problem. The rationale is that the heat rejection, q, or outlet temperatures from the hot-side, $T_{h,o}$, and cold-side, $T_{c,o}$, are a function of the inlet temperatures of the hot-side, $T_{h,i}$ and the cold-side, $T_{c,i}$, the heat capacity rates of the hot-side, $C_h = \dot{m}_h c_{p,h}$, and cold-side, $C_c = \dot{m}_c c_{p,c}$, overall heat transfer coefficient, U, heat trans-

fer area, A and flow arrangement. Alternatively, the problem can be reformulated to find variable A by making q or $T_{h,o}, T_{c,o}$ known, turning the problem into a sizing problem.

$$T_{h,o}, T_{c,o} \text{ or } q = f(T_{h,i}, T_{c,i}, C_h, C_c, U, A, \text{flow arrangement}) \tag{3.14}$$

The independent variables and parameters on the right-hand side of the equation can be grouped into non-dimensional groups. The various ways of doing that produce different methods. Shah and Sekulic [7] give five approaches: $\epsilon - NTU$, $P - NTU$, MTD, $\psi - P$ and $P_1 - P_2$ methods. The first three methods are elaborated upon next.

3.3.1. NUMBER OF TRANSFER UNITS METHOD

In the $\epsilon - NTU$, the heat transfer rate is defined as in Equation 3.15. $C_{\min}$ is defined by Equation 3.16 and ϵ is defined by Equation 3.17. Here, $C_{\min}$ denotes the stream with the lowest heat capacity rate, and ϵ denotes the effectiveness of the heat transfer.

$$q = \epsilon C_{\min}(T_{h,i} - T_{c,i}) = \epsilon C_{\min} \Delta T_{\max} \tag{3.15}$$

$$C_{min} = \min[C_c, C_h] = \min[c_{p,c}\dot{m}_c, c_{p,h}\dot{m}_h] \tag{3.16}$$

$$\epsilon = \frac{q}{q_{\max}} = \frac{C_c(T_{c,o} - T_{c,i})}{C_{\min}(T_{h,i} - T_{c,i})} = \frac{C_h(T_{h,i} - T_{h,o})}{C_{\min}(T_{h,i} - T_{c,i})} \tag{3.17}$$

NTU stands for *Number of Transfer Units* and can be interpreted as the non-dimensional *heat transfer size* of the heat exchanger. The definition is given in Equation 3.18, where U is the overall heat transfer coefficient, A is the heat transfer area and $C_{\min}$ is the minimum heat capacity rate.

$$NTU = \frac{UA}{C_{\min}} \tag{3.18}$$

The usefulness of this method originates from the fact that the *Number of Transfer Units*, NTU, and the effectiveness, ϵ, can be related to each other through relations based on the flow arrangement. For the sizing problem, one can use these relations to estimate the required heat transfer area given: U, q, $T_{h,i}$ and $T_{c,i}$. An example of such a relation is given in Equation 3.19, valid for a counterflow arrangement. This equation also features another variable C^*. This variable is the heat capacity rate ratio defined by Equation 3.20.

$$NTU = \frac{1}{1 - C^*} \ln \frac{1 - C^* \epsilon}{1 - \epsilon} \tag{3.19}$$

$$C^* = \frac{C_{\min}}{C_{\max}} \tag{3.20}$$

In certain applications, there is the possibility that the fluid with the minimum heat capacity rate is not always the same along the heat exchanger. This implies that $C_{\min}$ can switch, and as a consequence, C^* will be wrongly computed. The $P - NTU$ method solves this issue by prescribing a priori which is the side of the heat exchanger with respect to the effectiveness, and the heat capacity rate ratio is defined. This produces the so-called *temperature effectiveness* P, defined in Equation 3.21. Similarly, the heat capacity rate ratio is changed from C^* to R as defined by Equation 3.22, and the definition of NTU is modified as presented in Equation 3.23.

$$P_1 = \frac{T_{1,o} - T_{1,i}}{T_{2,i} - T_{1,i}} \quad \& \quad P_2 = \frac{T_{2,o} - T_{2,i}}{T_{2,i} - T_{1,i}} \tag{3.21}$$

$$R_1 = \frac{C_1}{C_2} = \frac{c_{p,1}\dot{m}_1}{c_{p,2}\dot{m}_2} \quad \& \quad R_2 = \frac{C_2}{C_1} = \frac{c_{p,2}\dot{m}_2}{c_{p,1}\dot{m}_1} \tag{3.22}$$

$$NTU_1 = \frac{UA}{C_1} \quad \& \quad NTU_2 = \frac{UA}{C_2} \tag{3.23}$$

Historically, the $P - NTU$ method has been used for designing shell-and-tube heat exchangers even before the $\epsilon - NTU$ was described [7]. Therefore the $\epsilon - NTU$ method is also a derivation of the $P - NTU$ method. For the application of interest of this work, it is not expected that the minimum heat capacity rate will switch.

3.3.2. MEAN TEMPERATURE DIFFERENCE METHOD

The *Mean Temperature Difference* (MTD) method uses the *Logarithmic-Mean Temperature Difference* (LMTD) and a correction factor based on flow configuration to compute the heat transfer rate q. The LMTD is defined by taking the difference in fluid temperatures at each end of the heat exchanger, yielding Equation 3.24 in the case of a counterflow configuration heat exchanger. The correction factor F is introduced to apply this method for other flow configurations than the counterflow heat exchanger. The definition of the correction factor F is given in Equation 3.26 as the ratio between the true mean temperature difference, ΔT_m, to the log-mean temperature difference, ΔT_{lm}, where ΔT_m is defined in Equation 3.25. Combining these terms yields Equation 3.27 to compute the heat transfer rate q.

$$LMTD = \Delta T_{\text{lm}} = \frac{T_{h,i} - T_{c,o} - T_{h,o} + T_{c,i}}{\ln\left(\frac{T_{h,i}-T_{c,o}}{T_{h,o}-T_{c,i}}\right)} \tag{3.24}$$

$$\Delta T_m = \frac{\Delta T_{\text{max}}\varepsilon}{\text{NTU}} = \frac{T_{h,i} - T_{h,o}}{UA/C_h} = \frac{T_{c,o} - T_{c,i}}{UA/C_c} \tag{3.25}$$

$$F = \frac{\Delta T_{\text{m}}}{\Delta T_{\text{lm}}} \tag{3.26}$$

$$q = UAF\Delta T_{\text{lm}} \tag{3.27}$$

3.3.3. CELL METHOD

Domingos [47] developed such an approach using the dimensionless groups $P-NTU$. A heat exchanger is discretized in blocks or elements based on the flow arrangement. The inlet and outlet temperatures of each element can be expressed as a function of the temperature effectiveness corresponding to that element. The system of equations for one such element is written in Equation 3.28. Converting this to matrix/vector form produces Equations 3.29 and 3.30.

$$\left.\begin{aligned} T_{1,\text{ out}} &= (1-P_1)\,T_{1,\text{ in}} + P_1\,T_{2,\text{ in}} \\ T_{2,\text{ out}} &= P_2\,T_{1,\text{ in}} + (1-P_2)\,T_{2,\text{ in}} \end{aligned}\right\} \equiv \boldsymbol{T}_{oo} = \boldsymbol{M}\boldsymbol{T}_{ii} \tag{3.28}$$

$$\boldsymbol{T_{oo}} = \begin{bmatrix} T_{1,\text{ out}} \\ T_{2,\text{ out}} \end{bmatrix} \quad \boldsymbol{T}_{ii} = \begin{bmatrix} T_{1,\text{ in}} \\ T_{2,\text{ in}} \end{bmatrix} \tag{3.29}$$

$$\boldsymbol{M} = \begin{bmatrix} 1-P_1 & P_1 \\ P_2 & 1-P_2 \end{bmatrix} \tag{3.30}$$

It is possible to assemble a $\boldsymbol{M}$ matrix for all the elements discretizing the heat exchanger based on flow arrangement. In the case of parallel flow heat exchangers, it is sufficient to multiply together the M matrices of each element, starting from the element encompassing the heat exchanger inlet as demonstrated in Equation 3.31. For the counterflow arrangement, the overall M matrix is constructed from those of the individual elements in a different way as further elaborated in [47].

$$\boldsymbol{T_{oo}} = \boldsymbol{M_A M_B M_C} \ldots \boldsymbol{M_n T_{ii}} \tag{3.31}$$

This method can be extended to more complex flow arrangements with splitting and mixing of streams. This is elaborated upon by Domingos [47] and later extended by Pignotti and Tamborenea [48] with the introduction of the chain rule method. The latter method is mostly applicable to tube-and-shell heat exchangers.
In principle, these methods have eliminated the problems pointed out by Shah and Sekulic [7], as it is now possible to predict the temperature distribution over the complete heat exchanger and such methodology can be used for complex flow arrangements. However, these methods still assume that the overall heat transfer coefficient, U, of each element is known. Zohuri [41] points out that determining the heat transfer coefficient typically produces the largest inaccuracies in heat exchanger analysis. For the specific application of this thesis, the working fluid properties undergo significant changes in phase state, density and velocity. All these changes affect the local heat transfer coefficient and, therefore, need to be taken into account in the model. In the upcoming section, a method that addresses this problem is introduced.

3.3.4. MOVING BOUNDARY CELL METHOD

Over the years, there have been a lot of publications suggesting methods for solving the design problem; covering all of these methods is, however, out of the scope of this literature study. The focus is to lay out an approach to size and rate a condenser. Reiterating the boundary conditions of the design problem stated at the beginning of Section 3.3, the known variables in the design problem are the inlet temperatures, $T_{c,in}, T_{h,in}$, and the heat rejection Q or the outlet temperatures $T_{c,out}, T_{h,out}$. Next to these variables, the fluid types are known. Chu and Zhang [8] developed a sizing algorithm that can deal with multi-phase fluids on the hot and cold side of the heat exchanger by splitting up the design problem into separate control volumes based on the given phase of the working fluids with so-called moving boundaries.

Chu and Zhang [8] start solving the design problem by performing an external pinch analysis. By setting the inlet and outlet temperatures of each fluid equal to each other, the maximum amount of heat transfer is calculated. This maximum heat rejection is used to calculate which phase-states the two fluids undergo during heat exchange to discretize the heat exchanger based on unique phase combinations; an example is provided in Figure 3.8. Hereafter an internal pinch analysis is performed to check whether the temperatures of the MB cells comply with the second law of thermodynamics, as shown in Figure 3.1. It is assumed by Chu and Zhang [8] that this non-compliance can only occur for the cold-side fluid at the boundary between the subcooled and two-phase fluid and for the hot-side fluid at the boundary between the two-phase and superheated fluid. At these boundaries, the temperatures of the fluids are set to be equal, and their respective theoretical maximum heat transfer is calculated. The minimum of these three theoretical values, given by the external and the two internal pinch analyses, is used in the subsequent analysis. The MB cells are now split into multiple finite-volume (FV) cells. Here, the total amount of heat transfer in the MB cell is split over the FV cells linearly. From here on, all properties are calculated, including the heat transfer coefficient on both sides of the FV cells. A new wall temperature is then calculated by equating the heat transfer of the two fluids in each FV cell. Once convergence is reached, the required heat transfer area from all FV cells is summed together to produce the total heat transfer area for the MB cell and compared to the heat transfer area initially guessed. Once this is converged, the solver performs the same procedure for all other MB cells.

The key difference from other literature on this approach is that the discretization is performed based on the phase states instead of physical size.

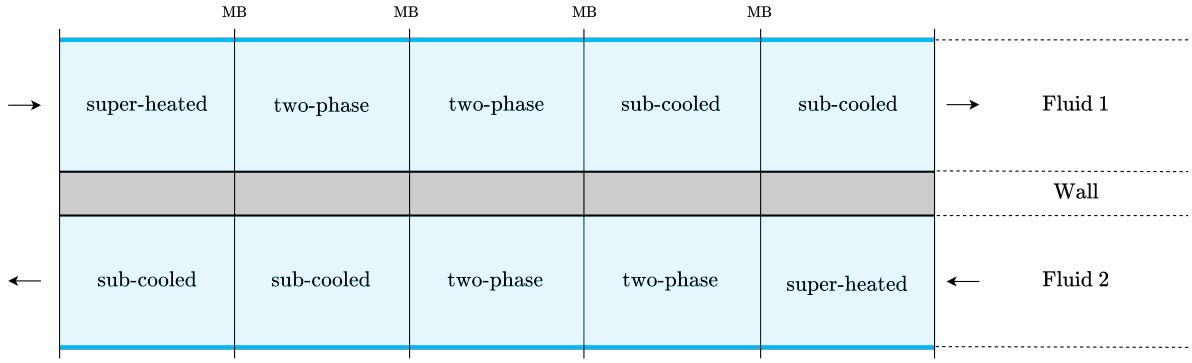

Figure 3.8: Discretization based on unique phase combinations reproduced from Chu and Zhang [8]

3.4. CFD MODELLING OF HEAT EXCHANGERS USING POROUS MEDIA

A promising modelling strategy for heat exchangers in computational fluid dynamics consists of using a porous media to simulate the presence of a heat exchanger.

In a strict definition, a porous media refers to a material that contains pores or voids, allowing fluids to flow within these voids. Examples of natural and artificial porous materials include soil, sand, foam rubber, and bread.

These voids can vary greatly in size and exhibit complex geometries. When attempting to model fluid flow through such media using conventional methods, mesh sizes tend to become very large, resulting in computationally expensive simulations. One approach to circumvent this issue is porous media modelling, which involves replacing the porous media with a fictional block that mimics the behaviour of the original porous media. This approach can also be applied to heat exchangers. This section will introduce the modelling of porous media, followed by a discussion on the recent application of porous media modelling in the context

of heat exchangers.

3.4.1. LENGTH SCALES AND NOMENCLATURE

Before examining how a porous media is represented, it is important to introduce some definitions. Zooming in on an arbitrary porous media, Quintard [9] introduces the nomenclature of the present length scales in porous media as seen in Figure 3.9. Here, the pore length scales l_β and l_σ are presented, denoting the void space β occupied by a fluid of arbitrary single or multi-phase and the solid matrix σ, as well as the length scale of the entire porous media. When trying to treat porous media at a macro-scale, that is to say, representing the porous media by a fictional medium having the same characteristics, a certain minimum scale is required to achieve a representative model.

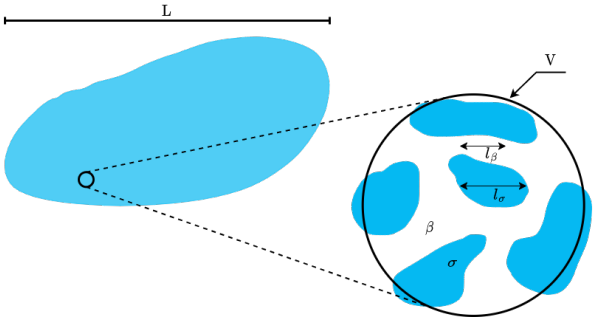

Figure 3.9: Length scales of a porous media, reproduced from [9]

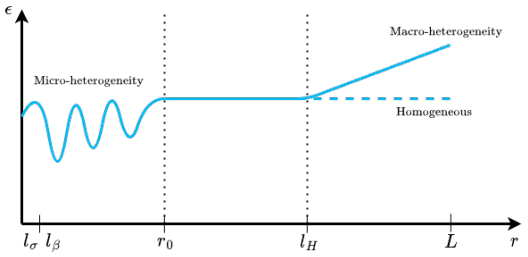

Figure 3.10: Schematic representation of the separation of scales, reproduced from [9]

The relation between the proous media porosity and the minimum length scale is shown schematically in Figure 3.10. The porosity, ϵ, is plotted on the vertical axis, and the length scale on the horizontal axis. Here the porosity, ϵ, is defined by Equations 3.32 to 3.36, starting with the general average of a volume element given by Equation3.32. A phase indicator, γ_β, is introduced in Equation 3.33. Using this phase indicator, the volume fraction occupied by the β phase can be calculated through Equation 3.34. More simply, the porosity, ε_β, is equal to the ratio V_β/V.

$$\langle \phi_\beta \rangle = \frac{1}{V}\int_{V_\beta} \phi_\beta dV \tag{3.32}$$

$$\gamma_\beta = \begin{cases} 1 & M \in V_\beta \\ 0 & M \notin V_\beta \end{cases} \tag{3.33}$$

$$\varepsilon_\beta = \langle \gamma_\beta \rangle = \frac{1}{V}\int_{V_\beta} dV = \frac{V_\beta}{V} \tag{3.34}$$

This volume fraction indicates that the sum of the volume fractions is unity as shown in Equation 3.35. Using the latter equation, the definition of porosity is achieved through Equation 3.36.

$$\varepsilon_\beta + \varepsilon_\sigma = 1 \tag{3.35}$$

$$\varepsilon = 1 - \varepsilon_\sigma \tag{3.36}$$

Figure 3.10 shows that starting from a scale r_0, the porosity does not fluctuate anymore until a certain point, l_H, where there could start to exist a difference in porosity due to macro-heterogeneity. These two points serve as the minimum and maximum scale of the volume, V. The minimum size is sometimes referred to as the minimum *representative elementary volume* (REV).

When comparing the cavities in sand, foam or bread to the cavities in most heat exchangers, it is obvious that the latter cavities are larger and more regular. In addition, the porosity can be linked to a definition found in heat exchangers: the heat exchanger blockage factor, a ratio of the free-flow frontal area and the total area.

3.4.2. ADJUSTING THE GOVERNING EQUATIONS

To represent a porous media, the governing equations need to be adjusted to model the increased velocity, momentum loss and heat transport to the fluid. In the porous media, the velocity increases due to the reduction in flow area by the solid matrix. Next to this, it experiences momentum losses as the solid matrix exerts friction on the fluid, and if the solid matrix has a higher temperature, thermal energy will be transferred as heat to the fluid.
The velocity increase is modelled by defining a physical velocity, equal to the velocity before the porous zone divided by the porosity. The definition is given in Equation 3.37; here, the superficial velocity is equal to the velocity as if there is no solid matrix present.

$$\vec{v}_{\text{superficial}} = \varepsilon \vec{v}_{\text{physical}} \tag{3.37}$$

The momentum losses and thermal energy transport to or from the fluid are modelled by adding source terms into the momentum conservation equation and energy conservation equation as shown in Equations 3.38 and 3.39. For the energy conservation equation, the effective thermal conductivity, k_{eff}, is adjusted with Equation 3.40 to include the effect of the thermal conductivity of the solid matrix. Here, the thermal conductivity in the fluid includes that of the turbulent contribution.
Depending on the simulation task, the source terms $\vec{S}_m$ and $\vec{S}_e$ can be modelled in multiple ways. In the next section, Section 3.4.3, various models for this source terms in the context of heat exchanger modelling will be discussed.

$$\frac{\partial}{\partial t}(\rho \vec{v}) + \nabla \cdot (\rho \vec{v} \vec{v}) = -\nabla p + \nabla \cdot (\bar{\bar{\tau}}) + \rho \vec{g} + \vec{S}_m \tag{3.38}$$

$$\frac{\partial}{\partial t}\left(\varepsilon \rho_\beta E_\beta + (1-\varepsilon)\rho_\sigma E_\sigma\right) + \nabla \cdot \left(\vec{v}\left(\rho_\beta E_\beta + p\right)\right) = \nabla \cdot \left[k_{\text{eff}} \nabla T - \left(\sum_i h_i J_i\right) + (\bar{\bar{\tau}} \cdot \vec{v})\right] + S_e \tag{3.39}$$

$$k_{\text{eff}} = \varepsilon k_\beta + (1-\varepsilon) k_\sigma \tag{3.40}$$

3.4.3. APPLICATION TO HEAT EXCHANGERS

To apply the porous media modelling methodology to heat exchangers, appropriate models need to be selected for the source terms. This section will discuss and show the different methods found in the literature, starting with the momentum source term, $\vec{S}_m$, and continuing with the energy source term S_e. Finally, literature will be discussed in the scope of turbulence modelling in porous zones and the representative elementary volume.

MOMENTUM SOURCE TERM

The Momentum source term is responsible for modelling the momentum losses in the heat exchanger. Missirilis et al. [10] described that the first form of such a momentum source term was that derived by Darcy [49]. Here, a linear term relating the fluid's mean velocity, v, and the hydraulic conductivity, k_h, was used in a relation shown in Equation 3.41. This form neglects the effect of the fluids' viscosity and is therefore only applicable for isothermal, incompressible, and low-velocity flows. Hazen [50] addressed this issue by modifying Equation 3.41 to include the fluid dynamic viscosity and replacing the hydraulic conductivity with the specific permeability, K. This produced the Hazen-Darcy equation shown in Equation 3.42. Still, this relation is only valid for low-velocity flows.

$$\frac{\Delta P}{L} = \frac{1}{k_h} v \tag{3.41}$$

$$\frac{\Delta P}{L} = \frac{\mu}{K} v \tag{3.42}$$

To make the relation also applicable to higher velocity flow, a quadratic term is added as first proposed by Depuit [51], as stated by Missirilis et al. [10]. Equation 3.43, known as the Hazen-Depuit-Darcy equation, introduces the quadratic term as a function of the form drag coefficient, c_F, and the fluid density, ρ. Missirilis et al.[10] mention that Equation 3.43 is also referred to as the Darcy-Forchheimer equation. Most other publications refer to the Darcy-Forchheimer relation; however, all give a slightly different formulation [52],[53], [54]. Here the common denominator is that all publications have the quadratic term but have a different factor before the mean velocity squared. For example, Ahlinder [54] defines the Darcy-Forchheimer equation as Equation 3.44.

$$\frac{\Delta P}{L} = \frac{\mu}{K} v + c_F \rho v^2 \tag{3.43}$$

$$\frac{dP}{dx} = -\frac{\mu}{K} v + c_F K^{1/2} \rho v^2 \tag{3.44}$$

Missirilis et al. [10] point out that the current form of Equation 3.43 is only applicable to isotropic porous material, which in the case of soil or foam is valid but not for most heat exchangers. Generalising Equations 3.43 and 3.44 to three dimensions is therefore required and is done in a similar form by Musto et al. [52], Ahlinder [54] and Missirilis et al.[10]. Equation 3.45 shows the corresponding source term in the momentum equation. In this equation, the matrices **D** and **F** contain the 1st-order and 2nd-order pressure drop coefficients, respectively.

$$\vec{S_m} = \mu \mathbf{D} \vec{v} + \frac{\rho}{2} \mathbf{F} |\vec{v}| \vec{v} \tag{3.45}$$

Different approaches are taken in the literature regarding the implementation of the latter equation. Musto et al.[52] and Hooman and Gurgenci [53] assume a homogeneous porous media, implying diagonal matrices for **D** and **F**. In contrast to this, Ahlinder [54] and Missirilis et al. [10] also include non-diagonal terms in the definition of **D** and **F**. On top of this, Ahlinder [54] and Missirilis et al. [10] split up the porous zone into multiple parts, defining an inlet region, interior and or outlet region, all with different values for **D** and **F**. These differences are summarized in Figure 3.11.

Ahlinder [54] mentions that the use of an inlet region is needed as in the first tube rows, the flow is not symmetric. Thus the matrices **D** and **F** require non-diagonal elemen's for appropriate assessment of the pressure drop. Only after the flow is aligned with the longitudinal direction of the heat exchanger, Ahlinder[54], states that matrices **D** and **F** can be diagonal.

A method different from those presented until now is that of Li et al. [55], where only the fins of a finned tube bundle are modelled by a porous zone. The authors opted to reduce computational costs but without renouncing to the simulation of the general flow structures outside of the fin regions.

Furthermore Missirilis et al. [10], proposes two extra correction coefficients: ζ_μ and ζ_C and normalises the viscosity and density in the momentum source term based on a reference value. These coefficients correct for indirect effects of the temperature-dependent viscosity on the form drag term. This allows the porous zone coefficients to be applied to a wider temperature range.

Porous zone division			Ahlinder	Missirilis et al.	Musto et al.	Hooman and Gurgenci
inlet	interior	outlet	x			
inlet	interior-outlet			x		
single zone					x	x
Tube bundle			x	x		x
Flat tube					x	
straight inflow					x	x

Figure 3.11: Division of porous zones, heat exchanger type and inflow direction

THE ENERGY SOURCE TERM

The energy source term is responsible for the heat transport associated with the heat exchanger. The dimension of the term is a W/m^3, and the determination of this has been done in different ways in the literature.

Starting with the most simple form, Musto et al. [52] and Hooman and Gurgenci [53] apply a calibrated constant heat source independent of the local flow conditions. In contrast, Missirilis et al. [10] proposes an energy source term dependent on local flow properties.
More in detail, Missirilis et al. [10] calculate the local Nusselt number using Equation 3.47 as a function of the local Prandtl number and local Reynolds number computed with Equation 3.46. The Nusselt number is then used to calculate the local heat transfer coefficient as shown in Equation 3.48. Finally, the local heat transfer coefficient is multiplied by the difference between the fluid local temperature and the specified wall temperature and the surface density of the heat exchanger $S_{\text{exchanger}}$, similarly defined as β_1 in Equation 3.1. In these equations, D_{eq} is the hydraulic diameter of the heat exchanger and, $k(T)$, the thermal conductivity of the fluid as a function of the temperature. The procedure is visually shown in Figure 3.12, where it is specified which terms are predefined and which quantities depend on the local solution of the flow and energy equations.

$$Re_{D_{\text{eq}}} = \frac{\rho D_{eq}|V|}{\mu} \tag{3.46}$$

$$Nu = aPr^m Re^n_{D_{\text{eq}}} \tag{3.47}$$

$$h_{\text{local}} = \frac{k(T)Nu}{D_{\text{eq}}} \tag{3.48}$$

$$q_{\text{local}} = h_{\text{local}}[T_{\text{wall}} - T)]S_{\text{exchanger}} \tag{3.49}$$

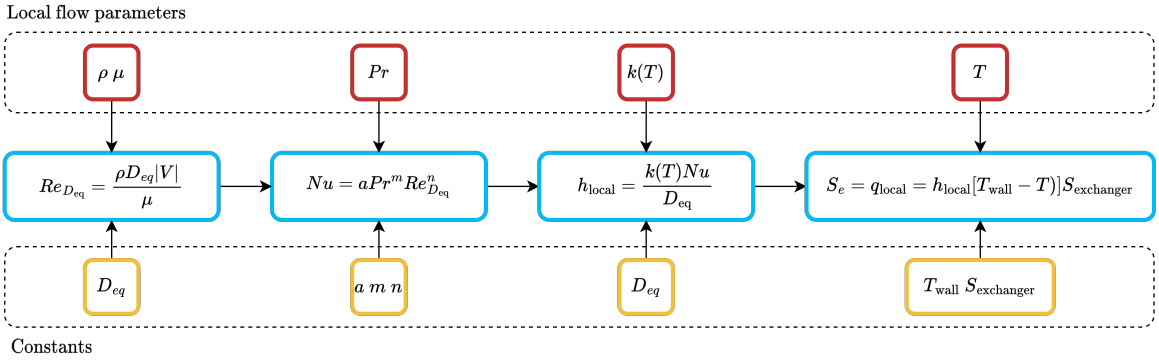

Figure 3.12: Procedure for calculation of energy source term, adjusted from [10]

Ahlinder [54] uses a method similar to Missirilis et al. [10]. The difference lies in the fat that the local flow properties on one side of the heat exchanger but on both sides.

TURBULENCE MODELLING IN POROUS MEDIA

Ahlinder [54] raises attention to the topic of turbulence modelling in porous media, mentioning that turbulent quantities can not be calculated properly in the porous zone without modification to their transport equations. This is demonstrated by Ahlinder [54] by comparing simulations of a tube bundle heat exchanger with and without porous media modelling. Here, the porous zone method showed a higher turbulent viscosity than the detailed grid simulation. This is an important realisation as the turbulent viscosity contributes to the effective thermal conductivity and therefore has consequences on heat transfer in the fluid. Ahlinder [54] mentions that correcting for this can be done by adjusting the turbulent Prandtl number or modifying the energy source term. However, he mentions that the latter is not recommended. Finally, he adds that the level of over-estimation on turbulent heat transport is unknown in his analysis.
Antohe and Lage [56] elaborate on the reason for the over-prediction of turbulent quantities in porous media modelling, stating that it occurs in the case of high Reynolds number flows in porous zones. Antohe and Lage [56] go on with a few examples of how turbulence modelling is different in porous zones when compared to a clear fluid. The first is that the largest eddy in a porous zone is limited by the pore scale of the porous material, and the second one is that it is unclear if a high permeability porous zone has a damping or enhancing effect on the turbulence. This is something that should be considered when analysing the results of a model using porous media modelling.

THE REPRESENTATIVE ELEMENTARY VOLUME

The representative elementary volume, as discussed in Section 3.4.1, should be considered while generating the porous media grid. Interestingly enough, from the literature focused on applying porous media modelling

to heat exchangers cited in this report, only one publication addresses this topic [54]. Most grids presented in the cited literature do not comply with this requirement. Ahlinder [54] recommends keeping cell sizes less or equal to the size of the representative elementary volume. Practically, this means that cell sizes often have to be very large. As a consequence of this, Ahlinder [54] recommends a two-equation turbulence model to balance between the desired accuracy outside of the porous zone and the resolution of the flow field in the porous zone.

4

AIRCRAFT INTEGRATION

Optimal integration of the ram air duct in the aircraft is challenging for multiple reasons, including the space requirement and the type and location of the intake. This chapter elaborates on these topics, starting with a discussion on the intake types, the definition of performance metrics and a comparison between them in Section 4.1. It is noted here that a scoop inlet is the preferred choice for achieving high-pressure recovery, whereas a flush inlet is better suited for reducing drag penalties. After that, the location of the intake on an aircraft and its effects on the added drag and pressure recovery are discussed in Section 4.2. Here, it is pointed out that certain locations are advantageous for integrating an intake due to varying boundary layer thickness around the aircraft. Finally, the effects of heat exchanger inclination are discussed in Section 4.3, showing that heat rejection can be increased without increasing the effective frontal area of a heat exchanger.

4.1. AIR INTAKES

Generally speaking, a distinction can be made into three different types of subsonic inlets [57]. These are shown in Figure 4.1 from left to right. A flush inlet with a ramp in front of the inlet, a scoop inlet, also known as a pitot intake and a static inlet. This latter type of inlet is mostly used in low-speed applications and, therefore, is deemed irrelevant to this literature study. In Figure 4.2, the inlets for the bleedless environmental control system (ECS) of the Boeing 787-9 are shown. This system requires high-pressure air to supply the cabin and air for cooling purposes. As can be noted, two different inlet types are serving the same system. Namely, a scoop inlet with a diverter in front and a flushed inlet. The reasons for this choice can possibly be explained by the main performance characteristics of the two types.

In this section, first, definitions of the pressure recovery, drag and mass flow rate ratio are introduced. Thereafter, the submerged/flush inlet will be discussed in detail, revealing its flow field characteristics in Section 4.1.1, whereafter the scoop inlet is introduced in Section 4.1.2. Finally, the two intake types will be compared based on the performance metrics discussed in Section 4.1.3

Figure 4.1: Inlet types

Figure 4.2: Environmental control system inlets Boeing 787-9, reproduced from [11]

The pressure recovery is defined by Seddon and Goldsmith [20] as the ratio between work done in compression and the available kinetic energy. This gives two separate definitions for the pressure recovery for incompressible and compressible flow shown in Equations 4.2 and 4.1 respectively.
Sacks and Spreiter [12] give a more general form of the pressure recovery factor by taking an area average of the total pressure at the inlet, see Equation 4.3. They declare this metric as a pressure loss parameter, namely as a ratio between the differences in total pressure and the dynamic pressure.

$$\eta_\sigma = \frac{\text{Work done in compression}}{\text{Kinitetic energy available}} = \frac{\left(\frac{p_1}{p_\infty}\right)^{(\gamma-1)/\gamma} - 1}{\frac{\gamma-1}{2}\left(M_\infty^2 - M_1^2\right)} \tag{4.1}$$

$$\eta_{\sigma i} = \frac{p_1 - p_\infty}{q_\infty} \tag{4.2}$$

$$\frac{p_{t_\infty} - p_{t_1}}{q_\infty} = \frac{\Delta p_t}{q_\infty} = \frac{1}{A_{inlet}} \int \frac{\Delta p_t}{q_\infty} dA \tag{4.3}$$

Seddon and Goldsmith [20] elaborate further that, at higher free stream velocities, a more convenient measure of pressure recovery is the simple total pressure ratio. They conclude that while Equation 4.1 is formally correct, in practice, it is easier to use Equation 4.4 for compressible flows. This form of pressure recovery metric is also adopted by Simon and Kowalski [58] in their later-to-be-discussed publication.

$$\eta_P = \frac{p_{t_1}}{p_{t_\infty}} \tag{4.4}$$

Here subscript, ∞, denotes a quantity taken at freestream conditions, t denotes a total quantity, and 1 denotes a quantity taken at the inlet throat. The variables p, q, M, γ and A_{inlet} are the pressure, dynamic pressure, Mach number, specific heat ratio and area at the throat of the inlet perpendicular to the freestream, respectively.

The drag of the inlet is divided by Seddon and Goldsmith[20] into three categories: pre-entry drag, bleed drag and cowl drag. Pre-entry drag is associated with the expansion of the stream tube before entering the intake, bleed drag with diverting the boundary layer, and cowl drag with forces exerted on the housing of the inlet. Seddon and Goldsmith [20] mention explicitly that they only consider drag associated with the intake and not the impact on the total drag of the aircraft. This distinction as the poor instalment of an inlet can deteriorate downstream (or even upstream) aerodynamics.
The ESDU data item 86002 [14] splits the drag into five components: Ram drag, spillage drag, datum drag, skin friction drag and diverter drag. Although the categorisation is different, one component of drag is not mentioned by Seddon and Goldsmith [20]. This is the ram drag term representing the drag associated with the ingested momentum by the intake. Usually, this term is not associated with drag, as this momentum can be conserved throughout the ram air duct.

The mass flow rate ratio defined by Seddon and Goldsmith[20] is the ratio between the mass flow of the captured stream tube and the theoretical mass flow that the area of the inlet can capture. The mathematical definition is shown in Equation 4.5, where A_∞ is the area of the captured stream tube and A_c the inlet area. Furthermore, the subscript ∞ denotes freestream conditions.

$$\mu = \frac{A_\infty \rho_\infty v_\infty}{A_c \rho_\infty v_\infty} = \frac{\dot{m}}{A_c \rho_\infty v_\infty} \tag{4.5}$$

4.1.1. FLUSH INLET

In the 50s and 60s, the former-named National Advisory Committee for Aeronautics (NACA) performed experimental research on flush inlets, also known as submerged inlets. Sacks and Spreiter [12] describe three different types of approach ramps: parallel walls, convergent walls and divergent walls. They are shown in Figure 4.3 from left to right. Their analysis focuses on the divergent ramp as the modelling involves all effects associated with submerged inlets and shows the best overall performance. The effects mentioned are the creation of a vortex around the edges of the diverging channel and the effect on the boundary layer by the diverging flow [12].

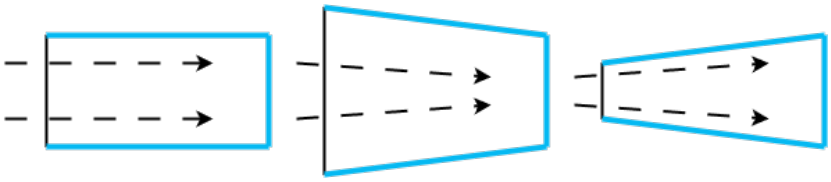

Figure 4.3: Top view of the different types of submerged inlets

By inspecting the boundary layer evolution around this intake, it can be observed that, upon entry, two extra boundary layers are developing on the vertical walls in combination with the formation of two vortices. These vortices' effect is split into two regions as shown on the left-hand side in Figure 4.4. Region I is experiencing an increasing diverging effect, and region II is experiencing a decreasing diverging effect due to the vortices. Sacks and Spreiter describe that this causes the boundary layer thickness in region I to decrease while the boundary layer in region II to increase [12], see on the right-hand side of Figure 4.4.

Sacks and Spreiter [12] elaborate further that the ingested boundary layer and entrained vortexes are the main contributions to the loss in pressure recovery.

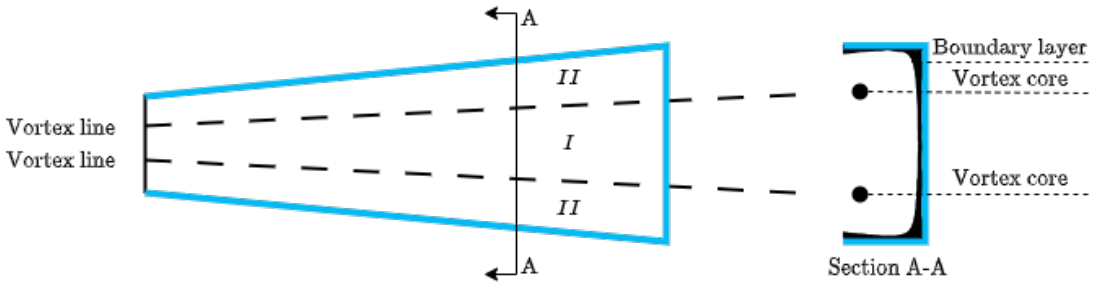

Figure 4.4: Regions that are affected differently by the vortices, reproduced from Sacks and Spreiter [12]

4.1.2. SCOOP INLET

The scoop inlet protrudes from a surface like the bottom inlet in Figure 4.2. Simon and Kowalski [58] differentiate between two types of scoop intakes, a detached and an attached version. Furthermore, they differentiate between fully submerged and partially submerged intakes. This is summarized in Figure 4.5.

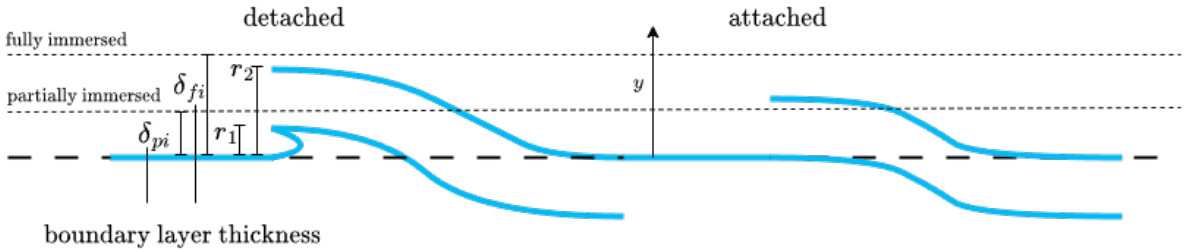

Figure 4.5: Attached and detached scoop inlets, fully immersed and partially immersed

In their research, Simon and Kowalski [58] develop an analytical framework to assess the performance of two types of intakes at full mass flow ratio. They aim to compare the performance metrics for scenarios with varying boundary layer thicknesses. It is revealed that the performance of the scoop inlet is affected by the boundary layer, and an option to mitigate this is to use a detached inlet.

4.1.3. COMPARISON OF SCOOP AND FLUSH INLET

The comparison of the two inlets provides insight into their beneficial and detrimental characteristics. Such a comparison is conducted in the ESDU 86002 report [14]. This report synthesizes various NACA reports and other sources to develop a semi-empirical method for estimating the performance of auxiliary scoop and submerged inlets. The semi-empirical method utilizes inputs based on free stream properties, boundary layer information, and the geometry of the inlet. In the ESDU 86002 report [14], an example compares a circular scoop with a submerged inlet with a curved divergent ramp. These inlets are sized for a mass flow of $\dot{m} = 0.23 kg/s$, a freestream Mach number of $M_\infty = 0.80$, freestream density $\rho_\infty = 0.46 kg/m^3$, freestream velocity $V_\infty = 303.27 m/s$, Reynolds number per unit length $Re = 2.3x10^6 m^{-1}$, boundary layer thickness $\delta = 0.03m$, and boundary layer momentum thickness $\theta = 0.003m$. Here, the submerged inlet is sized for two different operating points, as detailed in the following.

1. Circular scoop designed to operate at a mass flow ratio of 1
2. Submerged inlets with curved divergent ramps designed to operate at max ram pressure recovery
3. Submerged inlet with curved divergent ramps designed to operate at a mass flow ratio of 1.

The results of these calculations reveal that the scoop inlet produces the highest drag and highest pressure recovery. Conversely, the submerged inlet designed for full mass flow demonstrates the lowest drag, 32% lower than the scoop inlet and 15% lower than the submerged inlet designed for maximum pressure recovery. The main reason for the differences in drag between the two submerged inlets is that the submerged inlet designed for maximum pressure recovery operates at a much lower mass flow rate ratio. Subsequently, the throat area must increase to comply with the mass flow requirement. Regarding pressure recovery, the submerged inlet designed for maximum pressure recovery experiences a 12% lower pressure recovery than the scoop, and the submerged inlet designed for full mass flow demonstrates a 28% lower pressure recovery than the scoop.
It is important to highlight that the scoop inlet is submerged in the boundary layer up to approximately the centerline of the intake. In contrast, the throat height of the flush inlets is approximately the same height or smaller than the undisturbed boundary layer. Next, it must be noted that the calculation is performed at significantly lower mass flow rates than the considered test case in this thesis; see Section 10.

EFFECT OF BOUNDARY LAYER THICKNESS

Rütten et al. [59] investigated the effect of boundary layer thickness on the performance of the two types of intakes using the ESDU 86002 report [14]. Their investigation included rectangular attached and detached scoop intakes with varying aspect ratios and a submerged curved divergent ramp inlet. By sweeping the boundary layer thickness, the performance of those inlets was assessed based on pressure recovery and drag. The specifications for this study were as follows: a mass flow of $0.4 kg/s$, a free stream density of $0.31 kg/m^3$, a free stream Mach number of $M_\infty = 0.82$, and a boundary layer thickness swept between $\delta = [0m, 0.5m]$.
The results revealed that all inlet types experience a decrease in pressure recovery with increasing boundary layer thickness. However, the detached scoop inlet begins to decrease in efficiency only when the boundary

layer thickness exceeds the lower lip of the intake. Beyond this point, it exhibits a similar decrease in pressure recovery efficiency as the attached scoop inlet. The submerged curved divergent inlet demonstrates the most pronounced decrease in pressure recovery efficiency with increasing boundary layer thickness.

Regarding the drag of the intakes, initially, at small boundary layer thicknesses, the submerged curved divergent inlet exhibits the least drag. However, as the boundary layer grows, it generates more drag then that produced by the attached scoop inlet. This is explained by the fact that the throat area of the submerged inlet needs to increase to ingest the prescribed amount of mass flow. In contrast to the submerged intake, the scoop inlets present a decrease in drag with increasing boundary layer thickness. The attached scoop inlets have a lower drag impact than the detached scoop inlets for all boundary layer thicknesses. Furthermore, it is observed that there is a large variation in drag for varying aspect ratios in the case of the attached scoop inlet.

From this, it can be concluded that in the case of a reasonable boundary layer thickness, high-aspect-ratio attached scoop inlets perform better in terms of pressure recovery and drag. Furthermore, increasing the aspect ratio of the attached scoop inlet has little influence on pressure recovery while having a significant impact on drag decrease. Furthermore, it can be concluded that the choice of intake type should be based on the preferred performance metric and local boundary layer thickness.

EFFECT OF ANGLE OF ATTACK

Frank and Taylor [60] elaborate on the effect of angle of attack on the performance of the scoop and submerged inlet. Using scaled models in a wind tunnel, the intake performance was measured for varying inclination angles to represent a situation where the intakes are placed on the sides of the airframe. Here, it was found that the submerged inlet showed a sharper decrease in pressure recovery with increasing angles of attack.

4.2. LOCATION OF AIR INTAKE ON AIRCRAFT

To evaluate the optimal location of an intake on the aircraft, Rütten et al. [59] have performed a full CFD of an aircraft flying at similar free stream conditions to the DRAGON concept, with the scope of giving preliminary guidelines for bleedless environmental control systems (ECS). This research holds particular relevance as the performance metrics for such an intake align with the recommendations outlined in Section 2.2, specifically emphasizing high-pressure recovery.

The reference aircraft used for this analysis was the DLR F12 without engines, nacelles, pylons, flaps and flap track fairings, referred to as the clean configuration. This reference aircraft is comparable to an Airbus A340 or a Boeing 777, whereas the DRAGON is comparable to the Airbus 320 [23]. This means that quantitatively applying the conclusions of Rütten et al. [59] to the DRAGON concept should be done with caution.

From the CFD analysis, the boundary layer thickness around the aircraft was estimated and used as input for the semi-empirical method presented in the ESDU 86002 report [14]. From this, performance in terms of drag and pressure recovery was obtained as a function of the intake location on the aircraft. Notably, the boundary layer at the belly of the aircraft is relatively small compared to the tail section, and it is shown that both types of intakes perform well in this area. By comparing this to the ECS inlets of the Boeing 787-9, which features a bleedless ECS [61], the intakes are also located in this area.

Rütten et al. [59] go on to conclude that if high-pressure recovery is preferred, scoop inlets should be used almost everywhere on the aircraft; however, if low drag is preferred, submerged inlets are preferred across most locations on the aircraft. They noted a significant size difference of the submerged intake between the locations on the tail and belly, with the submerged inlet being three times larger than the scoop inlet. This size discrepancy can pose challenges in accommodating a diffuser with the same area ratio as that of the scoop inlet. One aspect not considered as a consequence of using data item ESDU 86002 [14] is the local velocity profile of the boundary layer. This omission arises because ESDU 86002 assumes a constant velocity profile for the boundary layer. However, in reality, the boundary layer at different locations on the aircraft can have varying shapes due to the local curvature of the fuselage.

4.3. HEAT EXCHANGER TILT

By tilting the heat exchanger with respect to the incoming flow, more heat can be rejected by the heat exchanger for the same frontal area, as stated by Hendriksson et al. [13]. In more detail, by tilting the surface area of the heat exchanger can be increased without an increase in vertical size of the ram air duct. In addition, the preceding diffuser area ratio can remain the same, reducing or preventing air separation.

The effect on pressure drop across the heat exchanger due to tilting was first investigated by Nichols [19] in 1942. Later, Hendriksson et al. [13] extended the analysis by including the effect on heat rejection. In contrast to the publication of Nichols [19], Hendriksson et al. [13], performed analysis based on a constant inlet area as shown in Figure 4.6. Their study showcased that inclining the heat exchanger core can lead to increased heat rejection for equivalent pressure drop. This is explained by the fact that the inclined heat exchanger has an increased heat transfer surface area and reduced velocities due to a larger heat exchanger frontal area. Notably, the experiments encompassed Reynolds numbers spanning approximately ~ 2000 to ~ 3000, and it's worth mentioning that apart from the zero inclination angle, no outlet duct was present. These findings underscore the potential benefits of orienting the heat exchanger at an angle relative to the flow direction, highlighting a promising solution for extra performance even without alterations to the inlet duct geometry.

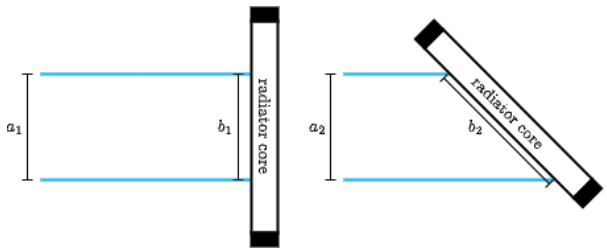

Figure 4.6: Untilted and tilted heat exchanger configuration considered by the publication of Hendriksson et al. [13]

5

Conclusion to the Literature Study

This literature study covers three main topics: the Meredith effect, Heat exchangers and Aircraft integration of ram air ducts.

In Chapter 2, the so-called Meredith effect principles were investigated. By analysing the thermodynamic processes occurring in the ram air duct, it was determined that heat rejection should occur at high pressure. The components preceding the heat exchanger have then to guarantee an efficient recovery of the dynamic pressure of the ingested ram air. Through an examination of literature discussing the modelling of ram air ducts, it was observed that there is an interrelation between duct geometry and heat exchanger performance. Moreover, it was noted that spatial constraints may pose limitations in optimal duct design.

Chapter 3 delved into heat exchanger types, physics, rating, and modelling. By reviewing the classification of heat exchangers proposed in [7], [41], relevant properties of the heat exchangers were discussed. Most notably, it advocated for using a compact heat exchanger type with small hydraulic diameters on the working fluid side. Subsequently, relevant physical phenomena were discussed, emphasizing the significance of matching thermal resistances on both heat exchanger sides and highlighting the heat exchanger blockage factor as a key parameter governing airside pressure drop. Following this, sizing and rating problems were examined, starting with the discussion on the ϵ-NTU, P-NTU, and $LMTD$ methods. It was revealed that these methods are inadequate for modelling novel heat exchanger geometries. To address this limitation, the moving boundary method of discretization was discussed, which offers a quick but accurate analysis of multi-phase heat exchangers. Lastly, in this chapter, the utilization of porous media modelling to represent a heat exchanger in a CFD simulation was highlighted as a promising technique for reducing computational costs without sacrificing accuracy.

Chapter 4 discussed different types of intakes, their optimal locations as well as heat exchanger orientation. The examination of intake types showed that the selection is mainly driven by the chosen performance metric. Literature regarding the intake location underscored that, irrespectively of the preferred performance metric or intake type, positioning the intake at the front of the aircraft's belly is favoured. It's worth noting that this analysis was conducted on a clean aircraft configuration, thus excluding locations such as the engine nacelle. Additionally, this conclusion is solely based on aerodynamic considerations.

Combining conclusions from Chapters 2 and 4, it is possible to make a recommendation for the preferred intake type. In Chapter 2, it was pointed out that heat transfer is most efficient at high pressure, and to achieve this, a high-pressure recovery is required from the intake. The intake that best suits this characteristic is the scoop-type intake, as pointed out in Chapter 4.

Reiterating the conclusion drawn in Chapter 2 about the interrelation between the heat exchanger and ram air duct design, it becomes apparent that the choice of heat exchanger type cannot be made solely based on the heat exchanger's performance alone. On top of that, most of the discussed literature on ram air ducts does not include heat exchanger tilt as one of the design parameters, which was shown to have promising effects

on the ram air duct performance and size.

In light of the considerations above, the research questions associated with this project are as follows.

1. What is the optimal design for the ram air duct accommodating the condenser of a waste heat recovery system for the IMOTHEP DRAGON concept main engines?
    (a) What is the effect on the performance and size of a condenser when this adopts a multi-pass configuration in the air flow direction?
    (b) What is the best heat exchanger type and topology for exploiting the Meredith effect on the IMOTHEP DRAGON concept?
    (c) What is the performance of the optimal ram air duct design predicted by the lumped parameter model versus that predicted by the CFD model?
    (d) What are the differences between the lumped parameter and CFD model?

II

Methodology

6

Introduction to the Methodology

Reiterating the main research question from Chapter 5: What is the optimal design for the ram air duct accommodating the condenser of a waste heat recovery system for the IMOTHEP DRAGON concept main engines? The objective is to identify a low net-drag integration of a condenser. To achieve this, the drag produced by the intake and the total pressure drop over the ram air duct should be minimized while meeting the required heat duty and spatial constraints. To answer the main research question systematically, the research has addressed four subquestions.

To answer the first subquestion, an optimisation of a longitudinal multi-pass heat exchanger is proposed, where the optimiser manipulates various geometrical parameters of each longitudinal pass of the heat exchanger. The performance of the optimized multi-pass heat exchanger is defined by the hot- and cold-side pressure drops across the heat exchanger and will be compared to a baseline single-pass heat exchanger. Details of the methodology will be discussed in Chapter 7.

To answer the second subquestion, a lumped parameter model of a ram air duct is developed. With the lumped parameter model, a sensitivity study will be performed to investigate the effect of geometrical parameters of the ram air duct on the thrust-over-drag ratio and ram air duct length. Thereafter, an investigation into the preliminary optimal design of the ram air duct for varying length constraints will be performed. This optimisation will be performed for various heat exchanger types and diffuser blocked area fractions to identify what heat exchanger type and ram air duct geometry offer the lowest net-drag impact. Details of the methodology will be discussed in Chapter 8.

To answer the third and fourth subquestions, a 2D Reynolds Averaging Navier Stokes (RANS) CFD analysis is set up. The results of this analysis will be compared with the results from the lumped parameter model for multiple design points and different geometrical configurations of the ram air duct. The details of the setup of the numerical simulation and verification are discussed in Chapter 9.

7

LONGITUDINAL MULTI-PASS CONDENSER

The adaptation of the heat exchanger blockage factor per longitudinal pass offers the possibility of controlling the acceleration of the flow in the heat exchanger due to heating, possibly reducing the pressure drop. Next to that, it can account for the density change on the working fluid side as a result of the condensation, shaving off the peak velocity of the working fluid by adjusting the working fluid flow area.

7.1. MODELLING OF THE TRANSVERSAL MULTI-PASS HEAT EXCHANGER

The solution strategy used to solve the system of equations of the counter-crossflow multipass condenser is to use a Jacobi Multi-Disciplinary Analysis (MDA), which decouples the individual passes of the heat exchanger and solves the system iteratively. In this section, first, the problem definition will be formally introduced, whereafter the design vector, bounds and parameterisation will be discussed. Finally, the Extended Design Structure Matrix (XDSM) architecture will be introduced, and the MDA coordinator and optimiser setup will be shown.

7.1.1. PROBLEM DEFINITION

The goal of this methodology is twofold. First, it is to evaluate a single design point. Second, it is to optimise the heat exchanger's geometry for given thermodynamic conditions to achieve the lowest total pressure drop across the heat exchanger. The numerical problem is formulated in Equation 7.1, in which the variable, $p_{t,c}$, is the total pressure of the cold-side, the variable, Y, is heat exchanger height, h_h is the enthalpy of the hot-side fluid and, Q_{duty}, is the heat duty of the heat exchanger. Further nomenclature for the subscripts used in the variables is shown in Figure 7.1. It should be noted that the design vector $\mathbf{x}$ is not limited to the variables listed above and can be extended or adapted by replacing different geometrical parameters. The objective function is a ratio of the total pressure drop of the current function evaluation and the total pressure drop produced by the initial design vector, $\mathbf{x}^{(0)}$.

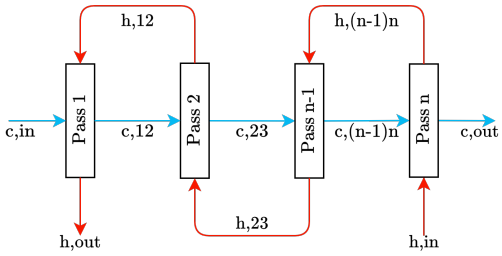

Figure 7.1: Conventions of subscripts for transversal multi-pass configuration

$$
\begin{aligned}
\min_{x} \quad & f(\mathbf{y}(\mathbf{x},\mathbf{y})) = \frac{p_{t,c,in} - p_{t,c,out}}{p^{(0)}_{t,c,in} - p^{(0)}_{t,c,out}} \\
\text{with respect to} \quad & \mathbf{x} \\
\text{where} \quad & \mathbf{x} = [Y_1, Y_2, ..., Y_n - 1, Y_n] \\
\text{with bounds} \quad & \underline{\mathbf{x}} \leq \mathbf{x} \leq \overline{\mathbf{x}}
\end{aligned}
\tag{7.1}
$$

7.1.2. DESIGN VECTOR, BOUNDS AND PARAMETERISATION

As mentioned in the preceding section, the selection of the design vector can be somewhat arbitrary. However, it is crucial that considerations outlined in Section 3.2.2 are taken into account, thus including only

variables that affect the objective function, i.e. the cold-side total pressure drop. The selection of bounds depends on the application, where the spatial limitations should be considered. Next, it is important to bound the geometrical parameters so that the correlations used in the model stay within their validity range. Regarding parameterisation, there is little to gain regarding variable reduction as the model already has the minimal amount of variables required to describe each heat exchanger geometry and topology. The lower and upper bounds used in the optimisation, the reference value used for normalisation and the initial values for the design vector are shown in Table 7.1.

Variable	Lower bound	Upper bound	Reference value	Initial value
Y_{hex}	0.67 [m]	0.87 [m]	0.87 [m]	0.77 [m]
h_{fin}	0.005 [m]	0.014 [m]	0.014 [m]	0.010 [m]
a_{xt}	1.5 [-]	3 [-]	3 [-]	2 [-]

Table 7.1: Lower and upper bound of the design variables used in the optimisation. Next to this, the reference values used to normalise the ddesin vector are reported, as well as the initial values for initialising the optimisation.

7.1.3. XDSM ARCHITECTURE

The XDSM architecture of the optimisation problem is shown in Figure 7.2. A larger size of the same diagram can be found in Appendix A, Figure A.1. The XDSM is constructed using the publication of Lambe and Martins [62] and is of the Multi-Discipline Feasible (MDF) Jacobi type. Following the order of procedure in the XDSM, the design matrix will be explained. Starting with the initialisation of the procedure, the optimiser receives as input the initial design vector $\mathbf{x}^{(0)}$, while the MDA is initialised by giving it the initial guess vector $\hat{\mathbf{y}}^{(0)}$. The iteration begins by evaluating the model of each condenser pass, a moving boundary-like sizing model implemented in the in-house developed tool named *HeXacode* [63]. The results of the design of each condenser pass are then returned to MDA. The MDA checks for convergence, proceeds with a new guess vector, or feeds the results to the objective function when convergence is attained. Once the objective function is evaluated, the result is returned to the optimizer. The optimiser produces a new design vector based on the chosen optimisation algorithm. This loop continues until the termination criteria of the optimisation are met. One caveat of this structure is that each pass is modelled as an individual heat exchanger, meaning that entrance and exit losses are accounted for in the intermediate stations. It is expected that this is an overestimation of the actual pressure drop across the heat exchanger.

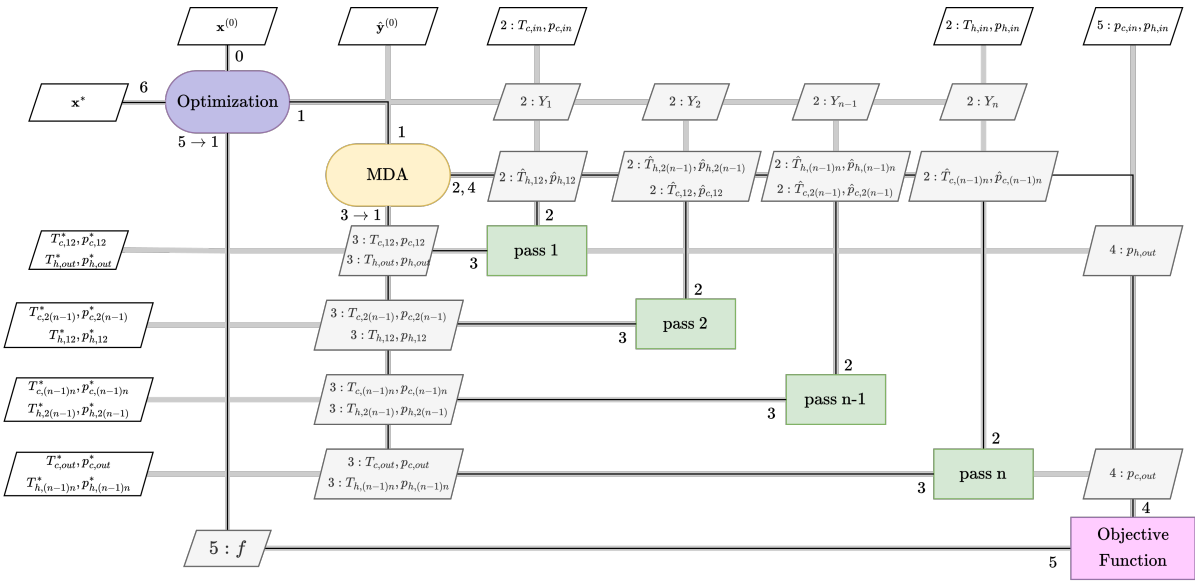

Figure 7.2: MDF-Jacobi XDSM matrix of longitudinal multi-pass heat exchanger

7.1.4. MDO SETUP

The MDA uses a simplistic gradient-free iteration algorithm to produce a new guess variable, see Equation 7.2. To check for convergence, the old and new function inputs are compared until a certain threshold is met. This is shown in Equation 7.3. The variable, r, is a relaxation factor that is reduced with higher values of L. The threshold used for L is 99.99%.

$$\phi_{n+1} = (\phi_n - \phi_{n-1})r + \phi_{n-1} \tag{7.2}$$

$$L = \frac{|\phi_n - \phi_{n-1}|}{|\phi_{n-1}|} \tag{7.3}$$

The optimisation is performed using the minimize function from the open source library *SciPy* [64], which implements the `SLSQP` algorithm. The configuration of this algorithm is shown in Table 7.2. In the results section corresponding to this methodology, Section 11, the design vector is composed of the heat exchanger height variable, Y, for each pass, and the heat exchanger fin height, h_{fin}, or adimensional transversal pitch a_{xt}.

Option	Value
`maxiter`	75
`eps`	1×10^{-3}
`ftol`	1×10^{-6}

Table 7.2: Optimization and convergence settings

8

Lumped Parameter Model Methodology

Previously, it has been highlighted that due to the interrelation between diffusive components and heat exchanger performance, the selection of heat exchanger topology based on the sole performance of the heat exchanger is short-sighted. This motivates a holistic analysis of how all components contribute to the overall drag of the system for each heat exchanger topology candidate. The figure of merit for this analysis is the ratio between the thrust and drag minus unity, such that a net zero drag is reported as zero, a positive thrust as a value greater than zero, and a value below zero in case of drag. It's mathematical definition is given in Equation 8.1.

$$DRF = \frac{F_{\text{nozzle}}}{D_{sc}} - 1 \tag{8.1}$$

In the considered application, differently from the other works documented in literature, the ram air duct is integrated in the engine nacelle. This was decided based on practical considerations. Figure 8.1 depicts the cross-section of the nacelle. Next to this, the heat exchanger types that will be considered are the flat tube microchannel offset strip fin (FTOSF), the flat tube microchannel louvred fin (FTLF), the plain tube bundle inline (PTBI) and the plain tube bundle staggered (PTBS) heat exchanger. These heat exchangers are all classified as compact heat exchangers, as recommended for aerospace applications in Section 3.1.

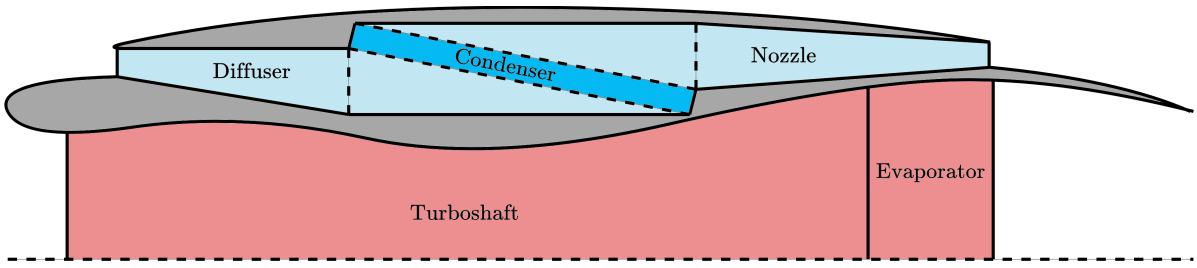

Figure 8.1: Schematic representation of the cross-section of the condenser integration

The lumped parameter model of the ram air duct will be discussed first in Section 8.1. Subsequently, this model will be used to perform a sensitivity study, the methodology of which is presented in Section 8.2. Finally, the lumped parameter will be used in a constraint optimisation to find the optimal duct geometry for each heat exchanger under a certain length constraint, the methodology of which is presented in Section 8.3. The components in this integration will be first discussed in Section 8.1. Subsequently, the methodology used for the sensitivity analysis will be shown in Section 8.2. Thereafter, the methodology for finding the optimum heat exchanger type duct geometry combination will be shown in Section 8.3.

8.1. LUMPED PARAMETER MODEL

The ram air duct has four main components - inlet, diffuser, heat exchanger, and nozzle. However, the system is split into more components, as shown in Figure 8.2 with the corresponding main process stations.

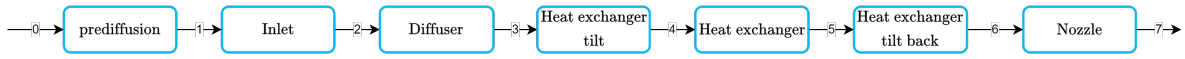

Figure 8.2: Stream-wise station nomenclature

PRE-DIFFUSION

The pre-diffusion occurs in front of the inlet. A key process variable for modelling the intake performance is the mass flow rate ratio, namely, the ratio between the captured mass flow and the mass flow captured by the inlet's forward projected area, as shown in Figure 8.3. Equation 8.2 gives the exact definition of the mass flow ratio.

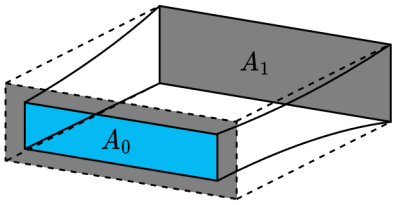

$$\frac{\dot{m}}{\dot{m}_0} = \frac{\rho_\infty V_\infty A_0}{\rho_\infty V_\infty A_1} \tag{8.2}$$

Figure 8.3: Schematic representation of mass flow ratio in front of the inlet

As seen in Figure 8.3, the flow area increases between station zero and one. Due to this increase in area, the flow diffuses and slows down. The non-ingested portion of air goes around the inlet and will contribute towards spillage drag. This is accounted for in the inlet model.

It is assumed that the pressure increases isentropically. By using Equation 8.3 to describe the mass flow at stations 1 and 2, the conservation of mass can be expressed as in Equation 8.4 is obtained. As the area ratio is yet to be determined, Equation 8.2 is substituted for the area ratio, and the Mach number at station 1 is found through numerical iteration for a prescribed mass flow rate ratio. With this, the static temperature and pressure at station 1 can be determined using Equations 8.5 and 8.6.

$$\dot{m} = \frac{A p_t}{\sqrt{T_t}} \sqrt{\frac{\gamma}{R}} M \left(1 + \frac{\gamma - 1}{2} M^2\right)^{-\frac{\gamma+1}{2(\gamma-1)}} \tag{8.3}$$

$$\left(\frac{A_1}{A_0}\right)(M_1)\left(1 + \frac{\gamma-1}{2} M_1^2\right)^{\frac{-\gamma-1}{2(\gamma-1)}} - \left(\frac{M_0}{\left(1 + \frac{\gamma-1}{2} M_0^2\right)^{\frac{-\gamma-1}{2(\gamma-1)}}}\right) = 0 \tag{8.4}$$

$$\frac{p_t}{p} = \left(1 + \frac{\gamma-1}{2} M^2\right)^{\frac{\gamma}{\gamma-1}} \tag{8.5}$$

$$\frac{T_t}{T} = 1 + \frac{\gamma-1}{2} M^2 \tag{8.6}$$

8.1.1. INLET

The inlet model is based on the ESDU report 86002 [14], which describes the pressure recovery and added drag of an intake for both submerged and scoop intakes. For the reasons mentioned in the literature review (Sec. 5), only scoop intakes will be considered here. As mentioned, there are multiple factors in the assessment of the performance of an intake. For convenience and clarity, first, the captured mass flow is discussed, followed by the drag of the intake and, finally, the pressure recovery of the intake. The reference geometry used in [14] and the corresponding nomencalture is presented in Figure 8.4.

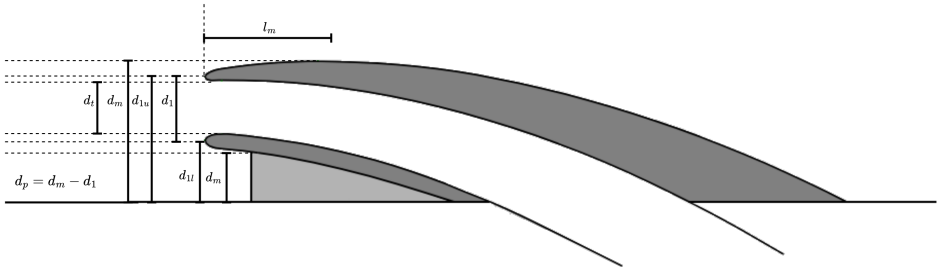

Figure 8.4: Intake described in ESDU data item 86002 [14], all dimensions can be converted to their respective area by multiplication with the width of the intake w

THE INGESTED MASS FLOW

The presence of the boundary layer in front of the intake affects the ingested mass flow because the air in the boundary layer moves slower. In the ESDU report, 86002 [14], charts are presented to assess the effect of the ingested boundary layer on the ingested mass flow rate. This is done by assuming a fixed shape boundary layer and how much of the intake is submerged in it. The chart can be found in Figure B.1 and provides the values for $\dot{m}_{Tu}/\dot{m}_0$ and $\dot{m}_{Tl}/\dot{m}_0$ as a function of Mach number M and boundary layer height ratio δ/h. By iteration, the intake throat area can be sized to ingest the right prescribed mass flow in combination with the assumed boundary layer thickness using Equation8.7. In Equation 8.7, the variables d_{1u} and d_{1l} are the upper highlight height and the lower highlight height, respectively; these variables are also shown in Figure 8.4. The boundary layer height is denoted with variable δ.

$$\dot{m} = \rho_0 V_0 A_1 \left\{ \frac{\dot{m}_{Tu}}{\dot{m}_0} d_{1u} - \frac{\dot{m}_{Tl}}{\dot{m}_0} d_{1l} \right\} \frac{1}{(d_{1u} - d_{1l})} \tag{8.7}$$

THE DRAG OF THE INTAKE

The drag of the intake is split up into multiple contributions. The ram drag, spillage drag, datum drag, skin friction drag, and diverter drag. In Equation 8.8, the individual terms are shown, where the drag coefficients are scaled with respect to the inlet area A and free stream properties at station 0. In the following section, the methodology to estimate each of the drag terms will be discussed in detail.

$$C_{Dsc} = \underbrace{2K_{sc}\left(\frac{\dot{m}}{\dot{m}_0}\right)}_{\text{Ram drag}} + \underbrace{k_f k_{spsc}\left(C'_D - C_{Dffull}\right)_{sh}}_{\text{Spillage drag}} + \underbrace{C_{Dffull}}_{\text{Datum drag}} + \underbrace{C_{DF}}_{\text{Skin friction drag}} + \underbrace{C_{Dd}}_{\text{Diverter drag}} \tag{8.8}$$

The ram drag term is affected by the mass flow ratio and a factor K_{sc}; the latter accounts for reduced ingestion of momentum due to the presence of the boundary layer. The chart to determine K_{sc} is found in Figure B.2. The chart provides values for Ψ_{Tu}/Ψ_0 and Ψ_{Tl}/Ψ_0 as a function of Mach number M and boundary layer height ratio δ/h. The term K_{sc} is computed using equation 8.9.

$$K_{sc} = \left\{ \frac{\Psi_{Tu}}{\psi_0} d_{1u} - \frac{\psi_{Tl}}{\Psi_0} d_{1l} \right\} \frac{1}{(d_{1u} - d_{1l})} \tag{8.9}$$

The spillage drag is built up from three components, k_f, k_{spsc} and $\left(C'_D - C_{Dffull}\right)$.
The first quantity, k_f, accounts for the reduction in spillage drag due to the presence of a smooth-shaped inlet lip. While the current implementation does consider this design feature, it is mentioned in the EDSU report [14] that correlations are not validated for rectangular inlets. Looking at the chart depicted in Figure B.8, the significant advantage of employing a well-shaped inlet lip becomes apparent. In this figure, the variable, A_p, is the forward projected area of the inlet lips excluding the diverter, A_m, is the maximum forward projected area excluding the diverter l_m, is the distance between the inlet lip and the maximum height of the scoop inlet and, w, is the width of the inlet. For more clarification, refer to Figure 8.4, where these variables are shown visually.

The second term, k_{spsc}, provides the relation between the mass flow ratio and the magnitude of the spillage drag, and is mapped in Figures B.6 and B.7. This factor is provided with an upper and lower scatter limit and becomes zero from a mass flow ratio higher than 0.7 for rectangular inlets.

Finally, the factor, $\left(C'_D - C_{Dffull}\right)$, provides the relation of spillage drag at zero mass flow with respect to Mach number at which the intake operates. The factor is mapped in Figure B.5. Here, it is interesting to note that high aspect ratios or, in other words, flatter intakes have significantly lower drag than lower aspect ratio intakes. Also, the correlation is provided here with upper and lower scatter limits.

The datum drag coefficient represents the drag generated by the intake when running at full mass flow and can be interpreted as the baseline drag. The trend, shown in Figure B.4, is similar to the spillage drag; the drag coefficient decreases with higher aspect ratios or, in other words, a flatter intake. Also, the trend is provided with upper and lower scatter limits because of uncertainties in the data used to generate the chart in Figure B.4. Finally, it is mentioned in the report [14] that applying this data to both sharp and smooth-shaped inlet lips is an assumption and that there is not enough data to fully support this choice.

The skin friction drag accounts for the extra wetted area due to the presence of the intake fairing. Depending on location and how the intake is integrated, the skin friction drag may or may not be accounted for in the draft coefficient of the aircraft of engine nacelle drag. For simplicity in this work, the drag around the ram air duct is neglected as it is assumed that the engine nacelle diameter does not change significantly with the size of the ram air duct.

The diverter drag is related to the drag generated by the support below the intake. In this case, the diverter is not present, and therefore, this term will be zero.

THE PRESSURE RECOVERY

The pressure recovery of the intake is modelled by two equations and two charts. The first equation, 8.10, is similar to that for the ingested mass flow. The variables $P_{t,t,Tu}/P_{t,0}$ and $P_{t,t,Tl}/P_{H0}$ are retrieved from the chart in Figure B.3, as a function of Mach number M and boundary layer height ratio δ/h. Equation 8.10 the pressure recovery for a scoop inlet running at full mass flow. If this is not the case, the actual pressure recovery is estimated through Equations 8.11 and 8.12 to account for the boundary layer interaction with adverse pressure gradient in the flow upstream of the intake. The value of k_p in Equation 8.11 is provided by the chart in Figure B.9. Here, θ, is the momentum boundary layer thickness. As mentioned by the authors of the report [14], this serves as an upper limit for this effect.

$$\left(\frac{P_{t,t}}{P_{t,0}}\right)_{\text{sc full}} = \left\{\frac{P_{t,t,Tu}}{P_{H0}}d_{1u} - \frac{P_{t,t,Tl}}{P_{t0}}d_{1l}\right\}\frac{1}{(d_{1u}-d_{1l})} \tag{8.10}$$

$$\frac{\Delta P_{t,t}}{P_{t,0}} \leq -k_p\frac{\theta}{d_{1u}}\left\{1-\left(\frac{\dot{m}}{\dot{m}_0}\right)^3\right\} \tag{8.11}$$

$$\left(\frac{P_{t,t}}{P_{t,0}}\right)_{sc} = \left(\frac{P_{t,t}}{P_{t,0}}\right)_{sc\,\text{full}} + \frac{\Delta P_{t,t}}{P_{t,0}} \tag{8.12}$$

APPLICABILITY AND IMPLEMENTATION

It is important to discuss the limitations of the intake model. Figure 8.1 shows how the condenser and ducting are integrated into the nacelle of the turboshaft. There are many differences when looking at the schematic representation of the intake described by the ESDU report 86002 [14], see Figure 8.4. First of all, the geometry described in the report [14] protrudes from a surface, whereas the envisioned nacelle integration is more streamlined with the original nacelle geometry. This implies that the datum drag term and $\left(C'_D - C_{Dffull}\right)$ give a conservative estimate in their contribution to the drag estimation as these terms are dependent on the geometry of the inlet. Finally, the database used to calibrate the ESDU empirical model does not encompass empirical data for very high aspect ratio inlets.
The implemented model was verified by comparing its predictions to the exemplary calculation in the report [14]. The code was deemed verified, as the comparison was in good agreement with the results in [14].

8.1.2. DIFFUSER

The diffuser model used is based on the work of Sovran and Klomp [17]. In their work, correlations are provided to describe the diffuser performance for diffusers with a rectangular, conical, or annular cross-section.

For the present study, a rectangular cross-section diffuser is chosen. The main geometrical parameters are shown in Figure 8.5, namely, the width, W_1, length, N, and the half angle, θ, of the diffuser. Reneau et al. [16] summarized the relevant flow regimes for the two-dimensional diffusers in Figure 8.6, as a function of the diffuser half angle θ and the non-dimensional length, N/W_1.

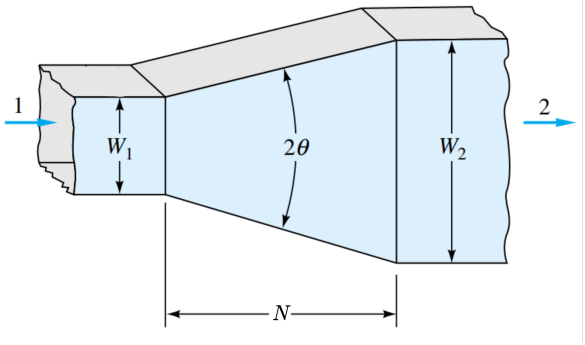

Figure 8.5: Parameters of the rectilinear diffuser with a rectangular cross-section. Reproduced from [15]

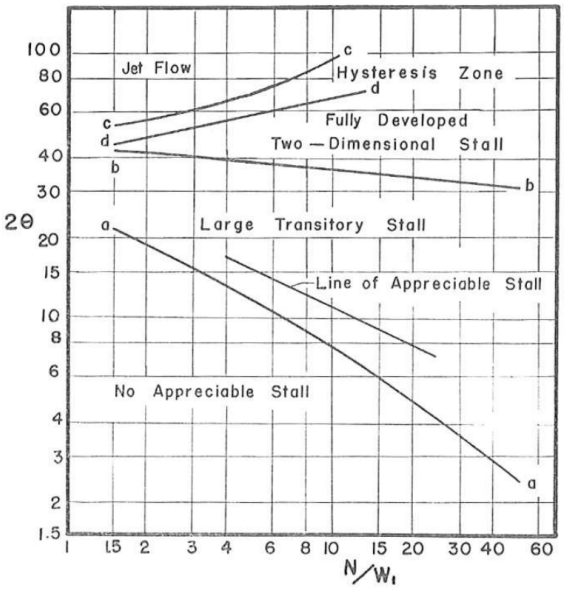

Figure 8.6: Flow regimes in straight-wall, two-dimensional diffusers. Reproduced from Reneau et al. [16]

The conclusion that can be drawn from this chart is that to prevent stall, demarked by line a-a, there is a maximum non-dimensional length given the diffuser half angle. Physically, this can be interpreted as a limit to prevent that the boundary layer is slowed down too fast due to the higher adverse pressure gradient or that the boundary layer thickness grows too much. The optimal diffuser behaviour is sketched in Figure 8.7. Here, the boundary layer remains small, and the core flow stays attached to the walls. When the stall occurs, the flow pattern is similar to that depicted in Figure 8.8, where the core flow cross-section does not increase along the diffuser.

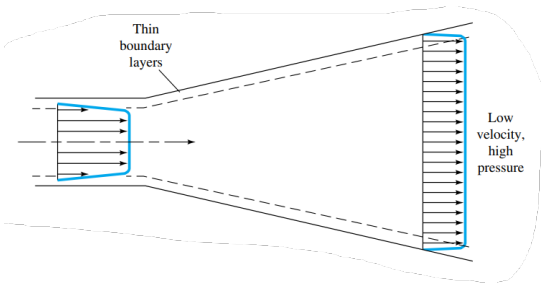

Figure 8.7: Optimal diffuser behaviour. Reproduced from [15]

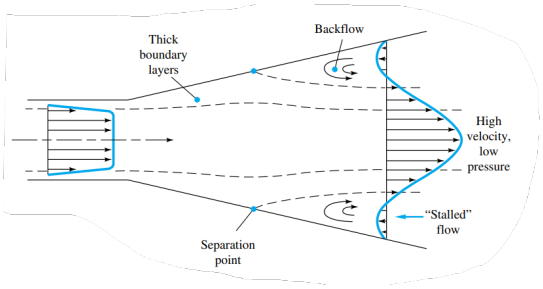

Figure 8.8: Diffuser behaviour with stall. Reproduced from [15]

To describe the performance of a diffuser, Sovran and Klomp [17] made use of a pressure recovery coefficient, whose definition is presented in Equation 8.13. This coefficient is a ratio between the static pressure rise across the diffuser, ΔP_s and the dynamic pressure of the flow. Here, $\bar{q}_1$ (Equation 8.14), is the mass averaged dynamic pressure, which is a function of the mass averaged velocity at the inlet, $\bar{u}_1$, and the density, ρ, where the latter variable is assumed to be constant in this publication.

$$\bar{C_P} = \frac{\Delta P_s}{\bar{q}_1} \tag{8.13}$$

$$\bar{q}_1 = \frac{\bar{u}_1^2}{2}\rho \tag{8.14}$$

Sovran and Klomp [17] recommend to describe the diffuser effectiveness by means of the diffuser effectiveness, $\overline{\mathscr{E}}_0$. This metric corresponds to the ratio between the actual pressure recovery coefficient and the ideal pressure recovery coefficient, shown in Equation 8.15. The ideal pressure recovery coefficient used in the latter equation is defined in Equation 8.16.

$$\overline{\mathscr{E}}_0 = \frac{\Delta P_s}{\Delta P_{s,\mathrm{i}}} = \frac{\Delta P_s / \bar{q}_1}{\Delta P_{s,\mathrm{i}} / \bar{q}_1} = \frac{\bar{C}_P}{\bar{C}_{P,\mathrm{i}}} \tag{8.15}$$

$$\bar{C}_{P,\mathrm{i}} = 1 - \frac{1}{AR^2} = 1 - \frac{1}{(W_2/W_1)^2} \tag{8.16}$$

This effectiveness definition implies that the actual pressure rise is compared to an incompressible and inviscid one-dimensional flow. One could argue that this reference is not fair as it compares the diffuser's pressure rise to a theoretically unattainable value. On top of this, the definition does not reflect what can be maximally achieved given an inflow condition and, therefore, is not only a measure of diffuser performance but also the quality of inflow conditions. When assessing a certain value of effectiveness it is therefore ambiguous if the performance of the diffuser is poor or in inflow conditions sub-optimal.

In the publication of Renau et al. [16], performance charts are published for two-dimensional diffusers. Figure 8.9, depicts one of these charts. Two optimal performance lines can be noticed in the chart. They represent the combination of geometrical parameters allowing for maximum pressure recovery. The first one, C_P^*, gives the optimal area ratio given the non-dimensional length of the diffuser. The second one, C_P^{**}, gives the optimal non-dimensional length for a given area ratio. Between optimal solutions of the C_P^* and C_P^{**} lines, the former is most suitable for the application at hand, as they allow for a shorter diffuser.

Sovran and Klomp [17] assessed how the optimal diffuser design varies with the thickness of the boundary layer at the diffuser inlet, described by the ratio $2\delta^*/W_1$ in Figure 8.10. This chart proves that the optimum geometry is independent of the relative boundary layer thickness. This is a useful observation as it shows that the geometry of the diffuser can be independently selected from the inlet conditions.

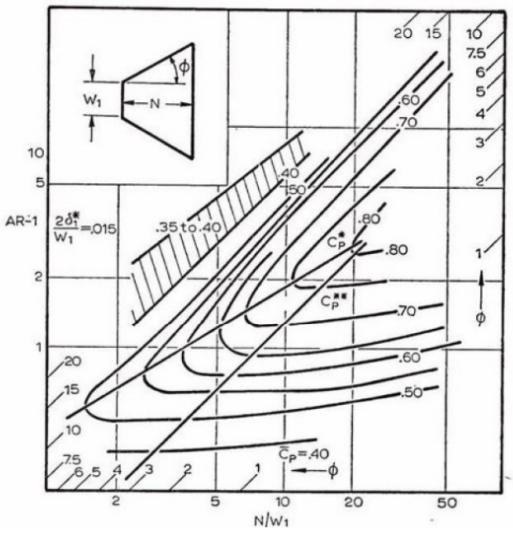

Figure 8.9: Performance chart for two-dimensional diffuser. Reproduced from [17]

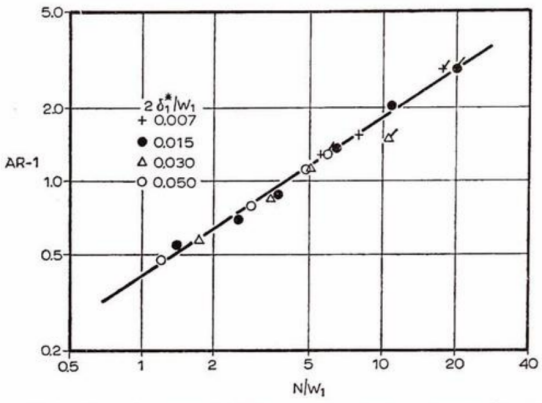

Figure 8.10: Effect of inlet-boundary-layer thickness on optimum geometry for two-dimensional diffusers. Reproduced from [17]

Effect of the boundary layer

While the optimum geometry is independent of the inlet boundary layer, the performance of the diffuser is strongly affected by it. In this regard, the concept of effective area is introduced. This quantity is defined as the area required to pass a uniform flow with a velocity equal to the maximum velocity at that point. In mathematical terms, the definition of the effective area is as presented in Equation 8.17. Inversely, the blocked area is defined as in Equation 8.18. Here, $u_{\max}$ is the maximum velocity. Combining then Equations 8.17, 8.19 and 8.20 together, yields Equation 8.21. This shows that the effective area fraction can also be seen as the ratio between the average- and maximum velocity. This is a useful parameter, as it describes how uniform the flow is at a given cross-section. Looking again at Figures 8.7 and 8.8, a more uniform flow at the exit indicates better diffusion and a less uniform flow at the exit, the contrary. Therefore, comparing E_1 to E_2 can give insight into the effectiveness of the diffuser.

$$A_{\mathrm{E}} = \int^A \frac{u}{u_{\max}} \,\mathrm{d}A \tag{8.17}$$

$$A_{\mathrm{B}} = A - A_{\mathrm{E}} = \int^A \left(1 - \frac{u}{u_{\max}}\right) \mathrm{d}A \tag{8.18}$$

$$E = \frac{A_{\mathrm{E}}}{A} \tag{8.19}$$

$$Q = \int^A u \,\mathrm{d}A = \bar{u}A \tag{8.20}$$

$$\frac{\bar{u}}{U} = E \tag{8.21}$$

Sovran and Klomp [17] rewrite the effectiveness using this observation to Equation 8.22. This version of the equation excludes the extra loss term, also presented in Sovran and Klomp [17], modelling viscous losses in the core flow of the diffuser.

Through analysis of experimental data, Sovran and Klomp [17] produced a correlation relating $AR(100B_1)^{1/4}$ to the effective outlet area E_2 shown in Figure 8.11. Here, B_1 is defined as in Equation 8.23 using the plane-boundary-layer displacement thickness $\delta_{pl,1}$ at the inlet. Furthermore, it is stated that the correlation in Figure 8.11 is valid for conical, annular and rectangular diffusers.

$$\overline{\mathscr{E}}_0 = \frac{1}{E_1^2}\left[\frac{1-\frac{(E_1/E_2)^2}{AR^2}}{1-\frac{1}{AR^2}}\right] \tag{8.22}$$

$$B_1 = \frac{2\delta^*_{pl,1}}{W_1} \tag{8.23}$$

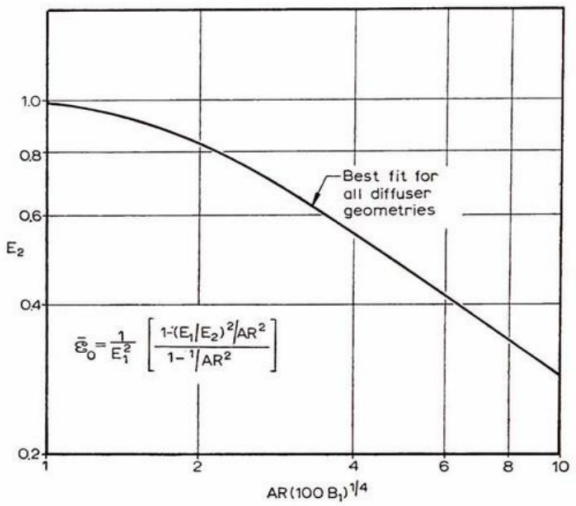

Figure 8.11: Effect of inlet-boundary-layer blockage on the performance of the diffusers on C_P^* and near C_P^*. Reproduced from [17]

The diffuser model has to output the diffuser length, static pressure rise and decrease in velocity, as well as other thermodynamic parameters. The diffuser length is N, is determined using Figure 8.10, given the diffuser area ratio, AR, and inlet height, W_1. The static pressure rise is computed by first determining the effective outlet area E_2 using Figure 8.11, which can subsequently be used to determine the diffuser effectiveness using Equation 8.22. Finally, Equations 8.13 and 8.16 are used to convert the diffuser effectiveness to the static pressure rise. To find the outlet velocity, three assumptions are made. First, it is assumed that the effective inlet area $A_{E,in}$ and the effective outlet area $A_{E,out}$ delineate an inviscid core. Theoretically, this assumption is invalid, as these areas will overlap with the boundary layer and, therefore, will include parts of the flow that exhibit viscous effects. The second assumption is that the static pressure throughout a cross-section is constant. This assumption is valid when there is no streamline curvature present and as, to a first approximation, is the case for a diffuser. The validity of this assumption is also underlined by Sovran and Klomp [17]. The third assumption is that the static temperature is constant throughout the cross-section at the outlet of the diffuser. Since the flow velocity is considerably reduced, the difference between total and static temperatures is small at the diffuser outlet. While this does not support the assumption of uniform outlet static temperature, the variation between static and total temperature for air (ISA @10000m, 0K) is less than 0.8% on a Mach number interval between 0 and 0.2.

Thanks to the first assumption, the flow outlet Mach number can be found using isentropic flow relations similar to Equation 8.4. With the outlet Mach number, the static temperature can be determined, and in combination with the static pressure rise given by the correlation, the density at the diffuser outlet. Finally, by the continuity equation, the average outlet velocity can be calculated and, subsequently, the total pressure. This implies that velocity uniformities at the diffuser outlet are neglected.

APPLICABILLITY AND IMPLEMENTATION

Given the range of validity of all correlations used in the model, the overall range of validity of the latter is as presented in Table 8.1. Finally, it should also be noted that the diffuser geometry shown in the schematic of Figure 8.1 has only one of the two walls moving outward. This means that the diffuser considered for the application at hand has a non-symmetric geometry, as opposed to those studied in [17]. This can have an impact on the accuracy and reliability of the diffuser lumped-parameter model for the ram air duct investigated in the present work.

	Lower	Upper
AR	1	4
B_1	0.007	0.05
Re	$5x10^4$	-

Table 8.1: Range of validity of the model

8.1.3. HEAT EXCHANGER TILT

After the diffuser, the flow has to turn to enter the heat exchanger that is tilted with respect to the diffuser axis. It is assumed that the flow before this component essentially slows down further due to the increase in the flow area.
In the work of Nichols [19] and Henriksson [13], experimental data is presented that describe the extra added pressure drop over the heat exchanger due to the inclination of the heat exchanger with respect to the main flow direction. The experimental data was used to fit a correlation describing a multiplication factor of the pressure drop across the heat exchanger as a function of the inclination angle. This trend is shown in Figure B.10, where the multiplication factor is the ratio of the pressure drop for an inclined heat exchanger with respect to that of a heat exchanger placed orthogonally to the main flow direction. What is interesting to note is that the pressure drop increase due to tilting is fairly small at moderate angles, and increases sharply from an inclination angle of 70 degrees. The pressure rise and velocity decrease due to the increase in flow area at the heat exchanger inlet is modelled using Bernoulli. As the Mach number at this point in the duct is in the incompressible regime, this assumption is deemed to be acceptable.
The effect of the duct flow area restriction downstream of the heat exchanger is modelled similarly by using the Bernoulli and continuity equations to determine the flow pressure and velocity at the nozzle inlet.

APPLICABILITY AND IMPLEMENTATION

One of the limitations of the correlation used to predict the additional pressure drop associated with the heat exchanger inclination is that the effect of inclination is not documented for all types of heat exchangers. Qualitatively, when comparing a flat tube louvred fin heat exchanger to an inline plain tube bundle, the flow in the latter case is less restricted in the transversal direction than with the flat tubes. Next to that, the data that is used to fit the adopted correlation is for much lower flow velocities at the heat exchanger inlet than predicted for the application at hand. For this reason, the inclination angle in the lumped parameter model is limited to 70 degrees. The increase in pressure drop up to this point is relatively small. Then, it is hypothesised that possible inaccuracies have a limited impact on the estimates of the overall pressure drop across the ram air duct predicted by the lumped parameter model. Nonetheless, these inaccuracies should be considered when analysing the results.
Another limitation is that the provided correlations assume a relatively uniform inflow velocity as if the diffuser outlet section has an effective area fraction, E, close to unity. When inspecting Figure 8.11, this would only happen when the area ratio and inlet blocked area fraction are small. This is not the case for the diffuser envisaged for the application at hand.

8.1.4. HEAT EXCHANGER

The heat exchanger is modelled using a method similar to that of Chu and Zhang [8] using a tool called *HeXaCode*[63] which has been verified using the commercial heat exchanger code *Echterm* [65]. This tool enables both the rating and sizing of heat exchangers. The sizing procedure calculates the required heat transfer area, where the dependent variable is the depth of the heat exchanger to meet the required heat duty. In the case of the flat tube microchannel heat exchangers, it thus calculates the required amount of microchannels, and in the case of the plain tube bundle heat exchangers, it calculates the required amount of

tube rows. Subsequently, it also outputs the fluid pressure and temperature at the exit of the heat exchanger. The rating procedure calculates for a given heat exchanger area the temperature and pressure of the cold and hot streams at the exit of the heat exchanger. Both calculation modes will be used in the thesis.

APPLICABILITY AND IMPLEMENTATION

The heat exchanger module uses static quantities. The cold stream inlet conditions are known from the component models upstream of the heat exchanger in the ram air duct, while the hot stream conditions and heat duty are fixed based on the required cooling capacity of the test case's waste heat recovery unit. At the outlet of the heat exchanger component, the total quantities are computed from static quantities using classical isentropic flow relations.

8.1.5. NOZZLE

The nozzle model is as described by Mattingly et al. [36], Equation 8.27 shows the relation to determine the thrust of the nozzle. This is a simplification of the equation found in Mattingly et al. [36] as the nozzle of the ram air duct never reaches the choked conditions. The procedure of calculating the nozzle thrust starts with computing the thrust coefficient, C_{fg}, in Equation 8.26, given the value of three empirical coefficients C_a, C_v and C_{ds}. These are the angularity coefficient, the velocity coefficient and the discharge coefficient. The first coefficient accounts for the misalignment of the exit flow with respect to the reference direction of the thrust. This effect is assumed to be negligible. The second coefficient accounts for the friction losses which are the cause of a reduction in the exit flow velocity compared to an isentropic process. The velocity coefficient is computed using Equation 8.24, where the losses are modelled by specifying a total pressure ratio, η_{P_t}. The third coefficient models the reduction in thrust due to the presence of the boundary layer and is called the discharge coefficient and is calculated using Equation 8.25. As seen in Equation 8.25, this coefficient is calculated as the ratio of the actual mass flow to the ideal mass flow through the nozzle or as the ratio of the ideal to the actual area required for the prescribed mass flow of the nozzle.

$$C_v = \frac{V_{out}}{V_{out,i}} = \frac{\sqrt{\left(1 - \frac{P_{s,7}}{\eta_{P_t} P_{t,6}}\right)^{(\gamma-1)/\gamma)}}}{\sqrt{\left(1 - \frac{P_{s,7}}{P_{t,6}}\right)^{(\gamma-1)/\gamma)}}} \tag{8.24}$$

$$C_{ds} = \frac{\dot{m}}{\dot{m}_i} = \frac{A_i}{A} \tag{8.25}$$

$$C_{fg} = C_v C_a C_{ds} \tag{8.26}$$

$$F_{\text{nozzle}} = C_{fg}\dot{m}V_{out,i} = C_{fg}\dot{m}\sqrt{\frac{RT_{t,6}2\gamma}{1-\gamma}\left(1 - \left(\frac{P_{s,7}}{P_{t,6}}\right)^{(\gamma-1)/\gamma)}\right)} \tag{8.27}$$

A check is implemented to verify whether the static pressure at the nozzle's inlet is not smaller than the ambient pressure. When this scenario occurs, an error message is generated to ensure that the solution is discarded from the analysis. For the computation of the nozzle length, the nozzle half-angle α_d, the area ratio of the nozzle AR_{nozzle}, and the nozzle inlet height H_6 have to specified, see Equation 8.28

$$L_{\text{nozzle}} = L_6 = \frac{H_6(1 - \frac{1}{AR_{\text{nozzle}}})}{\tan(\alpha_d)} \tag{8.28}$$

8.1.6. DUCT MASS ESTIMATION

The mass of the duct is obtained as the sum of two contributions, the heat exchanger mass computed by *HeXaCode* [63] and the mass of the ducting itself, which is proportional to the total duct surface area, A_{duct}. The volume of the walls of the duct is estimated by multiplying this area by a user defined thickness, t, of 2 millimetres. Finally, this figure is multiplied by the density of aluminium, ρ_{alu}, to get a mass estimation of the ducting. The equation used is shown in Equation 8.29.

$$m_{total} = tA_{\text{duct}}\rho_{\text{alu}} + m_{\text{hex}} \tag{8.29}$$

This method implies that the weight needed for fastening, such as bolts, nuts, lap joints, welds, etc., is neglected. Next to that, it is assumed that the material used is aluminium, which is a conservative estimate as this component can also be manufactured out of composite materials offering the same properties as aluminium at a lower specific weight. These simplifications are deemed okay as this performance metric is only used for the comparison of the various ram air duct designs.

8.2. SENSITIVITY ANALYSIS

A sensitivity analysis was performed by using the lumped parameter model to inspect the relative effect of the various geometrical parameters on the weight and thrust of the duct, as well as, to verify if the model is correctly implemented. The bounds of the parameters used in this sensitivity study are shown in Table 8.2. The parameterization method will be described in more detail in Section 8.3.2.

Variable	Lower bound	Upper bound	Constant value
$\dot{m}/\dot{m}_0[-]$	0.5	0.83	0.7
$AR[-]$	1.5	4	3.00
$\theta[deg]$	45	70	70
$h_{fin}[m]$	0.004	0.015	0.0077
$a_{xt}[-]$	1.5	3	2

Table 8.2: Variable bounds and constant values used in Figures 12.1,C.1,C.2 and C.3, where AR is the diffuser area ratio, $\dot{m}/\dot{m}_0$, the mass flow rate ratio, θ, the inclination angle and h_{fin}, the fin height of the flat tube heat exchanger.

The sensitivity analysis is carried out by sampling an arbitrary number of points between the bounds reported in Table 8.2 and assessing the performance of the ram air duct for every combination of these design variables. The lumped parameter model is used in sizing mode to find the drag recovery factor and the length of the duct. This process is repeated for each heat exchanger type considered. The visualization of the data set is done by producing contour plots where two variables are varied. The other two variables are kept constant according to the reference values in Table 8.2.

SENSITIVITY WITH RESPECT TO LOCAL MACH NUMBER

As seen in Figure 8.1, the inlet is located behind the inlet lip of the turboshaft engine, which means that the inlet Mach number and thermodynamic properties differ from those of freestream air. The curvature in front of the inlet, combined with the turboshaft engine intake performance, will influence the inflow conditions of the ram air duct. Since there is no information available at the moment about the geometrical parameters of the engine intake lip and the engine operating range, not much can be said about the effect of the engine intake on the ram air duct. To still evaluate the effect of varying local mach numbers, a parameter sweep will be performed of this quantity. This is done by assuming that the flow entering the ram air duct has gone through an isentropic compression or expansion, or in other words, that the inlet air has the same total pressure and temperature as the freestream air with varying static pressure. In all other analysed cases, the inlet Mach number will be that of the cruise Mach number unless otherwise indicated.

8.3. OPTIMIAL PRELIMINARY DESIGN OF THE RAM AIR DUCT

To identify the best heat exchanger type/topology, it is essential to compare them to the best of their performance. To this purpose, the ram air duct lumped parameter model is run in sizing mode under an optimizer to find the best geometry for each heat exchanger type and combination of the ram air duct design variables. The optimisation problem definition is introduced in Section 8.3.1, while the design vector, bounds and raim air duct parameterization will be discussed in section 8.3.2. The corresponding XDSM will be shown in Section 8.3.3, and the setup of the multidisciplinary optimisation will be shown in Section 8.3.4.

8.3.1. PROBLEM DEFINITION

The optimisation problem is defined as in Equation 8.30, where the objective function is the minimization of the drag recovery factor, and the constraint is set as a limit on the duct's maximum length.

$$\begin{aligned} \min_{x} \quad & f(\mathbf{y}(\mathbf{x},\mathbf{y})) = -\frac{F_{nozzle}}{D_{sc}} \\ \text{with respect to} \quad & \mathbf{x} \\ \text{where} \quad & \mathbf{x} = [\frac{\dot{m}}{\dot{m}_0}, AR, \theta, \text{micro-geometry}] \\ \text{subjected to} \quad & g_1 : \frac{L_{\text{duct}}}{L_{\text{max}}} - 1 \leq 0 \\ \text{with bounds} \quad & \underline{\mathbf{x}} \leq \mathbf{x} \leq \overline{\mathbf{x}} \end{aligned} \tag{8.30}$$

8.3.2. DESIGN VECTOR, BOUNDS AND PARAMETERISATION

Proper parameterisation of the duct geometry is important for two reasons. First, finding an optimum takes longer if the number of variables needed to describe the geometry is large. Second, by choosing a smart method of parameterisation, one can ensure that the model maintains its range of validity by setting bounds. Based on this rationale, the geometrical parameters are first listed with their respective theoretical bounds; see Table 8.3. The first parameter is the inclination angle, which is limited to 70 degrees, as mentioned in section 8.1.3. The second parameter is the diffuser area ratio, where the correlation range is limited to an area ratio of 4. The third parameter is the aspect ratio of the inlet, which only has a lower bound of 4. The fourth parameter is the mass flow rate ratio, which cannot exceed 1. The design variables of the heat exchanger also have limits based on the used empirical correlations and are included in Table 8.3.

Lower bound	Parameter	Upper bound
0 [deg]	θ	70 [deg]
1 [-]	AR	4 [-]
4 [-]	W_1^2/A_1	-
0 [-]	$\dot{m}/\dot{m}_0$	1 [-]
0.005 [m]	h_{fin}	0.014 [m]
1.5 [-]	a_{xt}	3 [-]

Table 8.3: Theoretical parameter bounds on geometrical variables

First, it is important to note that the duct is of fixed and constant width, meaning that only the height at each section needs to be sized. Second, it is important to recall that the length of the diffuser L_2, the length of the nozzle L_6, the outlet area of the nozzle H_7 and the length/depth of the heat exchanger L_4 are a result of the various component models. Furthermore, the height H_0 is constrained by the mass flow rate and the freestream conditions where L_1 is set to an arbitrary constant value. Finally, by looking at Figure 8.12, already, a few simplifications can be made as L_3 is equal to L_4, H_1 is equal to H_2, H_3 is equal to H_6 and H_4 is equal to H_5. This leaves only a few geometrical parameters that need to be defined. These are shown in orange in Figure 8.12.

Starting with H_1, two parameters can go out of bounds: the mass flow rate ratio and the aspect ratio of the intake. As the mass flow rate ratio is a very influential parameter on the initial pressure rise in the duct and the drag of the intake, the mass flow rate ratio is chosen. As this parameter serves as an area ratio between A_0 and A_1, H_1 can be determined as H_0 is known. H_3 can then be determined from the diffuser area ratio.

Finally, H_4 and L_3 can be calculated using the angle of inclination. This leaves the whole geometry of the duct determined by 3 parameters, namely, the mass flow rate ratio $\dot{m}/\dot{m}_0$, the diffuser area ratio AR and the inclination angle θ.

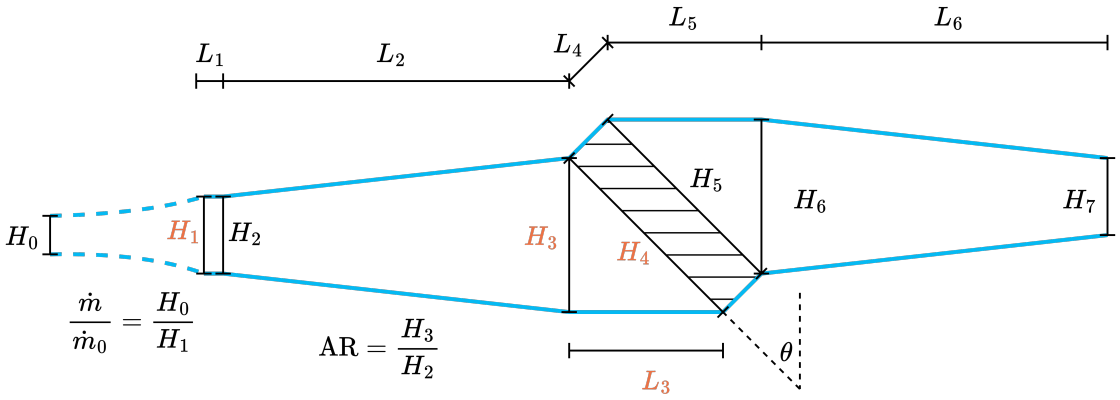

Figure 8.12: Duct parameterisation

Next to this, it is important to include a parameter in the design vector that has some influence on the pressure drop across the heat exchanger. In Section 3.2.2, it was shown that the airside pressure drop is, to a first approximation, a function of the heat exchanger blockage factor. A good method to control the heat exchanger blockage factor of the air side is to change the spacing between the (flat)tubes. For the four types of heat exchangers considered, this can be done by altering the fin height, h_{fin}, and the adimensional transversal pitch, a_{xt}. It is important to note here that for the louvred fin heat exchanger type, the louver length of the fins must grow with the fin height. For the staggered inline tube bundle, the adimensional transversal pitch is set equal to the adimensional longitudinal pitch. Further information about the assumptions made regarding the geometrical parameters of the heat exchangers are shown in B.1.

Finally, it is important to take into consideration how the jacobian of the objective function is computed. The optimization algorithm uses finite differences to estimate the gradient with the consequence that gradients of less influential parameters can become undervalued with respect to other design variables. Tuning the normalisation values based on the results of the sensitivity study can, therefore, improve the convergence of the less effective parameters on the drag recovery factor.

Table 8.4 reports the lower bound and upper bound of the design vector as well as the reference values used for the normalization.

Lower bound	Parameter	Upper bound	Reference value	Initial value
0 [deg]	θ	70 [deg]	60 [deg]	70 [deg]
2 [-]	AR	4 [-]	3 [-]	3 [-]
0.5 [-]	$\dot{m}/\dot{m}_0$	1 [-]	2.5 [-]	0.8 [-]
0.005 [m]	h_{fin}	0.014 [m]	0.025 [m]	0.01 [m]
1.5 [-]	a_{xt}	2.5 [-]	5.625 [-]	2 [-]

Table 8.4: The design vector includes the upper and lower bounds, the reference value used for the normalisation of the design vector, and the initial values used when initialising the optimisation.

8.3.3. XDSM ARCHITECTURE

The XDSM architecture is shown in Figure 8.13, the full version of which can be found in Figure A.2. Starting with the first step in the procedure, the optimisation gets initialized with the initial design vector $\mathrm{x}^{(0)}$, whereafter the lumped parameter model is evaluated. The inputs provided to the duct model include the free stream conditions and the hotside fluid parameters. The selection of freestream parameters will be discussed in more detail in Section 8.3.4. After evaluation of the duct model, the output parameters, $F_{\text{nozzle}}, D_{\text{sc}}, L_{\text{duct}}$,

get handed to the objective function and the constraint function. Next to that, the duct model outputs an array of thermodynamic properties for each station, ψ.

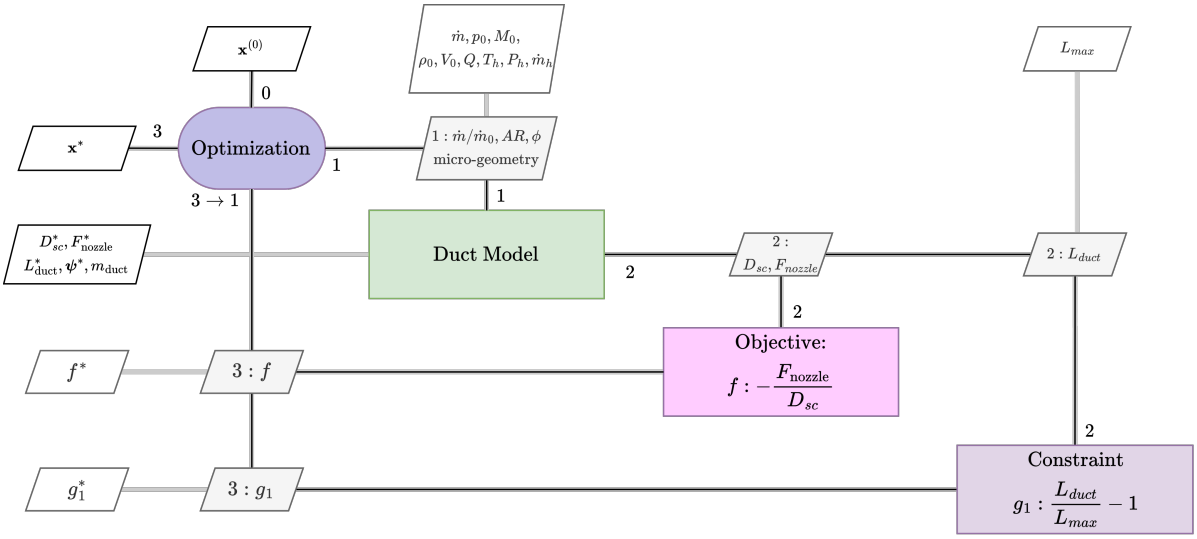

Figure 8.13: XDSM description of optimisation structure

8.3.4. MDO SETUP

The optimisation is performed using the `scipy.optimization.mimize` function with the `SLSQP` algorithm. For the algorithm selection, it is important that the optimiser respects the variable bounds and can deal with inequality constraints. Another requirement for the optimization algorithm is that it is able to deal with discontinuities in the design space, as the length of the heat exchanger grows by adding tube rows or microchannels. Finally, regardless of the chosen parameterisation, the model can produce invalid solutions. In this case, the model will raise an error message. This exception is caught by setting the objective function and constraint to a large positive value. The settings of the optimisation algorithm are specified in Table 8.5. The settings of the lumped parameter model will be discussed further in the test case description in Section 10.

Option	Value
`maxiter`	150
`eps`	1×10^{-3}
`ftol`	1×10^{-8}

Table 8.5: Settings of the optimization algorithm

9

DETAILED PHYSICS MODEL

The design solution generated with constraint optimisation forms the basis to answer the last two research questions. This chapter will discuss in Section 9.1 the simplifications of the heat exchanger duct geometry introduced to implement the CFD model, while Section 9.2 elaborates on the governing equations, the choice for the shear stress transport (SST) model, the configuration of the boundary conditions, solver settings and mesh. The porous media methodology and method of calibration will be shown in Section 9.3. Hereafter, the procedure of verification of the porous media model is introduced in Section 9.3.1 by comparing the results of HeXaCode with the CFD model predictions for a straight duct test case. The final two sections, Sections 9.5 and 9.6, introduce the method used for verifying grid independence and how the results of the detailed physics model can be compared with the lumped parameter model.

9.1. GEOMETRY

The numerical simulations are performed on a two-dimensional mesh of the ram air duct, which is parameterized as shown in Section 8.3. The numerical domain starts at the inlet of the diffuser (station 2) and ends at the nozzle exit (station 7). To improve convergence, large angle/sharp corners are rounded using a radius corresponding to 20 percent of the heat exchanger depth in the airflow direction.

9.2. GOVERNING EQUATIONS, TURBULENCE MODEL & NUMERICAL SETUP

The Navier-Stokes equations for a compressible, viscous and heat-conducting ideal gas are shown in Equations 9.1, 9.2 and 9.3 as described by Hickel [66]. The equations are adjusted to account for the effects of the porous zone by introducing momentum and energy source terms, denoted by S_m and S_e, respectively.
Continuity equation:

$$\frac{\partial \rho}{\partial t} + \frac{\partial (\rho u_i)}{\partial x_i} = 0 \tag{9.1}$$

Momentum equation:

$$\frac{\partial u_j}{\partial t} + u_i \frac{\partial (u_j)}{\partial x_i} = -\frac{1}{\rho}\frac{\partial p}{\partial x_j} + \frac{1}{\rho}\frac{\partial \tau_{ij}}{\partial x_i} + S_m \tag{9.2}$$

Energy equation:

$$\frac{\partial (\rho E)}{\partial t} + \frac{\partial (u_i \rho E)}{\partial x_i} = k_{\text{eff}} \frac{\partial^2 T}{\partial x_i^2} - \frac{\partial u_i p}{\partial x_i} + \frac{\partial u_i \tau_{ij}}{\partial x_i} + S_e \tag{9.3}$$

In these equations, E denotes the total energy of the fluid, k_{eff} denotes the effective thermal conductivity, and τ_{ij} denotes the fluid stress tensor.
As stated in section 3.4, the porous zone is applied to save computational time. On top of that, the porous zone grid needs to comply with the minimal REV. As a consequence, the flow in the porous zone is modelled rather roughly, and therefore, it makes no sense to model the rest of the domain in great detail, e.g. using LES or DNS. Next to that, using higher fidelity models would compromise the original goal of reducing computational costs. Therefore, to obtain a good balance between the accuracy of predictions in the porous domain and the non-porous domain, Ahlinder [54] recommends using the Reynolds averaged Navier-Stokes (RANS)

equations in combination with a two-equation turbulence model. The simplifications applied in the RANS model reduce the computational costs when compared to Large Eddy Simulation (LES) and Direct Numerical Simulation (DNS) while still being able to evaluate the relevant performance metrics of the ram air duct, namely, the total pressure drop, total temperature increase and drag recovery factor (Equation 8.1).
The chosen turbulence model is the k-ω SST model. Originally introduced by Menter [67], the SST model leverages the k-ϵ model's independence from free stream turbulence and the k-ω model's improved prediction of separation in adverse pressure gradients, among other advantages [67]. The governing equations for turbulent kinetic energy, k, and specific dissipation rate, ω, are provided in Equations 9.4 and 9.5. A blending function switches between the k-ω and k-ϵ models, as detailed in Equations 9.6, 9.7, and 9.8, where ϕ represents any coefficient being blended, y is the distance to the next surface, ν is the kinematic viscosity, and $CD_{k\omega}$ represents the cross-diffusion term (Equation 9.11). Another blending function defined in Equation 9.9 and using Equation 9.10 determines the turbulent viscosity (Equation 9.12). The expression of the Reynolds stress term is presented in Equation 9.13. The turbulence model makes use of sets of coefficients provided in Equations 9.14 and 9.15.

$$\frac{\partial \rho k}{\partial t} + \frac{\partial \rho u_j k}{\partial x_j} = \tau_{ij}\frac{\partial u_i}{\partial x_j} - \beta^* \rho \omega k + \frac{\partial}{\partial x_j}\left[\left(\mu + \sigma_k \mu_t\right)\frac{\partial k}{\partial x_j}\right] \tag{9.4}$$

$$\frac{\partial \rho \omega}{\partial t} + \frac{\partial \rho u_j \omega}{\partial x_j} = \frac{\gamma}{\nu_t}\tau_{ij}\frac{\partial u_i}{\partial x_j} - \beta \rho \omega^2 + \frac{\partial}{\partial x_j}\left[\left(\mu + \sigma_\omega \mu_t\right)\frac{\partial \omega}{\partial x_j}\right] + 2\left(1 - F_1\right)\rho \sigma_{\omega 2}\frac{1}{\omega}\frac{\partial k}{\partial x_j}\frac{\partial \omega}{\partial x_j} \tag{9.5}$$

$$\phi = F_1 \phi_1 + (1 - F_1)\phi_2 \tag{9.6}$$

$$F_1 = \tanh(arg_1^4) \tag{9.7}$$

$$arg_1 = \max\left(\max\left(2\frac{\sqrt{k}}{0.09\omega y}; \frac{500\nu}{y^2\omega}\right); \frac{4\rho\sigma_{\omega 2}k}{CD_{k\omega}y^2}\right) \tag{9.8}$$

$$F_2 = \tanh(arg_2^2) \tag{9.9}$$

$$arg_2 = \max\left(2\frac{\sqrt{k}}{0.09\omega y}; \frac{500\nu}{y^2\omega}\right) \tag{9.10}$$

$$CD_{k\omega} = \max\left(2\rho\sigma_{\omega 2}\frac{1}{\omega}\frac{\partial k}{\partial x_j}\frac{\partial \omega}{\partial x_j}; 10^{-20}\right) \tag{9.11}$$

$$\nu_t = \frac{a_1 k}{\max(a_1\omega; \Omega F_2)} \tag{9.12}$$

$$\tau_{ij} = \mu_t\left(\frac{\partial u_i}{\partial x_i} + \frac{\partial u_j}{\partial x_i} - \frac{2}{3}\frac{\partial u_k}{\partial x_k}\delta_{ij}\right) - \frac{2}{3}\rho k \delta_{ij} \tag{9.13}$$

Coefficients used in SST turbulence model

$$\begin{aligned} &\sigma_{k1} = 0.85, \sigma_{\omega 1} = 0.5, \beta_1 = 0.0750, a_1 = 0.31 \\ &\beta^* = 0.09, \kappa = 0.41, \gamma_1 = \beta_1/\beta^* - \sigma_{\omega 1}\kappa^2/\sqrt{\beta^*} \end{aligned} \tag{9.14}$$

$$\begin{aligned} &\sigma_{k2} = 1.0, \sigma_{\omega 2} = 0.856, \beta_2 = 0.0828, \\ &\beta^* = 0.09, \quad \kappa = 0.41, \quad \gamma_2 = \beta_2/\beta^* - \sigma_{\omega 2}\kappa^2/\sqrt{\beta^*} \end{aligned} \tag{9.15}$$

The choice of boundary conditions at the inlet and outlet are defined to match the boundary conditions of the lumped parameter model while ensuring sufficient numerical stability. The total pressure and temperature of the flow are prescribed at the inlet, while the static pressure of the flow is prescribed at the outlet for the ram air duct. This means that the mass flow, static pressure at the inlet and total pressure at the outlet are the output of the model and, therefore, can deviate from their initial prescribed value. The process of matching these deviations in mass flow, static pressure at the inlet and total pressure at the outlet with the limped parameter model will be elaborated upon in Section 9.6. A no-slip condition is applied for all the walls in the flow domain, with the exception of the porous zone, in which a slip condition is applied at the walls because the flow resistance is modelled entirely by the momentum source term. The inflow turbulence is specified by setting a turbulence intensity of 5% and a turbulent viscosity ratio of 10.
The simulation is solved using the Steady Pressure-Based solver of ANSYS Fluent, utilizing a Pseudo-time step method with automatic time step control. The time scale factor is set to 0.05 based on iterative results for improved convergence. The length scale method is configured as *aggressive* (a method in ANSYS Fluent), determining pseudo-time steps based on the flow field and global length of the model. Explicit relaxation factors for the pseudo-time step method are determined iteratively to improve convergence (see Table 9.1). The pressure-based solver is preferred over the density-based solver as it is able to simulate increased velocity in the porous zone due to the restriction in the flow area. The ANSYS user guide recommends this for more

precise porous media flow simulation. A coupled numerical scheme is used for the solution where the spatial discretisation method per quantity is shown in Table 9.1. The gradients of the quantities in Table 9.1 are calculated using the Least Squares Cell-Based method. Finally, the convergence conditions for the residuals are all set to $1e-5$.

	Relaxation Factors	Spatial Discretisation
Pressure	0.5	Second Order
Momentum	0.5	Second Order Upwind
Density	1	Second Order Upwind
Body Forces	1	Second Order Upwind
Turbulent Kinetic Energy	0.225	Second Order Upwind
Specific Dissipation Rate	0.2	Second Order Upwind
Turbulent Viscosity	1	Second Order Upwind
Energy	0.2	Second Order Upwind

Table 9.1: Solver settings

The fluid model is an ideal compressible gas featuring temperature-dependent properties and a constant molecular weight. Coefficients of the polynomials of temperature-dependent properties were estimated using *CoolProp* [68] for air, given the pressure range resulting from the lumped parameter model simulations. Specifications for each property model utilized are outlined in Table 9.2.

	Model specification/polynominal coefficients		
Density [kg/m^3]	ideal-gas		
Specific Heat [J/(kg K)]	1024.201	$-1.7345\cdot10^{-1}$	$3.7\cdot10^{-4}$
Thermal conductivity [W/(m K)]	$7.68049\cdot10^{-4}$	$9.56909\cdot10^{-5}$	$-3.49\cdot10^{8}$
Viscosity [kg/(m s)]	Sutherland		
Molecular weight [kg/mol]	28.9647		

Table 9.2: Fluid model properties

The energy equation in the porous zone assumes equilibrium with the solid material. This means that the energy equation uses an effective conductivity calculated by Equation 3.40 where the thermal conductivity of the fluid includes the turbulent contribution computed by Equation 9.16. The other parameters required for the configuration of the porous zone will be elaborated upon in Section9.3.

$$k_{\text{eff}} = k + \frac{c_p \mu_t}{Pr_t} \tag{9.16}$$

Mesh generation is performed using ANSYS Meshing. The domain is divided into multiple sections, each with a structured mesh except for sections identified as 3 and 7 in Figure 9.1. The reason thereof is the impossibility of the software to maintain a structured grid for these parts during grid refinement. A uniform inflation layer is applied across the walls of the domain. The inflation layer is specified with a total inflation layer thickness of five times the internal mesh element size, a growth rate of 1.2, and 34 layers. This configuration of the inflation layer ensured a smooth transition to the internal mesh. The internal mesh element size selected for the domain is determined based on a grid convergence study. Nonetheless, it's essential to consider the concept of the minimum Representative Elementary Volume (REV) and the recommendation by Ahlinder [54] to utilize element sizes that are smaller than or equal to the REV. The resulting mesh is shown in Figures 9.2 and 9.3.

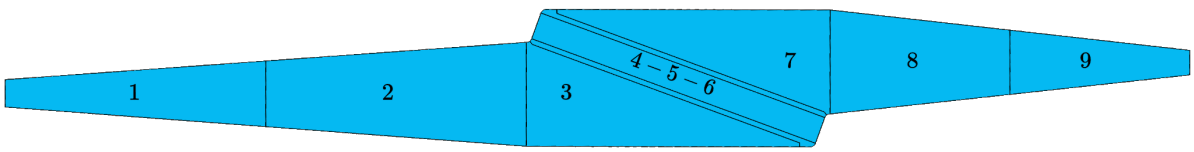

Figure 9.1: Duct domains

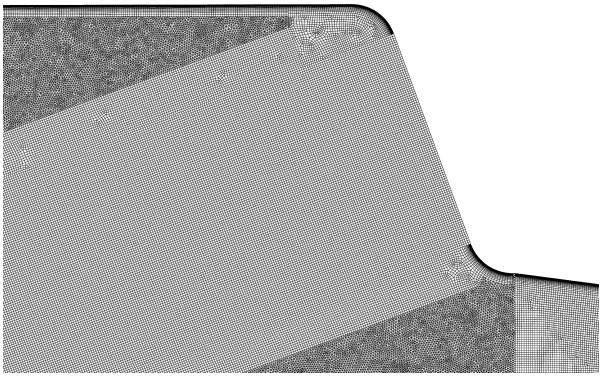

Figure 9.2: Mesh of the computational domain, focusing on the bottom right corner of the porous zone

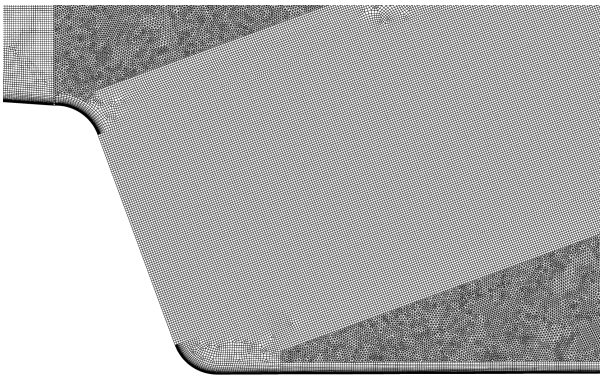

Figure 9.3: Mesh of the computational domain, focusing on the top left of the porous zone

9.3. POROUS MEDIA MODEL CONFIGURATION AND CALIBRATION

The porous media model uses a momentum sink and an energy source to mimic the presence of the heat exchanger in the CFD domain. In the upcoming sections, the models used for the momentum and energy source will be explained in Sections 9.3.1 and 9.3.2, respectively. Subsequently, the calibration procedure will be elaborated upon in Section 9.3.3.

9.3.1. THE MOMENTUM SOURCE

The momentum sink is expressed in the form of the Darcy-Forchheimer equation. The basic one-dimensional form is shown in Equation 9.17, which can be rewritten to a simpler form as in Equation 9.18.

$$\frac{\Delta P}{L} = \frac{\mu}{K} v + c_F \rho v^2 \tag{9.17}$$

$$\frac{\Delta P}{L} = \mu v D_{\text{ref}} + 0.5 \rho v^2 F_{\text{ref}} \tag{9.18}$$

The porous zone features a symmetric formulation of the momentum source term as expressed in equation 9.19. This assumption is supported by the flow straightening effect of the flat tube and fin HX topology. More in detail, the transversal velocity component dissipates quickly as the fluid enters the heat exchanger. Therefore, the one-dimensional nature of the flow within the HX core justifies the omission of non-diagonal terms in the momentum source term model. When the flow cannot be considered one-dimensional, for example, in tube bundles, the calibration of the non-diagonal terms requires detailed experimental or numerical data, particularly regarding inclined inflow angles.

$$S_m = \underbrace{\mu \begin{pmatrix} D_{\text{ref}} & 0 \\ 0 & D_{\text{ref}} \end{pmatrix} \begin{pmatrix} u \\ v \end{pmatrix}}_{\text{Darcy}} + \underbrace{\frac{1}{2} |\vec{V}| \rho \begin{pmatrix} F_{\text{ref}} & 0 \\ 0 & F_{\text{ref}} \end{pmatrix} \begin{pmatrix} u \\ v \end{pmatrix}}_{\text{Forchheimer}} \tag{9.19}$$

9.3.2. ENERGY SOURCE

The energy source term is modelled as shown by Missirilis [10]. The local heat source term is calculated with 9.20, where h_{local} is the local heat transfer coefficient, S_{exchange}, is the heat transfer area density and $T_{\text{wall}} - T$ is the difference between the wall and fluid bulk temperature. The max() operator is added to the original formulation to ensure that there can only be heat transfer to the cold side of the heat exchanger.

$$q_{\text{local}} = h_{\text{local}} \max\left([T_{\text{wall}} - T]; 0\right) S_{\text{exchange}} \tag{9.20}$$

Furthermore, the thermal conductivity of the porous zone is set to the fluid value, thereby omitting the solid material's aforementioned contribution to the thermal contribution. This is done to prevent upstream heat conduction inside the porous zone.

9.3.3. CALIBRATION

The calibration procedure uses the condenser rating model of the *HeXaCode*[63] software. For optimal heat exchanger design, the inflow conditions are varied to create with the model a data set which can be used to calibrate to source terms.

Momentum source calibration
This source term function can be fitted based on the values of inlet viscosity, μ_{in}, outlet density, ρ_{out}, and mean velocity, u_m for each data point. Figure 9.4 shows the data point and fit function. The transversal direction resistance coefficients are set equal to that of the axial direction times 1000, to mimic the high resistance of the flat tube walls.

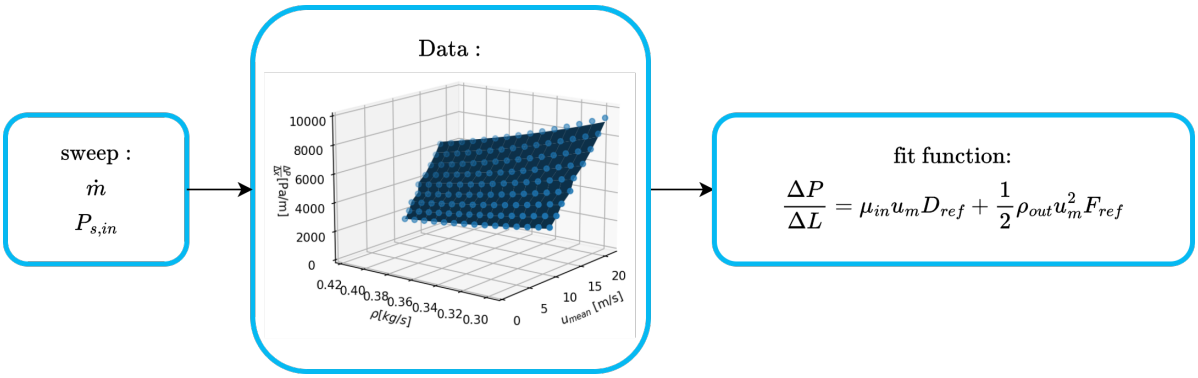

Figure 9.4: Calibration method for the coefficients of the momentum source

Energy Source calibration
The calibration of the energy source term is performed by fitting the Nusselt number function to the aforementioned dataset where the exponent of the Prandtl number is fixed to a value commonly used in literature. Figure 9.5 shows the data point and fit function. Furthermore, the other parameters that are used in the computation of the local heat source are extracted from the data produced by the condenser rating method of the *HeXaCode* [63] package. The method adopted to calculate the local heat source is explained in Section 3.4.3.

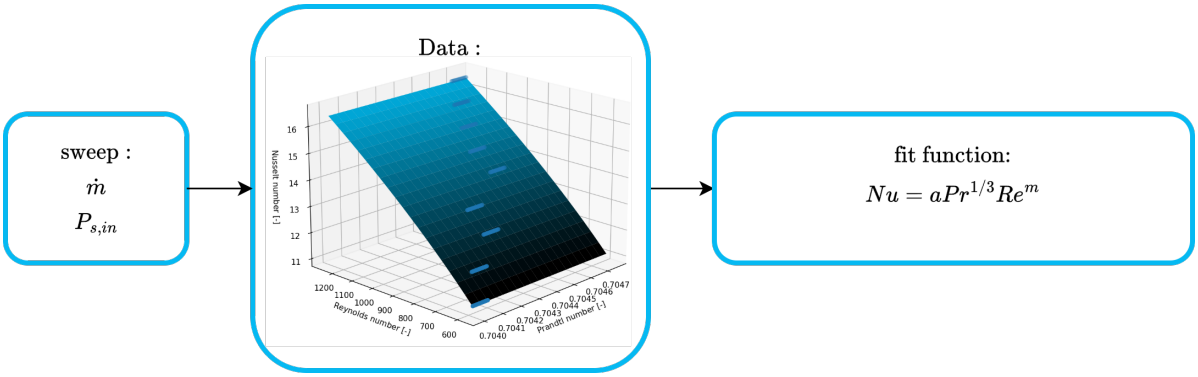

Figure 9.5: Calibration method for the Nusselt number correlation

9.4. VERIFICATION OF POROUS MEDIA MODELLING

The verification of the porous media implementation is performed by comparing the pressure drop and temperature increase obtained on a straight channel with a porous zone with the predictions of *HeXaCode* [63]. First, each model is tested by considering only one effect at a time, namely the porosity, resistance, heating and finally, an inclined inflow angle. Then quantitative verification is done by sweeping the inlet pressure and mass flow and comparing the static pressure drop, static temperature increase and velocity increase with *HeXaCode* [63].
For this verification, the same numerical settings are used as described in Section 9.2. In this situation, however, slip walls are used for all wall surfaces to remove the effect of wall friction from the results.

9.5. GRID CONVERGENCE STUDY

To inspect whether the results are invariant with respect to the grid size, a grid convergence study is carried out based on the work of Roache [69], which was later generalised by Celik et al. [70]. The method is based on

the Richardson extrapolation, which estimates the solution for an infinitely small grid size. This extrapolation is then used to calculate a Richardson error estimate. Roache [69] adds to this a safety factor constituting the grid convergence index, *GCI*. The safety factor recommended by Roache [69] for three-grid-sizes convergence studies is a conservative factor of 3. The same author suggests using a lower factor, namely 1.25, for higher-quality grid convergence studies with multiple grid sizes. The procedure of calculating the convergence index will be described in the following.

It is important to note that the grid convergence index is calculated on a set of three grid sizes; this implies that when performing the study on more than 3 grids, the Richardson error estimate is performed by considering only the simulation results for three grids at a time. In the following equations, the subscripts 1, 2, and 3 denote the variables corresponding to the fine, medium, and coarse grid, respectively.
The definition of the representative grid size h is given in Equation 9.21. By averaging the cell areas, it is possible to get a representative global cell size in the case when the mesh consists of elements of unequal size.

$$h = \left[\frac{1}{N} \sum_{i=1}^{N} (\Delta A_i) \right]^{1/2} \tag{9.21}$$

The next step is to define the values of ϵ and r, which are the differences between the numerical solution of two grid sizes and the refinement factor between the two grids, respectively. The definition of the two variables is given in Equations 9.22, 9.23, where the subscripts 1 and 2 can be substituted by subscripts 2 and 3, respectively. Here, the values ϕ are solution variables of the numerical simulation.

$$\epsilon_{21} = \phi_2 - \phi_1 \tag{9.22}$$

$$r_{12} = \frac{h_1}{h_2} \tag{9.23}$$

To find the order of convergence, Equations 9.24 are solved iteratively. Note that an oscillatory convergence is observed when $\epsilon_{32}/\epsilon_{21} < 0$.

$$p = \frac{1}{\ln(r_{21})} \left| \ln \left| \frac{\epsilon_{32}}{\epsilon_{21}} \right| \right| + q(p) \tag{9.24a}$$

$$q(p) = \ln \left(\frac{r_{21}^p - s}{r_{32}^p - s} \right) \tag{9.24b}$$

$$s = 1 \cdot \operatorname{sgn} \left(\frac{\epsilon_{32}}{\epsilon_{21}} \right) \tag{9.24c}$$

Now that the differences between the numerical solutions, ϵ, the refinement factors r and the order of convergence p are obtained, the extrapolated value, f_{ext}^{23}, of solution variable, ϕ, can be calculated using Equation 9.25.

$$f_{\text{ext}}^{21} = \frac{r_{21}^p \phi_1 - \phi_2}{r_{21}^p - 1} \tag{9.25}$$

Finally, three error estimates can be evaluated: The approximate relative error in Equation 9.26, the extrapolated relative error in Equation 9.27 and the fine-grid convergence index in Equation 9.28 which features the safety factor F_s. Furthermore, the asymptotic GCI can be evaluated using equation 9.29, which, when close to unity, indicates a grid-independent solution.

$$e_a^{21} = \left| \frac{\phi_1 - \phi_2}{\phi_1} \right| \tag{9.26}$$

$$e_{\text{ext}}^{21} = \left| \frac{\phi_{\text{ext}}^{12} - \phi_1}{\phi_{\text{ext}}^{12}} \right| \tag{9.27}$$

$$\text{GCI}_{\text{fine}}^{21} = \frac{F_s e_a^{21}}{r_{21}^p - 1} \tag{9.28}$$

$$\text{GCI}_{\text{asymptotic}} = \frac{\text{GCI}_{\text{fine}}^{32}}{r_{32}^p \text{GCI}_{\text{fine}}^{21}} \tag{9.29}$$

The choice of the solution variables will be discussed in the following. The solution variable that should be grid-independent is the drag recovery factor defined in Equation 8.1. The value of the nozzle thrust is determined by the mass flow rate and the velocity. Important quantities that play a role in determining the exit velocity are the total pressure drop and total temperature increase across the ram air duct. Another

important solution variable is the effective outlet area of the diffuser E introduced in Section 8.1.2. This quantity is important as it is related to the level of diffusion that occurs and the estimation of the separation point in the diffuser. Finally, as recommended by Celik et al. [70] and Roache [69], the safety factor of 1.25 will be used as the grid sensitivity study will be performed based on the simulation results obtained for multiple grid sizes.

9.6. COMPARISON WITH DUCT MODEL

To be able to compare the lumped parameter model with the detailed physics model, some data processing and measurement planes need to be established. This will be discussed in Section 9.6.1. Next to this, the boundary conditions prescribed in the detailed physics model need to match those of the lumped parameter model for a fair comparison. This procedure, as well as the method of data point generation, will be discussed in Section 9.6.2.

9.6.1. MEASUREMENT PLANES AND DATA PROCESSING

The data from the detailed physics model should be reduced to a singular value at each station before it can be compared to the lumped parameter model. This is done using the mass-weighted average value of a quantity, defined in Equation 9.30, using the built-in Ansys Fluent method.

$$\frac{\int \phi\rho|\vec{v}\cdot d\vec{A}|}{\int \rho|\vec{v}\cdot d\vec{A}|} = \frac{\sum_{i=1}^{n}\phi_i\rho_i\left|\vec{v}_i\cdot\vec{A}_i\right|}{\sum_{i=1}^{n}\rho_i\left|\vec{v}_i\cdot\vec{A}_i\right|} \tag{9.30}$$

Next to this, a uniformity index is extracted from the data of the detailed physics model to test the validity of the lumped assumption at each station. As calculated by Ansys Fluent, the mass-weighted uniformity index defined in Equations 9.31 and 9.32.

$$\gamma_m = 1 - \frac{\sum_{i=1}^{n}\left[\left(\left|\phi_i-\bar{\phi}_m\right|\right)\left(\left|\rho_i\vec{V}_i\cdot\vec{A}_i\right|\right)\right]}{2\left|\bar{\phi}_m\right|\sum_{i=1}^{n}\left[\left|\rho_i\vec{v}_i\cdot\vec{A}_i\right|\right]} \tag{9.31}$$

$$\bar{\phi}_m = \frac{\sum_{i=1}^{n}\left[\phi_i\left(\left|\rho_i\vec{v}_i\cdot\vec{A}_i\right|\right)\right]}{\sum_{i=1}^{n}\left[\left|\rho_i\vec{v}_i\cdot\vec{A}_i\right|\right]} \tag{9.32}$$

In these equations, the variable, Φ_i, indicates the quantity being considered. The integrals are approximated by summing all quantities over the total number of facets, n, in a given section of the CFD model where the index of each facet is given by i.

The measurement planes in which these average quantities are calculated are analogous to the station nomenclature introduced in Figure 8.2. Extra measurement planes are added to give more insight into the evolution of the fluid thermodynamic properties, namely a plane halfway through the diffuser, a plane just before the porous zone, a plane just after the porous zone and a plane halfway through the nozzle. This is shown in Figure 9.1.

9.6.2. DATA POINT GENERATION AND COMPARISON PROCEDURE

To be able to compare fairly the detailed physics model (DPM) and lumped parameter model (LPM), a procedure is required. This procedure is generalized for multiple design points and shown in Figure 9.6. The first step for the generation of the comparison database is the definition of the upper and lower bounds of the duct design variables as well as the total number of points. Thereafter, all unique combinations of these arrays are constructed. This set does not fully define a ram air duct geometry, and therefore the lumped parameter model in sizing mode is evaluated for each design point to find the heat exchanger depth, Z_{hex} and the outlet height of the nozzle, H_{outlet}. As all duct designs have different heat exchanger depths, the porous media needs to be calibrated before running the DPM simulation. Since the mass flow rate and inlet static pressure are not a direct input to the DPM, the LPM needs to match the inlet conditions of the DPM for a fair comparisson. To do so, both the mass flow rate ratio and the mass flow rate of the LPM are adjusted to match the inlet static pressure and mass flow rate of the DPM. Next to this, the heat exchanger depth,Z_{hex}, is also an input of the LPM model, and therefore *HeXaCode* [63] is used in rating mode. This process is repeated for each design point.

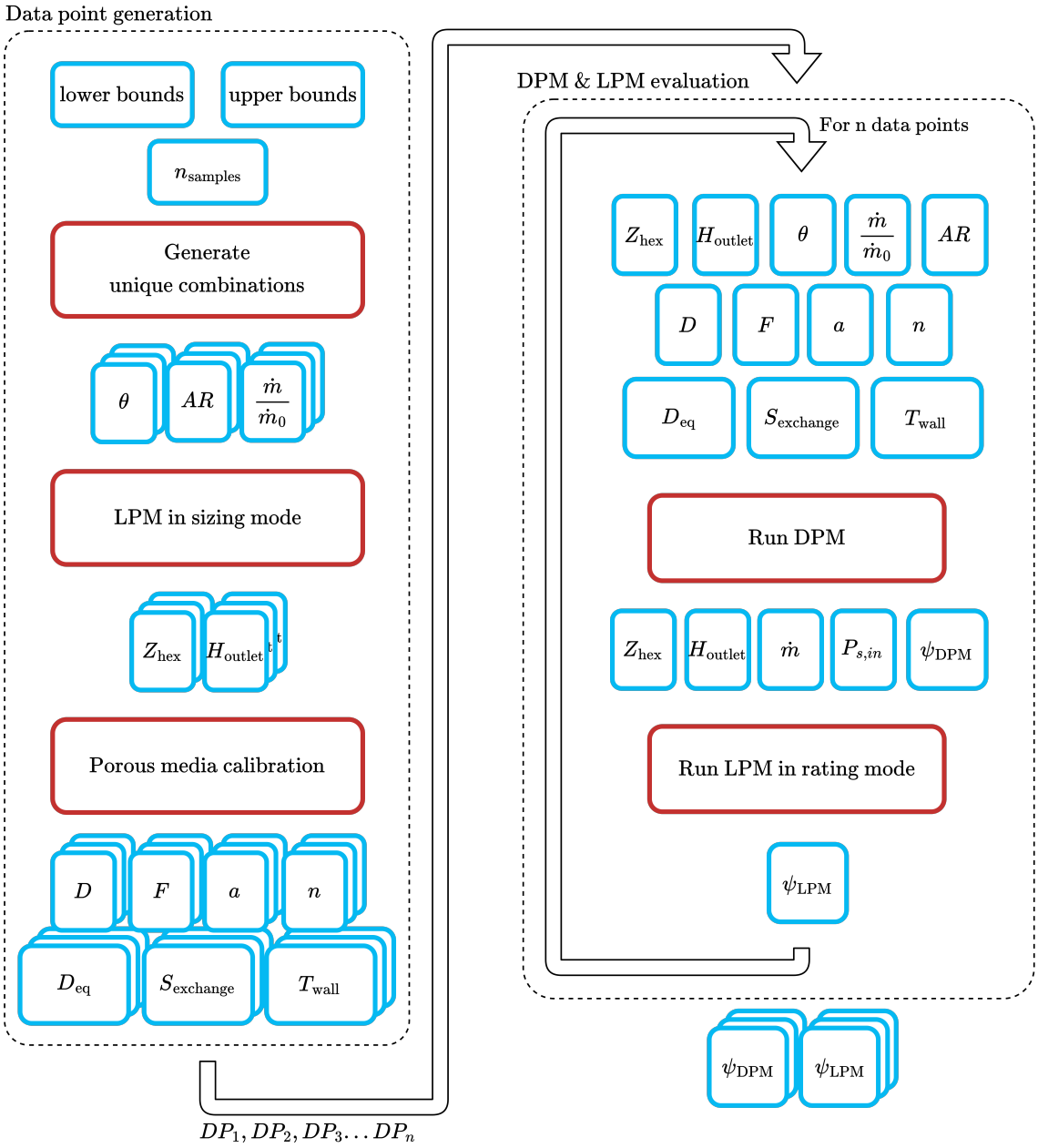

Figure 9.6: Procedure for generation and evaluation of design points

The upper and lower bounds of the sweep are shown in Table 9.3. The fin height, h_{fin}, is kept constant for simplicity as it has no considerable effect on the drag recovery factor, as found in the sensitivity study. For the generation of data points, each variable has 5 steps between its upper and lower bound, resulting in $5^3 = 125$ datapoints. As some of these points can possibly fall out of the range of validity of the used correlations in the LPM, it is expected that not all data points are evaluated.

Variable	Lower bound	Upper bound
$\dot{m}/\dot{m}_0$	0.7	0.7
AR	2	4
θ	50	70

Table 9.3: Variable bounds used for constructing the data points shown in Table B.2. AR is the diffuser area ratio, $\dot{m}/\dot{m}_0$, the mass flow rate ratio, θ, the inclination angle

III

RESULTS

10

Test Case Description: DRAGON Concept

In Section 1, the ONERA hybrid electric concept was introduced as the study's test case. This chapter delineates the boundary conditions and model inputs essential for result generation. Notably, the propulsion system incorporates a waste heat recovery Organic Rankine Cycle (ORC) within the electric generators mounted on the aircraft's tail, as depicted in Figure 8.1. The design features two condenser ducts per engine, totalling four condensers for the aircraft.

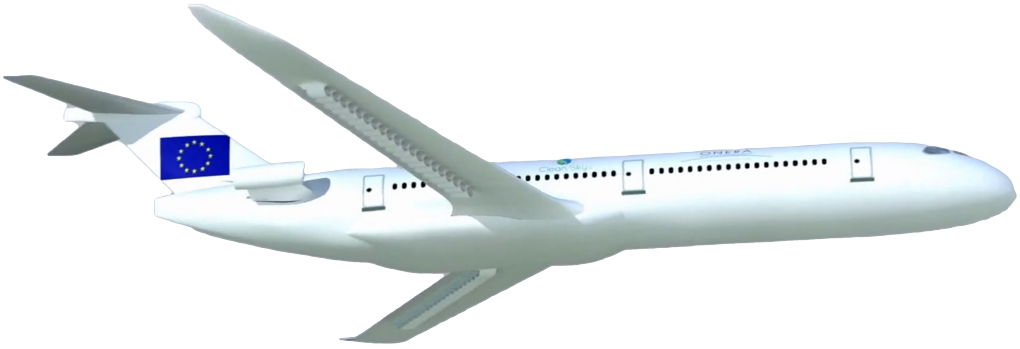

Figure 10.1: Side view of DRAGON concept, reproduced from [18]

The freestream conditions considered are consistent with those assumed in Schmollgruber et al. [23], performing a study on the same test case. More specifically, ISA+15@ 10000 m, with a freestream Mach number of 0.78. Furthermore, it is assumed that these freestream conditions remain unchanged up to the inlet of the ram air duct and that no boundary layer is affecting the intake performance. This assumption can be challenged by two factors. Firstly, the intake could be situated in the wake of upstream components, and secondly, the inlet conditions could be affected by the inlet lip and operating conditions of the turbogenerator itself.

Examination of Figure 10.1 reveals that the engine is positioned above the wings and away from the fuselage, suggesting that the intake of the ram air duct is likely not influenced by upstream components. The undisturbed airflow that reaches the engine nacelle is affected by the engine's inlet lip and operating point, thereby accelerating the airflow that reaches the inlet of the ram air duct. However, due to limited information about the inlet lip shapes, it is assumed that the engine inlet lip and duct intake location are designed to maintain a local Mach number equal to the freestream Mach number at the inlet. Additionally, it is assumed that there is minimal development of a boundary layer in front of the duct intake, thereby assuming that its effects are negligible.

Space constraints are determined using the publication of Krempus et al. [71], where the sizing of the waste heat recovery ORC is described. Here, it was assumed that each condenser ducting has a maximum width of 1.5 meters. Furthermore, a maximum length of 3 meters is assumed for the condenser ducting. No extra constraints are added regarding the maximum height of the condenser ducting.

The model inputs include performance constants and thermodynamic specification as well as the condenser heat duty. The inlet boundary layer thickness is assumed to be zero. The diffuser's blockage factor is configured to have a constant blocked area A_B. This implies that the blockage factor B_1 decreases when the inlet area grows. The total pressure ratio of the nozzle, η_{pt}, is set to 0.998, and the half angle of the nozzle, which is set to 15 deg. The discharge coefficient, C_{ds}, is set to 1 in the sensitivity study and constraint optimisation. Conversely, in comparing the lumped parameter model with the detailed physics model, the discharge coefficient is set to 0.986. The angularity coefficient C_v is set to 1 in both cases. Regarding the thermodynamic specification of the Organic Rankine Cycle, the heat duty, Q, is set to 728.427 [kW], the hotside properties, $T_h, P_h, \dot{m}_h$, to 454.59 [K], 541.770 [kPa] and 1.56 [kg/s] respectively, and the cold side mass flow rate, $\dot{m}$, to 6.94 [kg/s]. These variables are specified by an external method that optimises the Organic Rankine Cycle and is therefore assumed to be fixed in all cases. However, for the comparison of the lumped parameter model with the detailed physics model, the mass flow rate is not fixed. The reason for this is explained in Section 9.6.2 and resides in the fact that the boundary conditions used in the lumped parameter model do not constrain the mass flow rate.
Table 10.1 provides a summary of the test case specification and constraints. Table B.1 shows the microgeometry specification for each heat exchanger type.

Freestream conditions	Sizing	Rating	
$P_{s,\infty}$	26436 [Pa]		Freestream static pressure
$T_{s,\infty}$	238.15 [K]		Freestream static temperature
ρ_∞	0.38671 [kg/m^3]		Freestream density
M_∞	0.78 [-]		Cruise mach number
Duct			
$W_{\max}$	1.5 [m]		Max width of the condenser ducting
$L_{\max}$	3 [m]		Max length of the condenser ducting
Inlet			
δ	0 [m]		Boundary layer thickness
θ	0 [m]		Momentum boundary layer thickness
M_{loc}/M_∞	1.0 [-]		Local mach number ratio
Diffuser			
B_{in}	0.003 [-] @ H_2 = 0.1 [m]		Inlet blockage factor diffuser
AR_{max}	4 [-]		Maximum area ratio diffuser
Tilt			
θ_{max}	70 [deg]		Maximum tilt angle
Heat exchanger			
Q_{duty}	728.427 [kW]		Heat duty of single condenser
$\dot{m}_h$	1.56 [kg/s]		Hot side mass flow
$P_{s,h,in}$	541.770 [kPa]		Hotside inlet static pressure
$T_{s,h,in}$	454.59 [K]		Hotside inlet static temperature
$\dot{m}_c$	6.94 [kg/s]	-	Cold side mass flow
Nozzle			
C_a	1[-]	1[-]	Angularity coefficient
C_v	-	-	Velocity coefficient
C_{ds}	1[-]	0.986[-]	Discharge coefficient
α_d	15 [deg]		Nozzle half angle
η_{p_t}	0.998[-]		Total pressure ratio nozzle

Table 10.1: Data for the simulation of the test case considered

11

LONGITUDINAL MULTI-PASS CONDENSER RESULTS

As outlined in the methodology, the motivation for utilizing a longitudinal multipass condenser is to investigate whether altering the heat exchanger geometry per pass is advantageous compared to a singular pass configuration. It is hypothesized that the optimized multipass configuration will demonstrate a more controlled acceleration of flow velocity and variable geometrical parameters per pass, resulting in a lower-pressure drop across the heat exchanger compared to the single pass.

The results presented in Figure 11.1 illustrate the pressure drop characteristics of optimized heat exchanger geometries. The design vector comprises each pass's fin height or adimensional transversal pitch and the heat exchanger height. The baseline design is established, taking the mean value of the optimal solution for each individual heat exchanger of the multi-pass configuration.

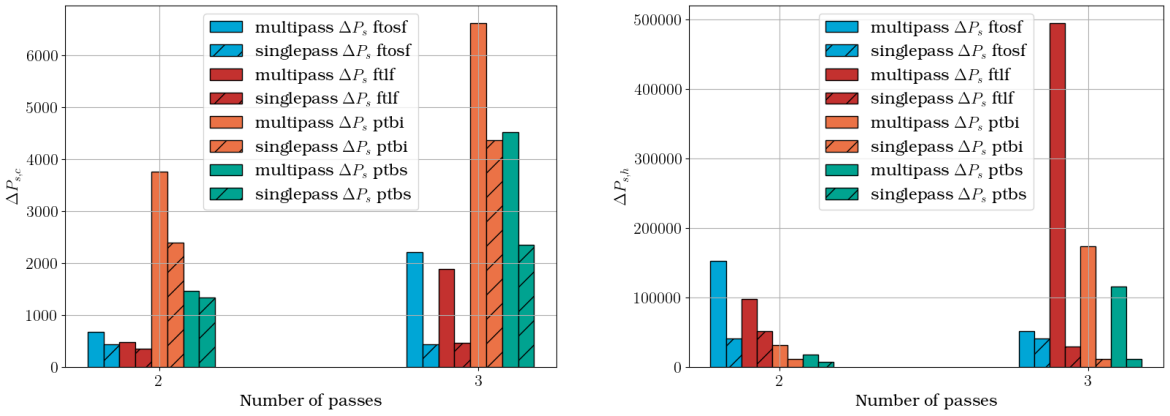

(a) Cold side pressure drop for all heat exchanger types considered. (b) Hot side pressure drop for all heat exchanger types considered.

Figure 11.1: Comparisson of single-pass versus multi-pass pressure drop performance for the hot and cold side.

From figure 11.1, it becomes obvious that, for this test case, there are no benefits in employing a longitudinal multi-pass configuration. As the cold-side pressure drop is similar or bigger for almost all heat exchanger types with two passes, the difference grows when using three passes. The hot-side pressure drop differences are even bigger. While the flat tube offset strip fin shows to be an outlier in the general trend, the hot side pressure drops are, especially for 3 passes, an order of magnitude larger. Moreover, it was observed that the optimizer did not vary the geometrical parameters per pass but attempted to maximize the face area of the heat exchanger and minimize the heat exchanger blockage factor as much as possible, essentially contradicting the hypothesis that predicted a varying geometry per pass.

From this, it can be concluded that there are no significant benefits on both sides of the condenser for employing a multipass configuration, at least for the analyzed application, and thereby answering research question 1a.

12

LUMPED PARAMETER MODEL RESULTS

In this chapter, the results of the lumped parameter model will be presented. In Section 12.1, the sensitivity of the drag recovery factor and ram air duct length to the duct geometrical parameters will be shown. Furthermore, in this section, the sensitivity of the drag recovery factor to the local inlet Mach number will be shown. Thereafter, in Section 12.2, the results of the optimal preliminary design of the ram air duct for varying length constraints and diffuser blocked area fractions will be presented. The combined results of these two analysis will contribute to answering the second research sub-question 1b in Section 12.3.

12.1. SENSITIVITY ANALYSIS

Figures 12.1,C.1,C.2 and C.3 show sensitivities of the geometrical parameters to the drag recovery factor for all considered heat exchanger types. Next to that, the figures show the sensitivity of the geometrical parameters to the length of the ram air duct with white contour lines. The infeasible points due to geometries generating conditions outisde the correlation bounds of the lumped parameter model are demarked by the hashed pattern. Figure 12.2, shows the effect of the local inlet Mach number on the drag recovery factor.

The duct length is most affected by the area ratio of the diffuser and, in a lesser manner, by the mass flow rate ratio and the inclination angle. The effect of the fin height on the duct length is very small.

The effect of the area ratio is explained by the relationship shown in Figure 8.10, where for higher area ratios, the diffuser length increases. The effect of the mass flow rate ratio ties into the fact that it specifies the area ratio between the ingested stream tube- and the inlet area. As the mass flow rate and freestream conditions are constant in this analysis, this means that the ingested stream tube area is constant. Therefore a decrease in mass flow rate ratio increases the inlet area. For a constant-width ram air duct, an increase in inlet area translates to an increase in inlet height which contributes to the length of the ram air duct in two ways. First, for a given area ratio, the diffuser length is proportional to the inlet height, assuming a constant diffuser half angle. Second, the increase in inlet height corresponds to an increase in diffuser outlet height, H_3, and is proportional to the height of the heat exchanger, H_4, which subsequently contributes to the ram air duct length with a factor $\tan(\theta)$, the tangent of the inclination angle. Moreover, the diffuser outlet height H_3 and heat exchanger height H_4 are related to each other by the inverse cosine of the inclination angle, $(\cos(\theta))^{-1}$. This, therefore, also explains the effect of an increase in inclination angle on the ram air duct length.
The effect of fin height on the duct length is related to the heat transfer coefficient and surface compactness computed by *HeXaCode* [63]. More in detail, as the product of the average air heat transfer coefficient, h, and surface compactness, β_1 decreases, the heat exchanger volume V has to increase to reject the same amount of heat, see Equation 12.1. As the frontal area of the heat exchanger is fixed by the diffuser area ratio, mass flow rate ratio and inclination angle, an increase in heat exchanger volume implies that the depth of the heat exchanger needs to increase. The increase in heat exchanger depth contributes to the length of the ram air duct proportionally to the cosine of the inclination angle.

$$Q = h\beta_1 V(T_{\text{wall}} - T_{\text{air}}) \tag{12.1}$$

The Drag Recovery Factor is most affected by the area ratio and inclination angle of the heat exchanger and, in a lesser manner, by the mass flow rate ratio and only marginally by the fin height.

Increasing the diffuser area ratio leads to a decreasing rate of improvement in the drag recovery factor, as can be observed from Figures 12.1(c) and 12.1(d). This can be explained by the effective outlet area correlation shown in Figure 8.11, where increasing area ratio has an increasingly declining effect on the effective outlet area fraction E_2 and translates to a decrease in static pressure rise and increases total pressure losses across the diffuser.

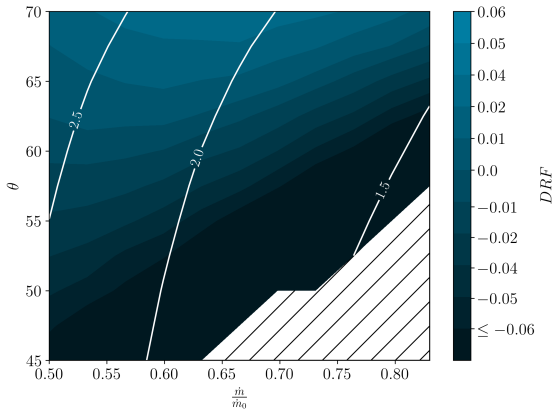

(a) Sensitivity to the inclination angle θ and mass flow rate ratio $\dot{m}/\dot{m}_0$ for $AR = 3$ & $h_{\text{fin}} = 0.0077$.

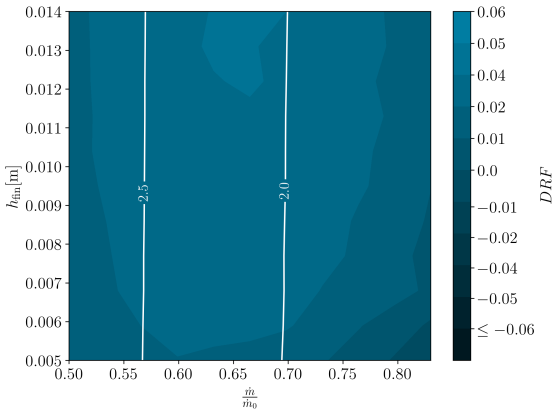

(b) Sensitivity to the fin height h_{fin} and mass flow rate ratio $\dot{m}/\dot{m}_0$ for $AR = 3$ & $\theta = 70$.

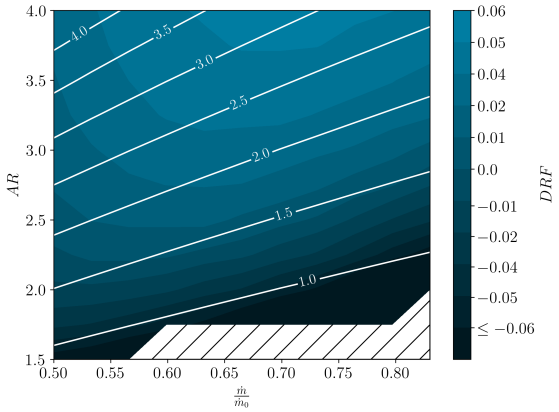

(c) Sensitivity to the diffuser area ratio AR and mass flow rate ratio $\dot{m}/\dot{m}_0$ for $\theta = 70$ & $h_{\text{fin}} = 0.0077$.

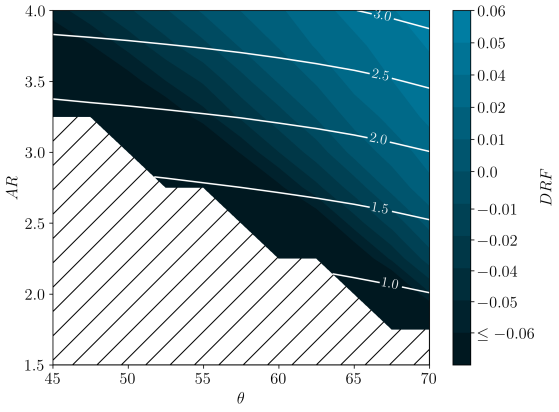

(d) Sensitivity to the diffuser area ratio AR and inclination angle θ for $\dot{m}/\dot{m}_0 = 0.7$ & $h_{\text{fin}} = 0.0077$.

Figure 12.1: Drag Recovery Factor, Equation 8.1, sensitivity w.r.t the geometrical input variables. The white contour lines represent the duct length in meters.. The ranges used for the parameter sweep are shown in Table 8.2 as well as the constant values used to slice the multivariable design space.

The inclination angle also has a declining positive effect when its value is increased; see Figures 12.1(d) and 12.1(a). Reviewing the correlation used in the tilt model (see Figure B.10) indicates that the extra pressure drop due to tilting the heat exchanger increases more sharply at higher inclination angles. Additionally, the decrease in velocity within the tilt component becomes more pronounced as the inclination angle increases. Therefore, it can be concluded that the benefits of further reduction in heat exchanger inlet velocity increasingly outweigh the penalties due to extra pressure drop.

The effect of the mass flow rate ratio is best characterized as a balance between the total pressure drop across the duct and the intake drag. In more detail, an increase in mass flow rate ratio reduces the intake drag as the inlet area decreases, and for mass flow rate ratios higher than ~ 0.7, the spillage drag component reduces to

zero. Conversely, an increase in mass flow rate ratio decreases the amount of pre-diffusion before the intake and thereby increases the mean velocity in the ram air duct, in turn increasing total pressure losses across it. These combined effects seemingly provide a range of mass flow rate ratios where the effect on the drag recovery factor are comparable in magnitude, see Figure 12.1(b), between a mass flow rate ratio of ~ 0.62 and ~ 0.70. Moreover, this balance between internal losses and external drag can also be found in Figure 12.1(c) where the drag recovery factor is nearly constant across a constant ram air duct length between 2.5 and 3 meters.

The effect of the fin height is not easily characterized by a single trend, however, showing a range of optimal values between $0.012[\text{m}] < h_{\text{fin}} < 0.014[\text{m}]$ as shown in Figure 12.1(b). Increasing the fin height reduces velocities in the heat exchanger through a higher heat exchanger blockage factor and thereby decreasing frictional losses. However, as mentioned before, an increase in fin height can also reduce the rejected heat per unit volume. The latter increases the depth of the heat exchanger and increases the pressure drop across it.

An increase in local inlet Mach number decreases the drag recovery factor as shown in Figure 12.2. This is explained by the fact that for higher local Mach numbers, the mean velocity in the ram air duct increases and thereby increases the total pressure drop across it. More in detail, an increase in the local Mach number at a fixed mass flow rate ratio causes a greater portion of the total pressure to be in the form of dynamic pressure, which is associated with larger total pressure losses.

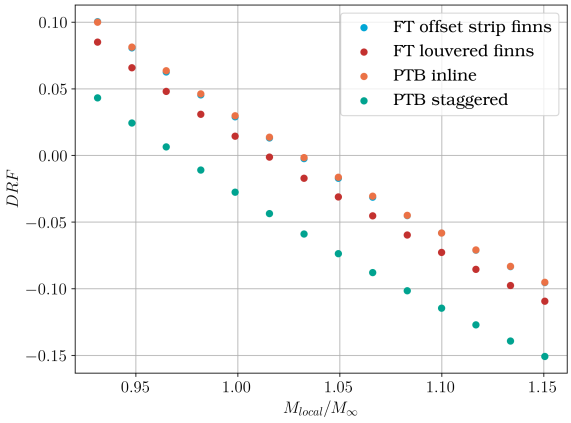

Figure 12.2: Local mach number plotted versus Drag Recovery Factor using constant geometrical parameters: AR = 3.8 [-], $\dot{m}/\dot{m}_0$ = 0.7 [-], θ = 70 [deg], h_{fin} = 0.014 [m]

In conclusion, it can be stated that inclining the heat exchanger is the most space-efficient way of increasing the drag recovery factor; while the diffuser area has a similar effect on the drag recovery factor, it offers a larger penalty on the ram air duct length. Furthermore, the local Mach number significantly affects the drag recovery factor through increased total pressure losses in the ram air duct. This, therefore, motivates careful consideration of positioning the intake of the ram air duct.

12.2. OPTIMIAL PRELIMINARY DESIGN OF THE RAM AIR DUCT

The results of the investigation into the optimal preliminary design of the ram air duct will be presented in this section. First, to compare different heat exchanger types, the evolution of the optimal design with varying maximum length constraints will be discussed in Section 12.2.1. Second, by varying the blocked area fraction at the inlet of the diffuser, the effect of the ingested boundary layer size on the optimal duct design will be shown in Section 12.2.2.

12.2.1. DIFFERENT HEAT EXCHANGER TYPES

From Figure 12.3(a), it is observed that the drag recovery factor values plateau for all heat exchanger types at a certain L_{max}. The reason of this trend can be understood when looking at Figure 12.4(b), where the points of $L_{\text{duct}}/L_{\text{max}} < 1$ coincide with the start of the plateau in drag recovery factor for each heat exchanger type respectively. More in detail, the differences in the position where the plateau starts can be attributed to the

fact that certain heat exchanger types offer a more compact solution than others, as their optimal designs allow for shorter ducts. Concretely, the flat tube offset strip fin and inline plain tube bundle heat exchanger types reach the unconstraint optimal design at the lowest $L_{\max}$ for similar drag recovery factors, with the inline plain tube bundle offering a lighter solution with a difference of ~ 5 kg.

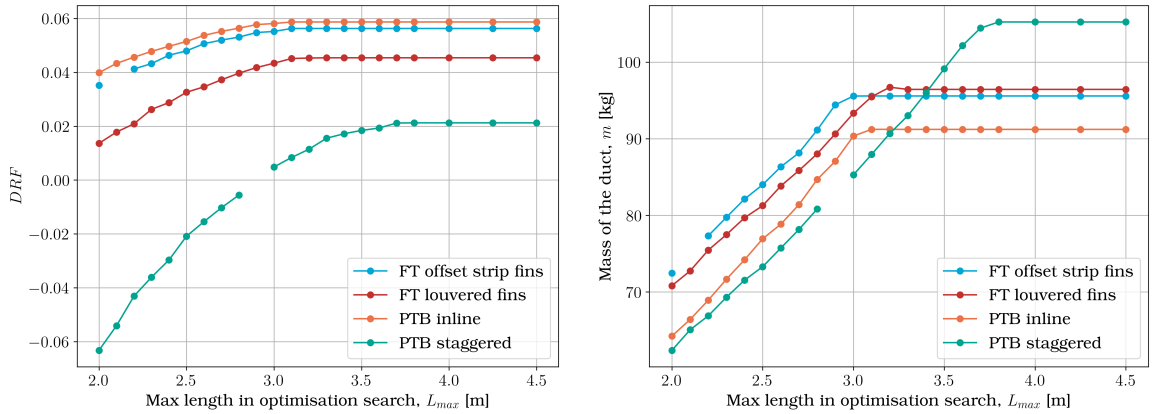

(a) Drag Recovery Factor of each optimized geometry for varying maximum length

(b) Mass of duct of each optimized geometry for varying maximum length

Figure 12.3: Drag Recovery Factor, Equation 8.1, and duct mass optimized duct geometry per heat exchanger type and varying maximum length.

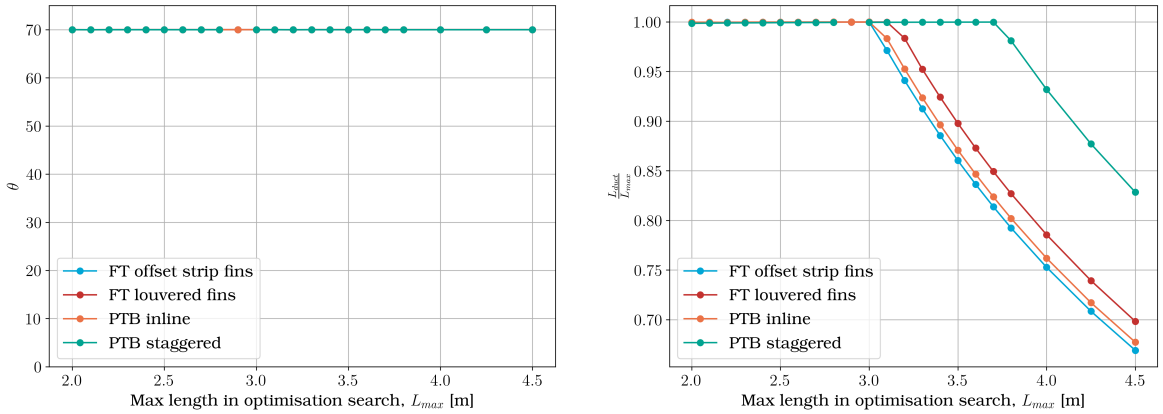

(a) Inclination angle, θ, of each optimized geometry for varying maximum length

(b) Ratio of ram air duct length versus maximum length constraint of each optimized geometry for varying maximum length

Figure 12.4: Geometrical parameters for optimized duct geometry per heat exchanger type and varying maximum length.

Furthermore, it can be seen from Figure 12.4(a) that the inclination angle is always maximized regardless of the length constraint. This observation is coherent with the conclusions from the sensitivity study, which found that it is the most space-efficient way of increasing the drag recovery factor.
The mass flow rate ratio increases and decreases in the range of $2[\text{m}] < L_{\max} < 3[\text{m}]$ as shown in Figure 12.5(b). In this range the diffuser area ratio AR increases from 3 to 4. Projecting the trends of mass flow rate ratio and diffuser area ratio onto Figure 12.1(c) highlights how the mass flow rate ratio has little sensitivity on the drag recovery factor until the ram air duct length is higher than $L_{\max} = 2.5[\text{m}]$. This is the same point at which the mass flow rate ratio starts to decrease again in Figure 12.5(b). Physically, this can be explained by the fact that increasing the mass flow rate ratio decreases the inlet area and, therefore, decreases intake drag. This increase in mass flow rate ratio also reduces the amount of pre-diffusion before the inlet, which is compensated by an increase in the diffuser area ratio. The combined effect, therefore, yields increasing drag recovery factors.

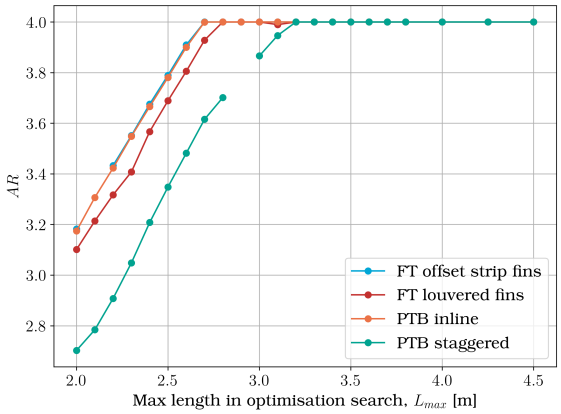

(a) Diffuser area ratio of each optimized geometry for varying maximum length

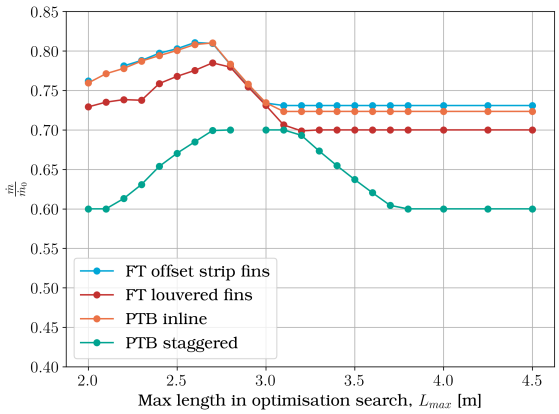

(b) mass flow rate ratio, $\dot{m}/\dot{m}_0$, of each optimized geometry for varying maximum length

Figure 12.5: Geometrical parameters for optimized duct geometry per heat exchanger type and varying maximum length.

12.2.2. VARYING BLOCKED AREA FRACTION INLET DIFFUSER

By varying the blocked area fraction, B, the effect of a boundary layer on the drag recovery factor of the optimal duct design can be investigated. From Figure 12.6(a), it can be observed that the blocked area fraction has a significant impact on the drag recovery factor. On top of this, it also increases the point at which the optimal ram air duct geometry is unaffected by the constraint on $L_{\max}$, as shown in Figure 12.6(b).

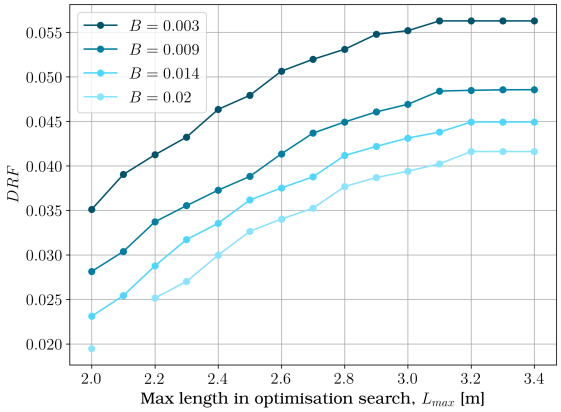

(a) Inclination angle, θ, for varying diffuser blocked area fraction and maximum length

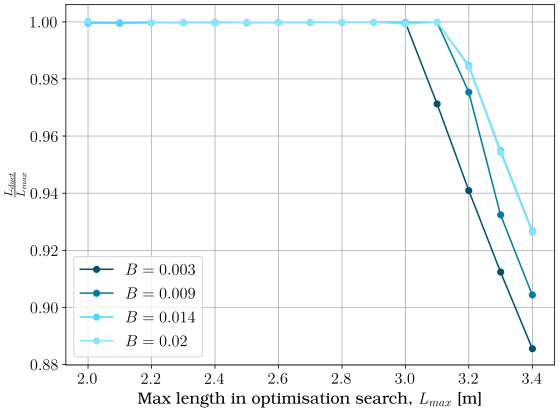

(b) Ratio of ram air duct length versus maximum length constraint for varying diffuser blocked area fraction and maximum length

Figure 12.6: Geometrical parameters and drag recovery factor for optimized duct geometry using the flat tube offset strip fin heat exchanger for varying diffuser blocked inlet fractions.

The results in Figure 12.7(b) show that as the blocked area fraction decreases, the trend of the optimal mass flow rate ratio tends to flatten. From a certain blocked area fraction, the values of the mass flow rate ratio thus appear to be unaffected by the length constraint and lie close to the point for which the maximum pre-diffusion is achieved without extra spillage drag. With this, recommendations can be made for optimal ram air duct geometry in case of appreciable boundary layers at the inlet. Namely, maximizing the inclination angle of the heat exchanger, selecting a mass flow rate ratio that has maximum pre-diffusion and no spillage drag and increasing the area ratio of the diffuser according to the maximum allowed ram air duct length lead to the best ram air duct design.

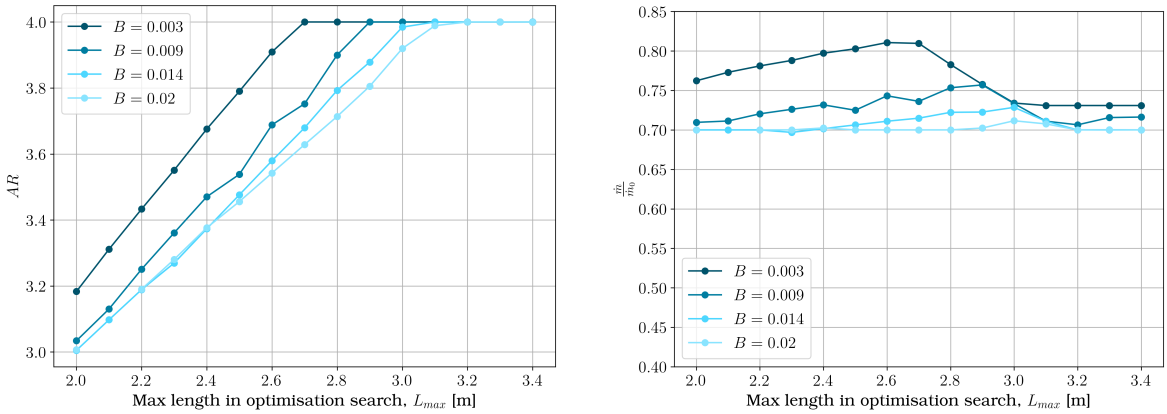

(a) Diffuser area ratio, AR, for varying diffuser blocked area fraction and maximum length

(b) mass flow rate ratio, $\dot{m}/\dot{m}_0$, for varying diffuser blocked area fraction and maximum length

Figure 12.7: Geometrical parameters and drag recovery factor for optimized duct geometry using the flat tube offset strip fin heat exchanger for varying diffuser blocked inlet fractions

The reason for inconsistencies in the found results is related to the chosen optimisation algorithm and sensitivity of the drag recovery factor to the geometrical parameters. The optimization algorithm is gradient-based and it found optima are therefore, dependent on initial design vectors and convergence criteria. The sensitivity study has shown that some design variables have a significantly greater effect on the drag recovery factor and ram air duct length than others. Moreover, sensitivities of the mass flow rate ratio show a generally small gradient with respect to the drag recovery factor while having a relatively high influence on the ram air duct length. As the drag recovery factor and ram air duct length are used in the objective and constraint function, respectively, it is therefore expected that the gradient-based optimizer can have issues with converging to an optimum design vector. By this rationale large inconsistencies are removed from the shown results.

12.3. CONCLUSION TO THE SENSITIVITY ANALYSIS AND CONSTRAINT SPACE OPTIMISATION

The results of the sensitivity study and optimal preliminary ram air duct design show that regardless of heat exchanger type and length constraint, the inclination angle should be maximized. Next to this, it is shown that local inlet conditions significantly affect the drag recovery factor, creating a recommendation for placing the inlet of the ram air duct in a location of low local Mach number and a small boundary layer. Moreover, for blocked area ratios of about $B > 0.02$, optimal duct design is characterized by choosing a maximum heat exchanger inclination angle, a mass flow ratio that offers maximum pre-diffusion without spillage drag and increasing the diffuser area ratio up to the allowed maximum length of the ram air duct.
Finally, among the analysed heat exchanger types, the inline plain tube bundle and the flat tube offset strip fin heat exchanger types prove to be the most suitable for exploiting the Meredith effect on the IMOTHEP DRAGON concept. When also considering the duct's mass, the inline plain tube bundle, considering the model assumptions, is arguably the best heat exchanger type to use. However, as the difference in mass between the two heat exchanger types is small, the flat tube offset strip fin heat exchanger will be used in further analysis.

13

Detailed Physics Model Results

In this chapter, the results of the detailed physics model will be discussed. First, the verification of the porous media modelling is discussed in Section 13.1, showing the individual contributions of the porous media to the flow and the differences in static pressure decrease, static temperature increase and velocity increase between *HeXaCode* [63] and the porous media model. Thereafter, the grid convergence study results are shown in Section 13.2, exploring the sensitivity to the grid size of the total pressure drop across the duct, the total temperature increase and the effective outlet area fraction of the diffuser. In Section 13.3, the lumped parameter model (LPM) and detailed physics model (DPM) will be compared, first by analysing the results for the optimal geometry found in Section 12 and second by analysing the differences in the predictions of the two models for multiple design solutions differing in diffuser area ratio, mass flow rate ratio and heat exchanger inclination angle. Finally, in Section 13.4, conclusions will be presented to answer the sub-research questions 1c and 1d.

13.1. Verification of Porous Media

The implemented porous media model is verified by comparing the CFD results obtained for a straight channel with the prediction of the *HeXacode*[63] model. Moreover, to verify that each contribution of the porous zone is implemented correctly, different CFD simulations are performed to isolate the effect of the porosity and each source term. To understand the effect of inclined flow on the porous zone, another test case is added with an inclination angle θ of 70 degrees. Figure 13.1 shows the geometry of the test case and the position at which the profiles reported in Figure 13.2 are sampled. The geometry and inlet conditions of the heat exchanger are extracted from the results of the constraint optimisation when the maximum duct length is limited to 3 meters. This gives a L of 0.0964 [m] and a heat exchanger height Y of 0.765 [m]. Finally, the process variables are normalized with their respective inlet value for each test case, giving the normalised total temperature, T_t^*, the normalised total gauge pressure, P_t^*, the normalised velocity magnitude, V_{mag}^*, the normalised x-velocity, V_x^* and the normalised y-velocity, V_y^*.

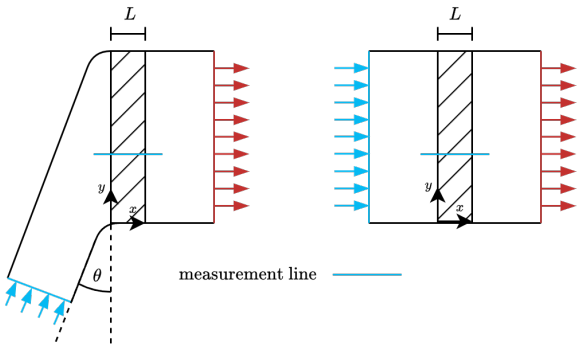

Figure 13.1: Sketch of test case setup for the inclined and straight duct, where θ is set to 70 degrees. The hatched box represents the porous medium, and the blue and red arrows indicate the inlet and outlet, respectively

The hypothesis is that with only porosity activated, there will solely be an increase in velocity proportional to the reciprocal of the porosity, which, in this case, is equal to 1.27002. With the momentum source term activated, there should be a decrease in total pressure. With the addition of the energy source term, the results should show an extra increase in velocity inside the porous zone and an increase in total temperature. In the case of a tilted heat exchanger, the flow is no longer aligned with the least resistive path in the porous zone. At that point, the velocity in the y direction is expected to dissipate and thus go to zero. The x velocity, on the other hand, will follow an evolution similar to that of the velocity magnitude of the straight duct case. As a consequence thereof, it is expected that a total pressure drop will occur at the inlet of the porous zone.

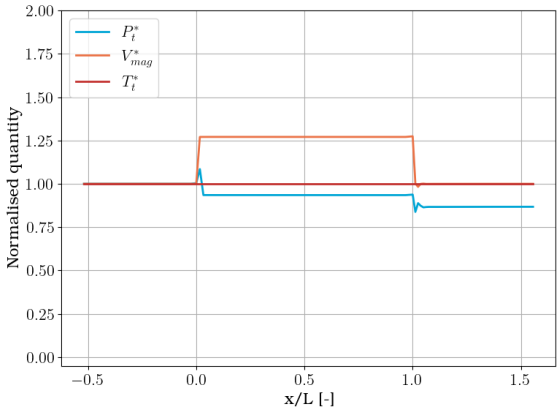

(a) Profiles of normalized quantities for straight duct test-case with only porosity activated.

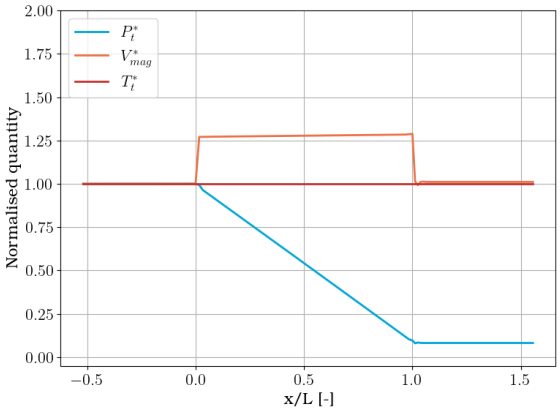

(b) Profiles of normalized quantities for straight duct test-case with porosity and resistance

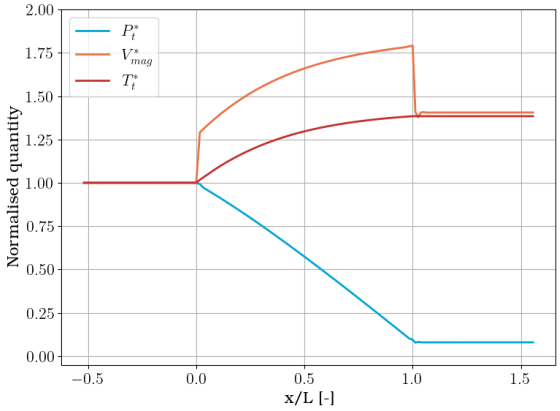

(c) Profiles of normalized quantities for straight duct test-case with porosity, resistance, and heating.

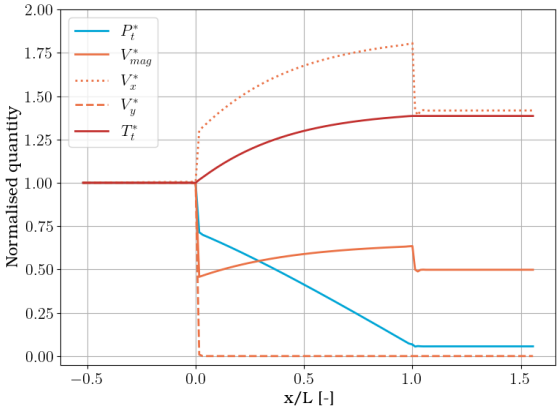

(d) Profiles of normalized quantities for inclined duct test-case with porosity, resistance, and heating

Figure 13.2: Profiles of normalized quantities for different duct test cases for the measurement line drawn in Figure 13.1.L is the depth of the porous zone

This is confirmed by the results in Figure 13.2. A closer inspection of the results in the same figure also highlights the presence of pressure and velocity oscillations upon entry and exit of the porous zone. To rule out the possibility of numerical errors, the test case shown in Figure 13.2(c) was performed for multiple grid sizes. It was found that the oscillations were only squished in the x direction with a decrease in cell size. However, the magnitude of these oscillations did not significantly change. The results of this investigation can be found in Appendix D and Figures D.1, D.2, D.3.

To further verify the implementation, the simulation is repeated for different inlet pressures and mass flows. These results are compared with the predictions of the *HeXaCode* [63] model for the same design specifications. The difference in the predicted values of the inlet and outlet static pressure, total temperature and velocity magnitude are plotted in Figure 13.3.

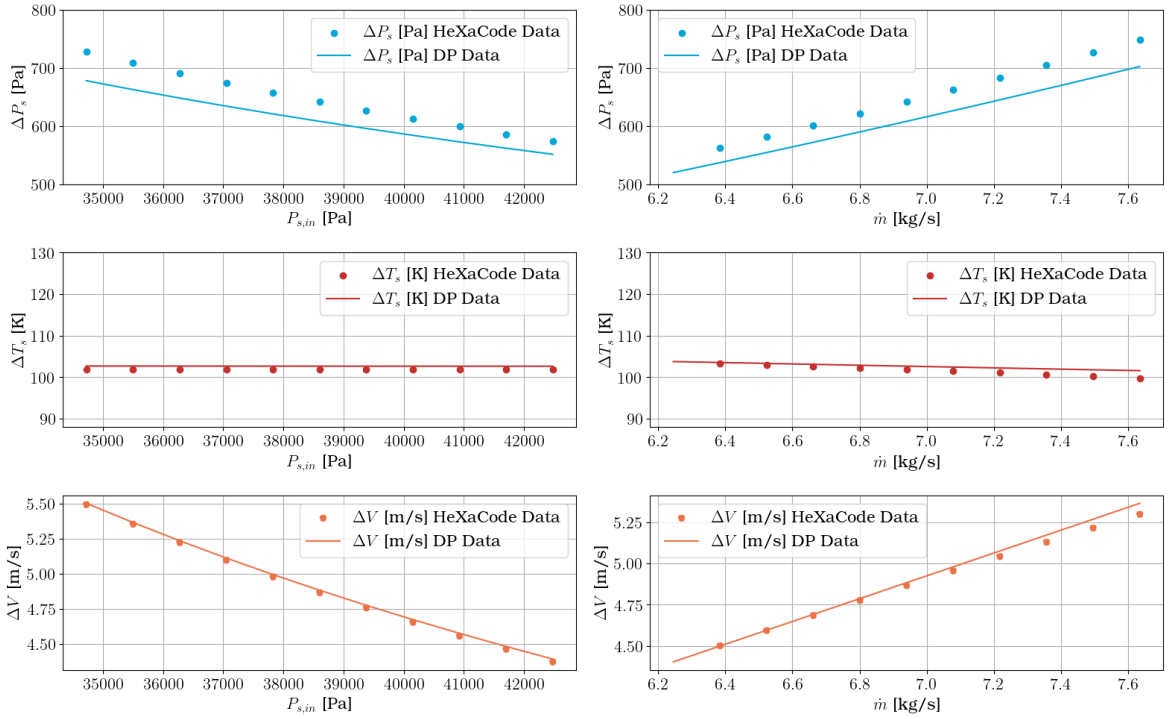

Figure 13.3: Calibration verification between HeXaCode predictions and the porous media model for the straight duct test case for varying inlet mass flow and varying inlet static pressure.

It is observed that the velocity and total temperature predicted by the detailed physics model for the straight duct test case are in agreement with the estimates of *HeXaCode* [63]. The static pressure, however, shows more deviation. The mean relative errors are summarized in Table 13.1. The reason for the difference in pressure drop was extensively investigated, but no conclusive evidence was found to explain it.
Nonetheless, it is hypothesized that this could be due to the pressure losses at the entrance and exit of the heat exchanger, something which is not explicetly modelled in the porous media. Moreover, the porous media model incorporates these losses by the calibrated momentum source term. Since the loss factors are directly proportional to the specific velocity at the entry and exit of the heat exchanger, they, by definition, do not scale with the average velocity. On top of that, for this specific application, the heat exchanger is relatively thin, meaning that entry and exit losses play a significant role in the overall pressure drop across the heat exchanger.

Varied quantity	ΔP_s error	ΔT_s error	ΔV error
$P_{s,in}$	-5.293 %	0.765 %	0.331 %
$\dot{m}$	-5.299 %	0.933 %	0.493 %

Table 13.1: Percentual error between HeXaCode data and the straight duct test case data using the HeXaCode data as reference.

13.2. GRID CONVERGENCE STUDY

With the implementation of the porous zone being verified, the next step is to perform the grid convergence study. As mentioned in Section 9.5, the important parameters that need to be grid invariant are the total pressure drop, the total temperature increase and the effective area fraction of the diffuser outlet. In Figure 13.4, the quantities are plotted against the cell count for each mesh. In this plot, the extrapolated value is plotted, and an uncertainty band is provided by the fine grid convergence index, GCI_{fine}^{21}, of the finest grid. In Table 13.2, the results of the grid convergence study are summarized for the chosen grid size while in Tables D.1,D.2,D.3 full results are reported. It is important to note that in the grid convergence study procedure, as explained in Section 9.5, Celik et al. [70] recommends refinement ratios over 1.3. The latter implies that from the 11 simulated grids, every other grid needs to be skipped to comply with refinement ratios higher than

1.3, giving two full sets of grids to perform the study on. (Giving two sets of grids: Set 1,3,5,7,9,11 and set 2,4,6,8,10)

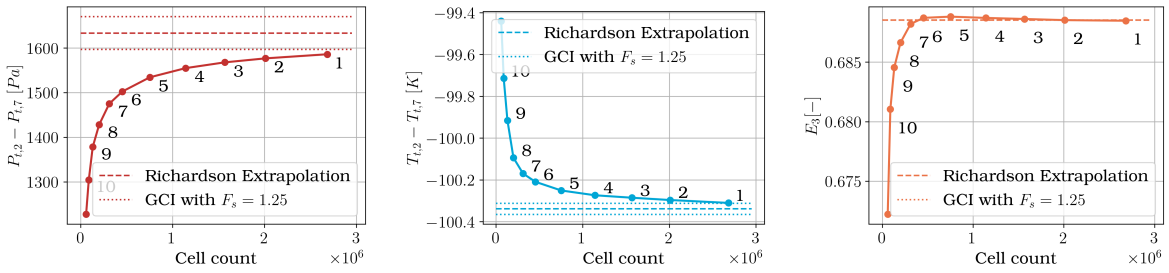

(a) ΔP_t for varying grid sizes.

(b) ΔT_t for varying grid sizes.

(c) E_3 for varying grid sizes.

Figure 13.4: Plot of all considered quantities for varying grid sizes. The plot includes the Richardson extrapolation value and corresponding uncertainty ranges based on the fine grid convergence index, GCI_{fine}, calculated with Equation 9.28 with safety factor $F_s = 1.25$.

As one can see, the effective area fraction and the rise in total temperature converge well. Thus, the corresponding uncertainty estimated in the Richardson extrapolation is low. However, for the total pressure drop, the uncertainty is larger, and the relative error is relatively high as well. While the CGIs of the effective area fraction and total temperature increase are well below 1 per cent, the CGI of the delta total pressure is in the order of 5 per cent. Further grid refinement has shown that the solution is converging towards the extrapolated value, however, at a high computational cost.

Variable		ϕ	N_{cells}	r	GCI	$GCI_{\text{asymptotic}}$	p	$\phi_{\text{extrapolated}}$
	Grid 4	1.555e+03	1142241	1.6	6.35%			
ΔP_t	Grid 6	1.50e+03	454358	1.5	10.93%	1.035	1.11	1.63e+03
	Grid 8	1.43e+03	201302	-	-			
	Grid 4	6.887e-01	1142241	1.6	0.00%			
E_3	Grid 6	6.89e-01	454358	1.5	0.00%	1.002	14.43	6.89e-01
	Grid 8	6.87e-01	201302	-	-			
	Grid 4	-1.003e+02	1142241	1.6	0.07%			
ΔT_t	Grid 6	-1.00e+02	454358	1.5	0.15%	1.001	1.63	-1.00e+02
	Grid 8	-1.00e+02	201302	-	-			

Table 13.2: Grid convergence study based on the results of 3 grids. Full results can be found in Tables D.1,D.2,D.3. ϕ represents the variable considered in the first column and $\phi_{\text{extrapolated}}$ its extrapolated value. N_{cells} is the number of grid elements, r the refinement ratio between two successive grids. GCI is the grid convergence index in percent and its asymptotic value is provided by $GCI_{\text{asymptotic}}$, where a value close to unity indicates a grid-independent solution. The order achieved in the simulation is given by p.

As mentioned by Celik et al. [70], a grid-independent solution is indicated by a value of $GCI_{\text{asymptotic}}$ close to one, meaning that further gird refinement is not affecting the solution variable significantly anymore. Therefore, the size of grid number 4 is deemed a good compromise between computational cost and accuracy.

13.3. COMPARISON WITH LUMPED PARAMETER MODEL

In this Section, the results of the lumped parameter model (LPM) will be compared to the results of the detailed physics model (DPM). First, the two models are compared for a single design point and thereafter for multiple design points. The geometry used for the single design point comparison is the optimum FTOSF heat exchanger duct geometry for a maximum length of 3 meters. The geometrical specifications of this design solution are shown in Table B.2 and are indicated as design point zero (DP0).

13.3.1. PER-STATION COMPARISSON

Figure 13.5, shows the thermodynamic quantities at each station throughout the ram air duct are shown, where the station nomenclature is defined in Figure 8.2. Next to this, the figure also shows the mass-weighted uniformity index of the static pressure, static temperature, density and velocity for each station. With this index, the lumped assumption used in the LPM can be challenged. Here, it is observed that only the velocity shows large non-uniformities, while all other quantities are well-uniform to be represented by a single lumped value. The implication of the non-uniform velocity profile is that the total pressure will also vary across a cross-section in the ram air duct.

In the upcoming discussion, trends of the thermodynamic quantities will be discussed per component of the ram air duct, starting with the diffuser. Finally, the total pressure drop, as well as the drag recovery factor, will be analyzed.

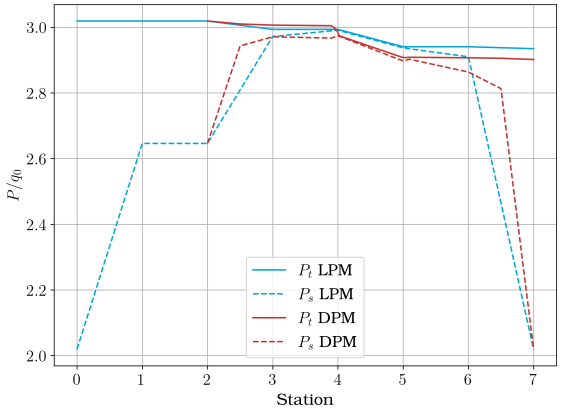

(a) Static and total pressure for each station.

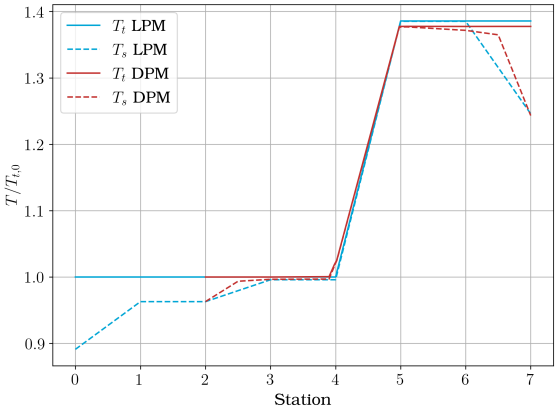

(b) Static and total temperature for each station.

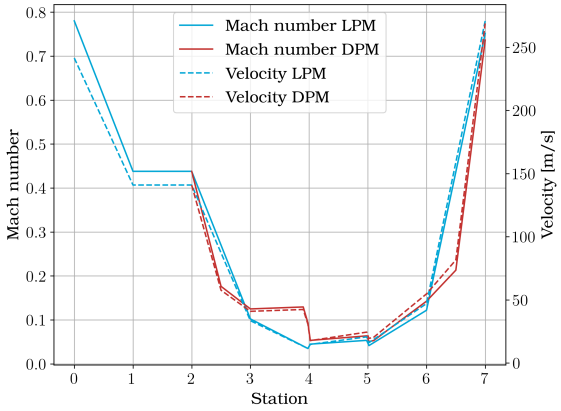

(c) Velocity and Mach number for each station.

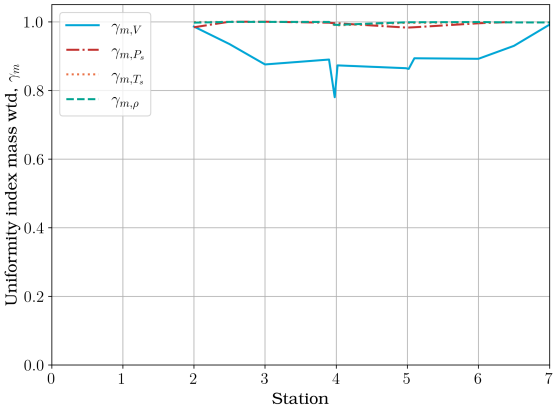

(d) Mass weighted uniformity index for selected quantities.

Figure 13.5: Thermodynamic quantities for design point zero (DP0) for each station. Station nomenclature is provided in Figure 8.2.

DIFFUSER

From Figure 13.5(a), a non-linear trend in static pressure rise of the DPM is observed. This is to be expected as the used correlation in Figure 8.11 also shows a non-linear decrease with area ratio. This trend is also reflected in the velocity, Mach number and static temperature shown in Figures 13.5(b) and 13.5(c). Furthermore, it is observed that the static pressure at the outlet of the diffuser is similar, while total pressure is lower for the LPM, resulting in higher velocities at the diffuser outlet as reported by the DPM. The difference in total pressure is possibly explained by checking the validity of the assumption taken in the LPM in calculating the total pressure at the outlet of the diffuser, namely, uniform static pressure and temperature at the diffuser outlet and that the effective area fraction at the inlet and outlet delineates the inviscid core (see Section 8.1.2 for more details). From Figure 13.5(d), it is observed that at the outlet of the diffuser, the mass-weighted uniformity indexes of the static pressure and temperature are near the unity, indicating that the first two assumptions are correct. The third assumption made is that the effective outlet area A_E delineates the inviscid core of the diffuser flow. From the sketch in Figure 13.6, it is shown that the effective outlet area, A_E, does not, by definition, coincide with the edges of the boundary layer. Moreover, A_E is defined as the area required for the given mass flow rate with a flow velocity equal to the mean velocity of the fluid at that station. Hence, this area will always be larger than the area delimited by the edges of the boundary layer.

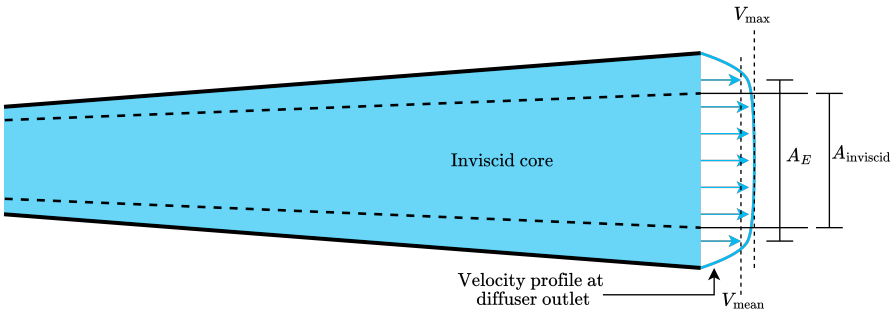

Figure 13.6: Sketch of the diffuser outlet velocity profile with the difference between effective area A_E and inviscid core at the outlet of the diffuser.

HEAT EXCHANGER TILT

In the tilt section, the LPM and DPM show opposing trends; while the static pressure of the LPM increases due to assumed perfect diffusion, the static pressure of the DPM is nearly constant. Moreover the DPM flow velocity even increases in the tilt section. The latter is explained when inspecting the velocity contours shown in Figure 13.7, where it is observed that the core flow contracts towards the end of the diffuser and tilt region. Regarding the trends of total pressure, the LPM reports no change, while the DPM shows a large total pressure drop just in front of the heat exchanger. This total pressure drop is explained by the fact that the transversal velocity component is dissipated upon entering the porous zone, as seen in the results of the verification in Section 13.1. The dissipation of the transversal velocity component is reflected in Figure 13.5(c), where the velocity magnitude decreases sharply just in front of the heat exchanger. Conversely, the LPM shows an increase in velocity, which can be explained by the combined effect of assumed uniform inflow and the blockage effect of the heat exchanger.

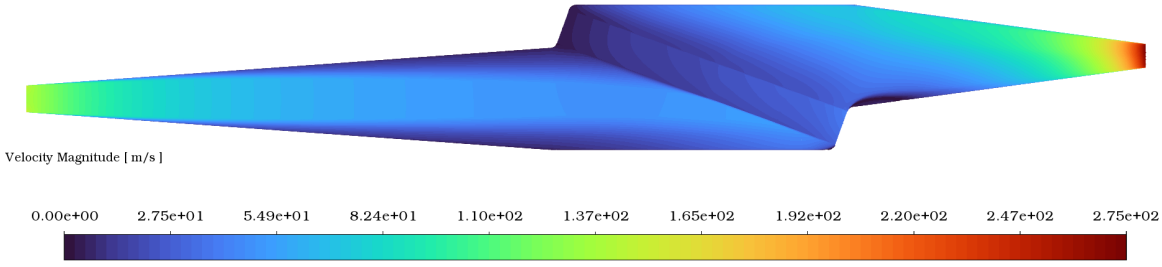

Figure 13.7: Velocity contour of DP0

Furthermore, from Figure 13.5(b) it is observed that just in front of the heat exchanger the DPM shows an increase in total temperature. This indicates that the flow is non-adiabatic. To further verify why this happens, profiles of the velocity magnitude, total temperature and effective thermal conductivity just in front of the heat exchanger are shown in Figure 13.8. The quantities are normalized as defined in equation 13.1. This figure shows that the total temperature increase is only present at locations of high effective thermal conductivity and low velocity. In light of this and considering that the maximum effective conductivity is four orders of magnitude higher than the air thermal conductivity at that temperature, it can be concluded that the total temperature increase is due to upstream heat transport.
To inspect why this effective thermal conductivity is so high, it is good to reiterate that the effective thermal conductivity, K_{eff} includes a turbulent contribution, as shown in Equation 9.16. Comparing the turbulent kinetic energy of the straight duct test case, where no upstream heating was present, with the full duct simulation reveals that there is a large difference between the two, as shown in Figures D.4 and D.5. The key difference here is that the straight duct features no diffuser and, thus, the presence of the diffuser can be the reason why upstream heating is present in the full duct simulation. A caveat here is that it is not possible to conclude whether the magnitude of upstream heating is realistic as there is no validation case available.

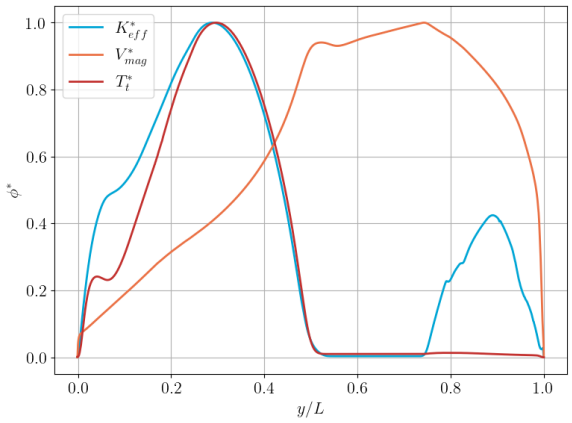

Figure 13.8: Nondimensionalized values of velocity magnitude V^*_{mag}, effective thermal conductivity K^*_{eff} and total temperature T^*_t just before the beginning of the porous zone. The quantities are nondimensionalized using Equation 13.1, where ϕ^* are the nondimensional values, y the coordinate aligned with the heat exchanger height L.

$$\phi^* = \frac{\phi(y) - \phi_{min}}{\phi_{max} - \phi_{min}} \tag{13.1}$$

	$K_{\text{eff}}[W/(mK)]$	$T_t[K]$	$V_{\text{mag}}[m/s]$
Max value	36.4378	276.209	54.2355
Min value	0.0238428	267.171	0.0

Table 13.3: Maximum and minimum values of the nondimensionalized quantities shown in Figure 13.8

HEAT EXCHANGER

At the heat exchanger inlet, the static pressure is close to its stagnation value for both models, with the LPM reporting higher total pressures. Next to this, there is a difference in the inlet temperature due to upstream heating and a low value for the mass-weighted uniformity index of the velocity because of the two-dimensional velocity profile at the diffuser outlet predicted by the DPM. These differences contribute to the mismatch in total temperature increase across the heat exchanger estimated by the two models. The higher inlet temperature of the DPM decreases the mean temperature difference with the specified wall temperature and thereby reduces the magnitude of the energy source term computed with Equation 3.49. Due to the non-uniform inlet velocity, there are zones of the heat exchanger with a lower mass flux and have, therefore, a faster-decreasing temperature difference with the specified wall temperature. This faster-decreasing temperature difference then contributes to an overall lower heat transfer rate and, thus, a smaller increase in total temperature of the

airflow.

The difference in the velocity at the heat exchanger inlet contributes to the difference in total pressure drop across the heat exchanger. This is explained by the Darcy-Forchheimer equation (see Eq. 9.17), where a higher mean velocity translates to higher static pressure drops. Regarding the velocity trends in the heat exchanger, both models show a similar increase in velocity inside the heat exchanger as well as a similar decrease in velocity upon exiting the heat exchanger due to an increase in flow area.

NOZZLE

From the exit of the heat exchanger up to the exit of the nozzle, the DPM reports a non-linear increase in velocity and a non-linear decrease in static pressure and temperature, which can be explained in two ways. First of all, by the Mach number-based isentropic flow relation shown in Equation 8.5 where the static pressure has a non-linear response to increasing Mach number. Secondly, by the separation bubble shown in Figure 13.7 at the beginning of the nozzle at the bottom wall. This separation effectively reduces the flow area, resulting in the first part of the nozzle experiencing a stronger converging effect, thereafter, a lesser converging effect and finally, a converging dictated by only the geometry again. Here, it is good to mention that the measurement plane between stations 6 and 7 is after this bubble.

TOTAL PRESSURE DROP PER COMPONENT

Before looking at the total pressure drop per component, it is good to reiterate that the drag recovery factor computed for the DPM uses the intake drag computed by the lumped parameter model.
The values reported in Figure 13.9(a) are very similar, showing only a 0.8% difference with the DPM reporting ~ 4.0% more thrust than drag. Figure 13.9(b) shows that between the models, there is a total pressure drop difference of 3.30 % of the ingested stream tube dynamic pressure. Next to that, the diffuser + tilt total pressure drop is reported to be lower by the LPM, mostly governed by the difference in the total pressure drop due to tilting heat exchanger. The total pressure drop reported by the DPM across the heat exchanger is expected to be lower than the total pressure drop reported by the LPM for the same inlet conditions, as shown in the verification in Section 13.1. Nonetheless, the LPM reports a higher total pressure drop in this section, explained by the discrepancy in inlet velocity between the models, shown in Figure 13.5(c). The total pressure drops in the tilt + nozzle component are similar between the models.

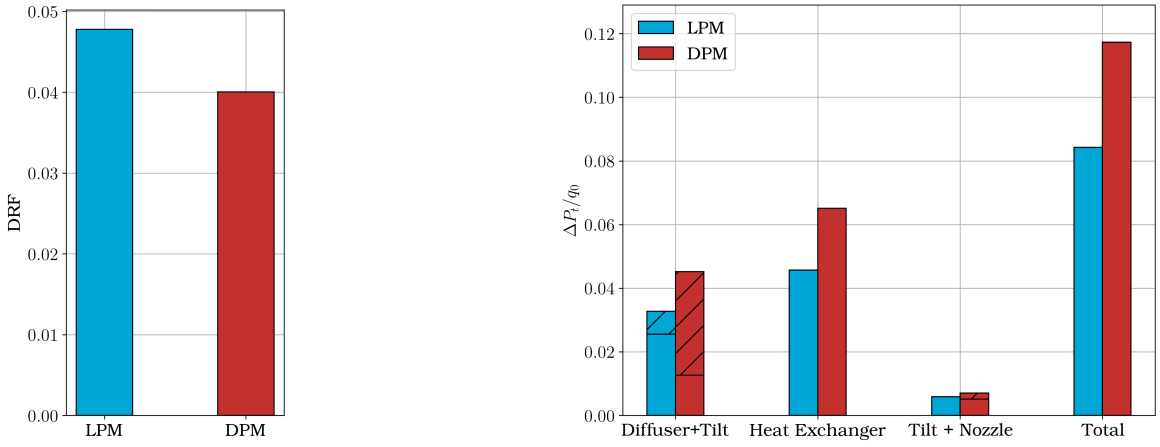

(a) Drag recovery factors of the LPM and DPM.

(b) Total pressure drop bins of the LPM and DPM.

Figure 13.9: Drag Recovery factor, Equation 8.1, and pressure drop predicted by the lumped parameter model and the detailed physics model for data point zero DP0, where the hatched portion of the bar is the contribution of the tilt to the total pressure drop of that component.

13.3.2. MULTIPLE DESIGN POINT COMPARISSON

A comparison between the two models over multiple design points will be discussed in this section. The creation of the data points was discussed in Section 9.6.2, where in Table 9.3, the bounds of the parameter sweep are shown. As mentioned in that section, not all created points were feasible. As a consequence, there are 89 data points left out of the 125 possible design combinations. Furthermore, not all of the 89 design points were evaluated with the DPM due to high computational costs per data point. In Table B.2 the data points are shown starting from $DP1$.

The results will be discussed by first looking at the reported drag recovery factors, whereafter discrepancies between the models will be discussed in analogy to the previous section.
In the following figures, the non-dimensional heat exchanger height defined in equation 13.2 is used. When the product of Equation 13.2 is multiplied by the height of the ingested stream tube H_0, it gives the heat exchanger height H_4. This is particularly useful as the height of the ingested stream tube H_0 is constrained by specified mass flow and the width of the duct.

$$\frac{H_0}{H_4} = \left(\frac{\dot{m}}{\dot{m}_0}\right)^{-1} \frac{AR}{\cos(\theta)} \tag{13.2}$$

Next to this, in the proceeding text, pressure quantities with the superscript ϕ^* are normalized with the ingested stream tube dynamic pressure and temperature quantities with the superscript ϕ^* are normalized with the total temperature of the ingested stream tube.

DRAG RECOVERY FACTOR

The DPM and LPM are in good agreement on the prediction of the drag recovery coefficient as shown in Figure 13.10, where the mean absolute difference between the models is 1.081% with a standard deviation of 0.584%. Furthermore, it is observed that there is an increase in the drag recovery factor with increasing area ratio and inclination angle. These trends are also identified in the sensitivity study, shown in Section 8.2. Next to that, for high values of diffuser area ratio and inclination angles, the drag recovery factor trends reach a plateau for mass flow rate ratios between 0.6 and 0.6. Finally, it is found that the effect of the inclination angle at lower diffuser area ratios is more effective than at higher diffuser area ratios, showing a steeper gradient with respect to the inclination angles at these lower diffuser area ratios.

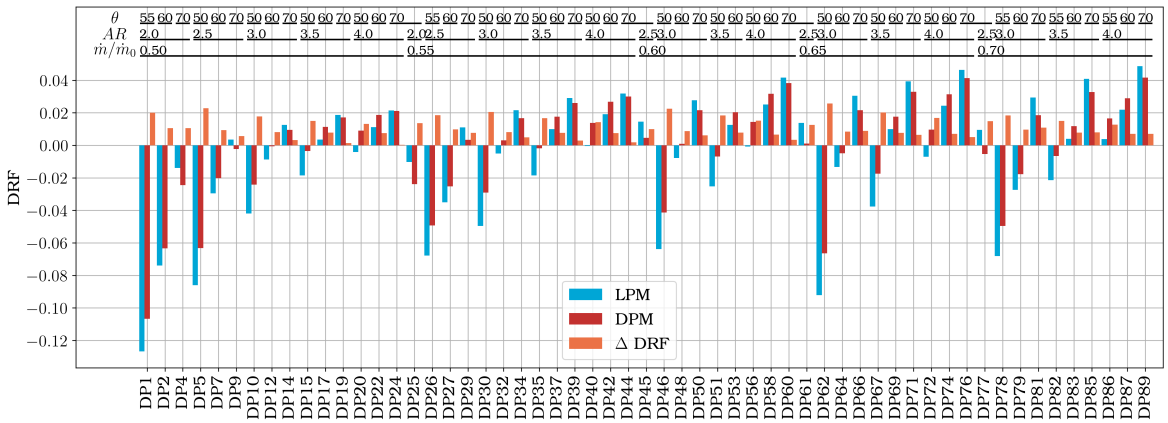

Figure 13.10: Drag recovery factor computed by the DPM and LPM, for multiple data points and differences between the two DRF estimates in orange; this can be interpreted as a percentage of the drag. At the top of the figure, the labels indicate what geometrical input each data point has.

DIFFUSER AND HEAT EXCHANGER TILT

The overall differences in total pressure drop across the diffuser and tilt between the models are shown in Figure 13.11. The mean absolute difference between the models is 0.78 % of the ingested free stream dynamic pressure. Furthermore, it can be seen that for higher heat exchanger inclination angles, the total pressure drop differences are generally larger, while for higher diffuser area ratios, the differences generally decrease. To inspect the origins of these deviations, the diffuser and tilt components will be discussed separately in the upcoming section.

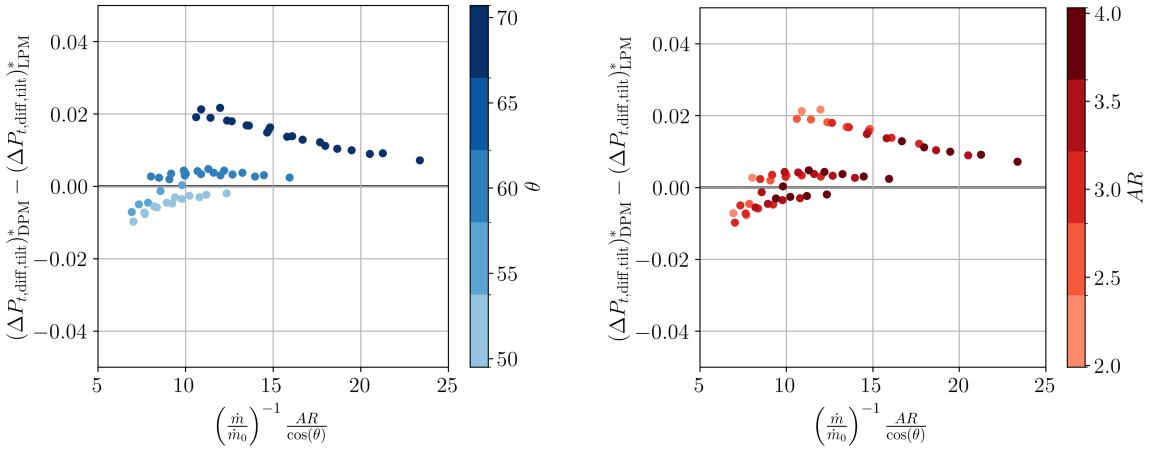

(a) (b)

Figure 13.11: Differences in total pressure drop in the diffuser and tilt between the two models normalized with the dynamic pressure of the ingested stream tube. The two subfigures show the inclination angle of the heat exchanger, θ, and the diffuser area ratio AR

Diffuser

Figure 13.12 shows the differences between the static and total pressure coefficients of the diffuser are shown. The coefficients are defined in Equations 13.3 and 13.4, where $\bar{q}_2$ is the dynamic pressure at the inlet of the diffuser and ΔP_s, ΔP_t and Δq the absolute differences in static, total and dynamic pressure between the inlet and outlet of the diffuser. The coefficients represent the portion of dynamic pressure that is converted to static pressure, highlighting how much dynamic pressure is lost in that conversion. The root mean square difference in static pressure coefficient amounts to 0.011, whereas the root mean square difference in total pressure coefficient is 0.043. This shows that the models roughly agree on the conversion of dynamic pressure to static pressure; however, less so on what portion of this dynamic pressure is lost.

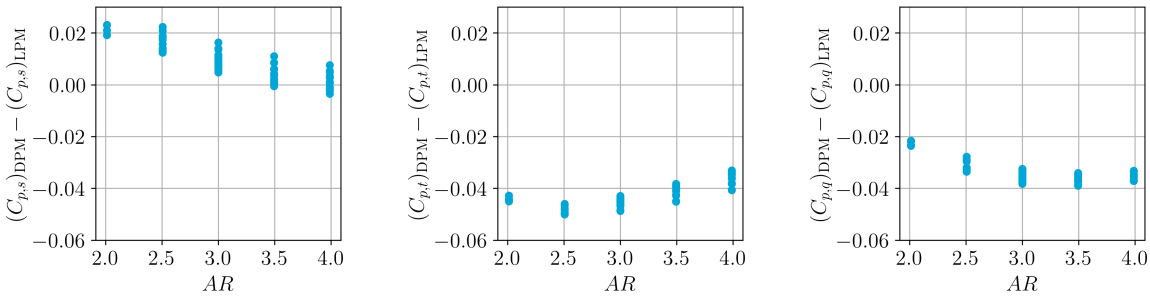

(a) Static pressure coefficient difference.

(b) Total pressure coefficient difference.

(c) Dynamic pressure coefficient difference.

Figure 13.12: Absolute difference of diffuser total and static pressure coefficient between the LPM and DPM, where $C_{p,\text{static}}$ is defined in Equation 13.3, $C_{p,\text{total}}$ is defined in Equation 13.4 and $C_{p,\text{dynamic}}$ is defined in Equation 13.5.

As mentioned in the preceding section, the difference in total pressure loss across the diffuser can be explained by the assumptions of the lumped parameter model. Across all evaluated data points, the mean values of the mass-weighted uniformity indices for the static pressure and static temperature are 0.9998 and 0.9996, respectively. This further reinforces the suspicion that the differences in total pressure at the diffuser outlet are due to the assumption of the effective outlet area A_E at the inlet and outlet delineating the inviscid core flow.

$$C_{p,\text{static}} = \frac{|\Delta P_s|}{\bar{q}_2} \quad (13.3) \qquad C_{p,\text{total}} = \frac{|\Delta P_t|}{\bar{q}_2} \quad (13.4) \qquad C_{p,\text{dynamic}} = \frac{|\Delta q|}{\bar{q}_2} \quad (13.5)$$

Next to this, the scatter for a single area ratio in Figure 13.12 shows that the diffuser performance does not only depend on the area ratio. To further inspect this, Figure 13.13 is introduced, showing the computed effective outlet area fraction, E_3, by the DPM versus the input variables, AR and B_2, the diffuser area ratio and diffuser inlet blocked area fraction respectively. Here, it can be observed that the effective outlet area fraction E_3 is dependent on the mass flow rate ratio and inclination angle, implying that the diffuser is also affected by these geometrical variables. As the diffuser inlet blocked area fraction, B_2 is scaled according to the height of the diffuser inlet, the parameter $AR(100B_2)^{1/4}$ also changes as a function of the different diffuser inlet heights. Furthermore, it is observed that the inclination angle has a similar effect on the effective outlet fraction E_3 as the mass flow rate ratio $\dot{m}/\dot{m}_0$.

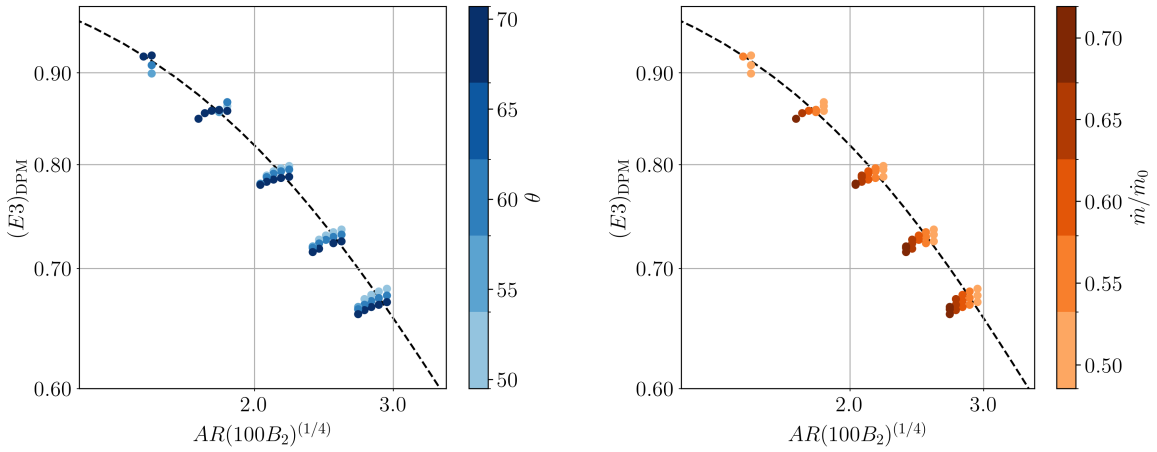

Figure 13.13: Effective outlet area fraction E_3 found by the DPM versus $AR(100B_2)^{1/4}$. The relation between E_3 and $AR(100B_2)^{1/4}$ presented by Sovran and Klomp [17] is denoted by the dashed line. The colours of the scatter points denote the inclination angle θ and mass flow rate ratio $\frac{\dot{m}}{\dot{m}_0}$ of that design point.

The increase in the mass flow rate ratio translates to a change in diffuser throat Reynolds number, varying between $2.7 \cdot 10^5 < (H_2 V_2 \rho_2)/\mu_2 < 2.8 \cdot 10^5$, and a change in diffuser inlet aspect ratio, varying between $15.1 < AS < 21.2$. The range of Reynolds numbers is an order of magnitude higher than the data used in Sovran and Komp [17]. However, Reneau et al. [16] state in their publication that for throat Reynold numbers higher than $Re_{H_2} > 10^4$, the inlet velocity profile and inflow turbulence are the most important parameters that determine the performance of the diffuser. On top of that, Pittaluga [37], in his correlation for straight-walled diffusers, omits the Reynolds dependent term for throat Reynolds number higher than $Re_{H_2} > 2.5 \cdot 10^5$. Similarly, Reneau et al. [16] state that the aspect ratio does not affect diffuser performance at these ranges ($15.1 < AS < 21.2$), where it must be noted that the CFD results represent an infinite aspect ratio as side walls are omitted in the simulation. The combined statements on the effect of throat Reynolds number and Aspect ratio somewhat contradict the found results of the present investigation as it seems that there is an effect of diffuser throat Reynolds number and Aspect Ratio on the effective outlet area fraction and, therefore, the performance of the diffuser.

A possible explanation of the mass flow rate ratio's effect is that the heat exchanger inclination's effect on the effective outlet area is Reynolds number dependent, where the effect of increasing the inclination angle is

most likely explained by the combined effect of the heat exchanger's resistance and orientation. However, this is impossible to fully verify with the current dataset.

Heat exchanger tilt

A larger difference between the models is observed in the computation of the extra total pressure drop due to tilting the heat exchanger, as shown in Figure 13.14. In this figure, the predictions of the two models have an opposing trend with respect to the inclination angle. On top of this it is observed that the total pressure drop due to inclining the heat exchanger only roughly aligns for low inclination angles.

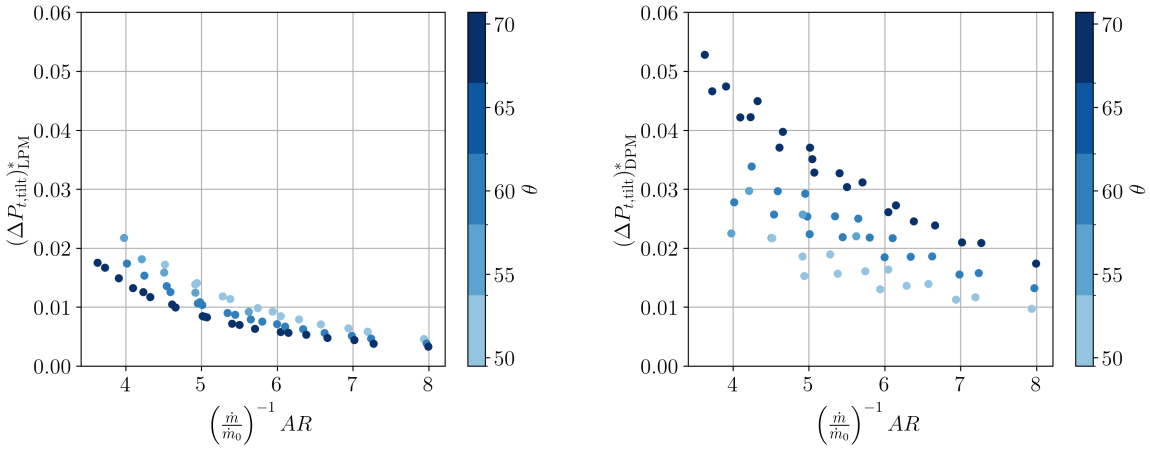

(a) LPM (b) DPM

Figure 13.14: Total pressure drop due to tilting the heat exchanger normalised with the freestream total pressure for the DPM and LPM as a function of the inverse of the mass flow rate ratio times the diffuser area ratio.

The trend of the DPM can be explained by using the results from Section 13.1. Here, it was shown that for an inclined inflow angle, the transversal velocity component is dissipated upon entry into the porous zone. Moreover, Figure 13.15 shows that the tilt total pressure drop is proportional to the dynamic pressure of the transversal velocity component scaled with the non-dimensional heat exchanger height $(\dot{m}/\dot{m}_0)^{-1} AR/(\cos(\theta))$ and depth over width ratio L_4/W_4.

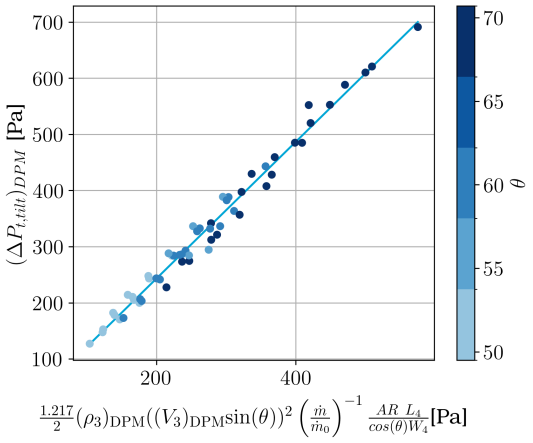

Figure 13.15: DPM tilt total pressure drop fitted to Equation 13.7

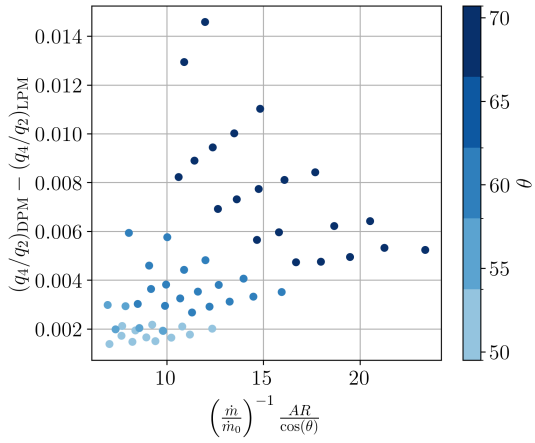

Figure 13.16: Difference in dynamic pressure at station 4, where the reported dynamic pressure is computed with the velocity inside of the heat exchanger.

The LPM trend can be explained by the fact that the extra pressure drop across the heat exchanger is a function of the non-inclined heat exchanger static pressure drop and the inclination angle. As with higher inclination angles, the modelled diffusion in the tilt increases, it decreases the velocity at the heat exchanger inlet. In turn, this reduces the pressure drop across the heat exchanger and, subsequently, the total pressure drop due to tilt.
The evolution of the static, total and dynamic pressure differences from the diffuser outlet to the heat exchanger inlet will be discussed next. Figure 13.12 shows that at the diffuser outlet, the static, total and dynamic pressure of the DPM is generally higher than the LPM. From the diffuser outlet to the heat exchanger inlet, the LPM has no total pressure losses and the static pressure increase is estimated according to Equation 13.6. Conversely, the DPM reports relatively small static pressure changes with larger total pressure drops. Here, the total pressure drop can be approximated with the Equation 13.7. Equations 13.6 and 13.7 therefore show that both models have a decreasing dynamic pressure with inclination angle while having opposite trends in static and total pressure. This implies that for some heat exchanger inclination angle θ, the LPM has generally higher static and total pressure at the heat exchanger inlet. Furthermore, as Equations 13.6 and 13.7 scale differently with $\sin(\theta)^2$ it is observed from Figure 13.16 that the dynamic pressure at the heat exchanger inlet aligns best for lower inclination angles (e.g. $\theta = 50$).

$$(\Delta P_s)_{\text{LPM}} = (V_3)^2_{\text{LPM}} - (\cos(\theta)(V_3)_{\text{LPM}})^2 = (\sin(\theta)(V_3)_{\text{LPM}})^2 \tag{13.6}$$

$$(\Delta P_t)_{\text{DPM}} = \frac{1.217}{2}(\rho_3)_{\text{DPM}}((V_3)_{\text{DPM}}\sin(\theta))^2\left(\frac{\dot{m}}{\dot{m}_0}\right)^{-1}\frac{AR\ \ L_4}{cos(\theta)W_4} \tag{13.7}$$

HEAT EXCHANGER

The overall differences in total pressure drop and total temperature increase across the heat exchanger between the models are shown in Figure 13.17. The mean absolute difference in total pressure drop is 1.01 % of the ingested free stream dynamic pressure, and the mean absolute difference in total temperature increase is 0.32% of the total temperature at the heat exchanger inlet. Similarly to the diffuser and tilt sections, the total pressure drop difference is highest for higher heat exchanger inclination angles. The difference in total temperature increase also grows with the heat exchanger inclination angle.

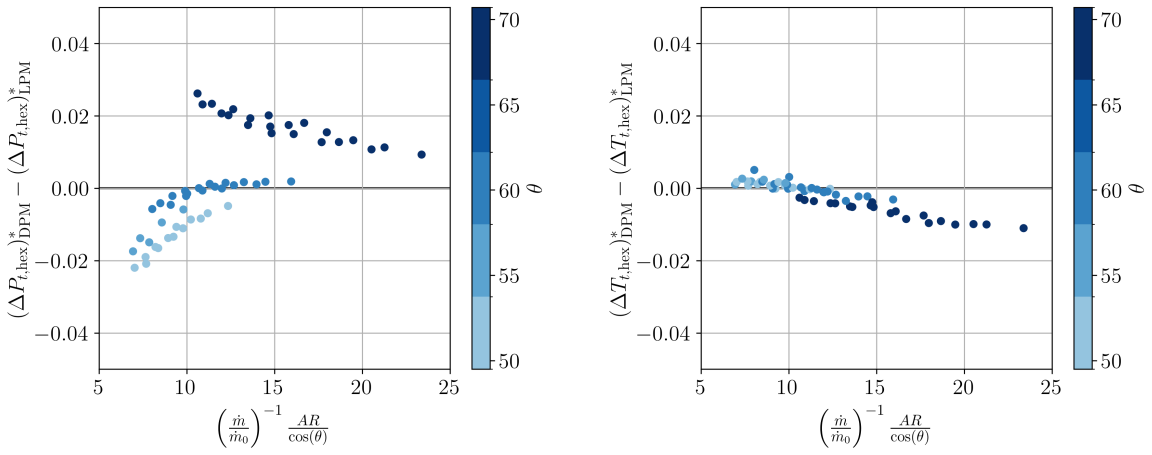

Figure 13.17: Total pressure drop and total temperature increase differences of the heat exchanger between the two models. Here the total pressure drop is normalized with the dynamic pressure of the ingested stream tube q_0 and the total temperature increase is normalized with the total temperature of the ingested stream tube $T_{t,0}$

It is established that at the heat exchanger inlet, the total and static pressures reported by the LPM are generally larger than those reported by the DPM, while the latter shows higher inlet dynamic pressures at the heat exchanger inlet. Conversely, the LPM still shows generally slightly higher static pressure drops for low inclination angles, as shown near the origin point of Figure 13.18.

From the verification study, it is expected that the DPM predicts static pressure drops that are ~ 5 % lower for similar inlet conditions. This is roughly true for low discrepancies in inlet velocity, shown with the black dashed line indicating a 5% offset in static pressure drop. For higher differences in inlet velocity, the difference surpasses the ~ 5 % offset.

To inspect this further, the black dots in Figure 13.18 show the static pressure drop computed with Equation 13.8. This equation uses the arithmetic mean values of the velocity, u and viscosity μ and the harmonic mean of the density ρ of the DPM data across the heat exchanger, together with the coefficients D_{ref} and F_{ref} of each datapoint.
From the black dots shown in Figure 13.18, it can be observed that the static pressure drop computed by Equation 13.8 is much higher than the reported static pressure drop by the LPM and DPM. This can be explained by the fact that the thermodynamic values reported by the DPM are lumped into a single value using a mass-weighted average. This method of averaging presumably overestimates the actual mean velocity in the porous zone and thereby overestimates the static pressure drop.
Furthermore, the black dots shown in Figure 13.18 show a different trend with respect to deviations in relative inlet velocity. This implies that the difference in inlet velocity is not the only reason for the difference in static pressure drop across the heat exchanger. Inspecting Figure 13.18(b) shows that the higher differences in static pressure drop correspond to lower mass-weighted uniformity indices of the velocity, $\gamma_{m,v}$. As shown in Equation 13.8, the pressure drop scales quadratically with the mean velocity in the porous zone and, therefore, more non-uniform inlet velocity profile can explain the trend in static pressure drop differences.
The non-uniform inlet velocity profile can also possibly explain the deviations in total temperature increase. As seen in Figure 13.18, low values of the mass-weighted uniformity indices of the velocity, $\gamma_{m,v}$, strongly correlate with the heat exchanger inclination angle. Therefore, the higher differences in total temperature increase shown in Figure 13.17 also correspond to more non-uniform inlet velocity profiles, where a non-uniform heat exchanger inlet velocity decreases the heat transfer rate as explained in Section 13.3.1.

$$\Delta P_s = L_4 \left(\mu_m D_{\text{ref}} u_m + \frac{1}{2} \rho_m F_{\text{ref}} u_m^2 \right) \tag{13.8}$$

$$\delta P_{s,\text{hex}} = \frac{(\Delta P_{s,\text{hex}})_{\text{DPM}} - (\Delta P_{s,\text{hex}})_{\text{LPM}}}{(\Delta P_{s,\text{hex}})_{\text{LPM}}} \tag{13.9}$$

$$\delta V_3 = \frac{(V_3)_{\text{DPM}} - (V_3)_{\text{LPM}}}{(V_3)_{\text{LPM}}} \tag{13.10}$$

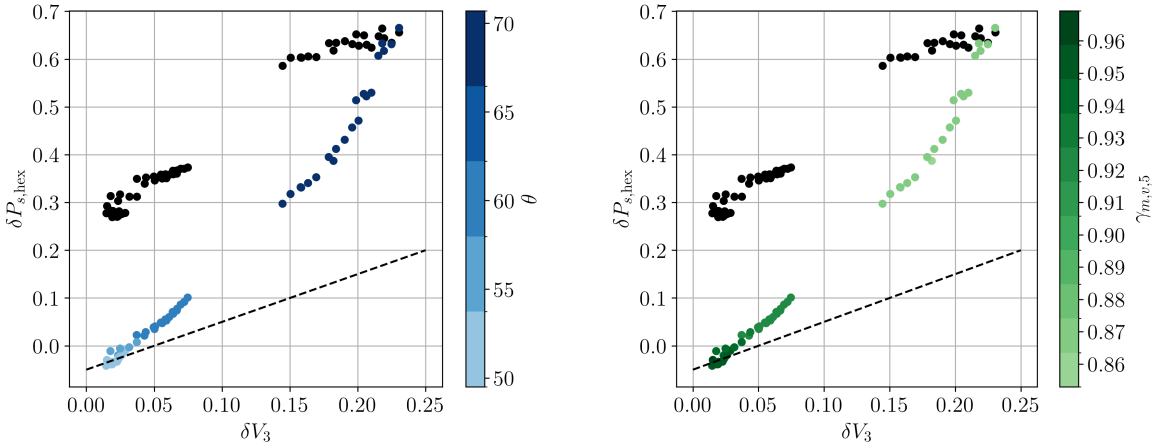

(a) (b)

Figure 13.18: Relative difference in heat exchanger inlet velocity, δV_3 as defined in Equation 13.10, versus the relative difference in static pressure drop, $\delta P_{s,\text{hex}}$ as defined in Equation 13.9. In this figure, the mass-weighted uniformity index, $\gamma_{m,v}$, as well as the inclination angle θ of each data point, are shown. The black dashed line indicates the predicted difference relation between heat exchanger inlet velocity and pressure drop from the verification study. The black dots in the figures indicate the static pressure drop computed with Equation 13.8 using the data of the DPM.

TILT BACK AND NOZZLE

From the outlet of the heat exchanger up to the ram air duct outlet, the models agree well on the total pressure loss as shown in Figure 13.19, where the differences decrease with increasing nozzle area ratio. The mean absolute difference between the models is 0.190 % of the ingested stream tube dynamic pressure.

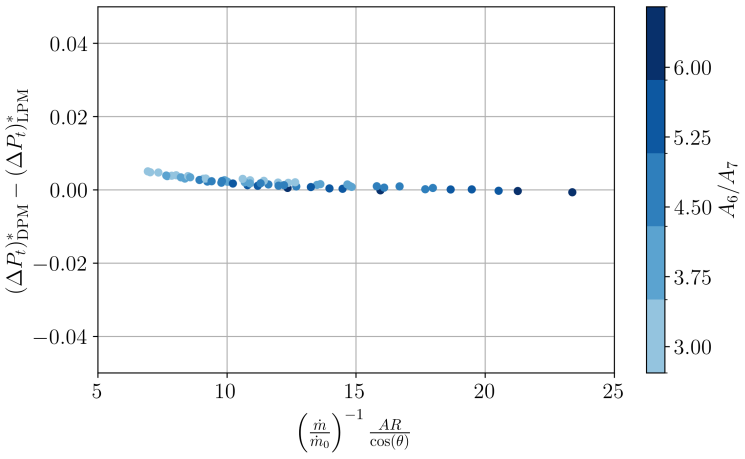

Figure 13.19: Difference in total pressure drop in tilt back and nozzle sections of the ram air duct divided by the dynamic pressure of the ingested stream tube, station 0.

OVERALL COMPARISON

In summary, the mean absolute difference in total pressure drop across the ram air duct amounts to 1.81 % of the ingested stream tube dynamic pressure. The mean absolute difference in total temperature increase amounts to 0.32 % of the total temperature of the ingested stream tube. The differences across the ram air duct are summarized in Figures 13.20 and 13.21.

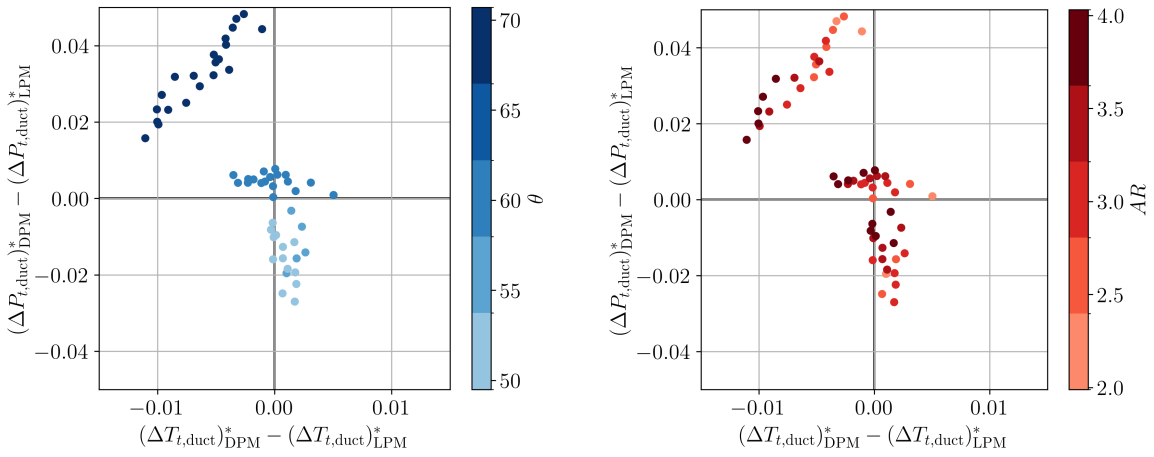

(a) (b)

Figure 13.20: Relative differences of total quantities across the ram air duct. In this figure, the pressure and temperature quantities are normalised with the dynamic pressure and total temperature of the ingested stream tube, respectively.

The diffuser and tilt show a maximum total pressure drop difference of ~ 2% of the ingested stream tube dynamic pressure with a mean absolute difference of 0.78% of the ingested stream tube dynamic pressure. Between the diffuser and tilt, the diffuser shows the largest differences in the total pressure drop estimation. Furthermore, it is shown that there is an interaction between the mass flow rate ratio, heat exchanger inclination angle and diffuser performance. Regarding the tilt model, the two models display opposing trends with

increasing inclination angles. This produces similar total pressure drops for low inclination angles ($\theta = 50$) but higher differences for higher inclination angles, θ. This difference fortuitously opposes the accumulated differences in total pressure drop across the diffuser and tilt and thereby also explains the small deviations in total pressure differences for $\theta = 60$.
The heat exchanger shows a maximum total pressure drop difference of ~ 2.3 % of the ingested stream tube dynamic pressure with a mean absolute difference of 1.01 % of the ingested stream tube dynamic pressure. The total temperature increase shows a maximum deviation of 0.05 % of the total temperature of the ingested stream tube with a mean absolute difference of 0.32 %. Larger differences between the two models are correlated to higher inclination angles and low values of the mass-weighted uniformity index $\gamma_{m,v}$. It was shown that for higher differences in heat exchanger inlet velocity, the difference in static pressure increased. Next to this, evidence was found that more non-uniform inlet velocity profiles also contribute to the increasing differences in static pressure drop. The tilt back and nozzle components contribute only to a relatively small amount of the overall total pressure drop differences.
Overall, Figures 13.20 and 13.21 show that the total pressure drop and differences in total pressure drop and total temperature increase across the ram air duct are smaller for inclination angles of $\theta = 60$ and that larger differences are associated with larger inclination angles. Furthermore, it is observed that the area ratio generally reduces the differences in total pressure drop while higher mass flow rate ratios have little effect on the differences total pressure drop and total temperature increase except for inclination angles of $\theta = 70$.

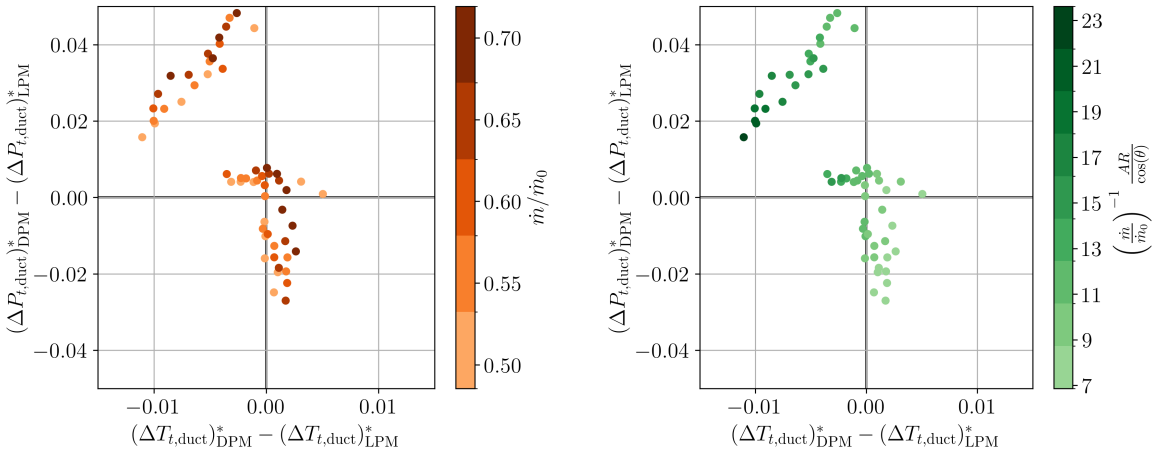

(a) (b)

Figure 13.21: Relative differences of total quantities across the ram air duct. In this figure, the pressure and temperature quantities are normalised with the dynamic pressure and total temperature of the ingested stream tube, respectively

13.4. CONCLUSION

The verification of the detailed physics model shows that there is a difference of ~ 5% in static pressure drop between the predictions of *HeXaCode* [63] and the calibrated porous zone. The grid convergence study showed that the total pressure drop across the ram air duct ΔP_t, the effective outlet area of the diffuser E_3, and the total temperature increase across the ram air duct ΔT_t were grid-independent for meshes larger than 1M elements. Ideally, however, when more computational power is available the used grid size should be finer such that the solution variables lie closer to their Richardson extrapolate.
The results of the detailed physics model showed that there is a good agreement in terms of drag recovery between the two models, showing that the lumped parameter model can be used to achieve similar results to a two-dimensional CFD with orders of magnitude lower computational costs. The main differences between the models originate from the diffuser and tilt models used in the LPM. More in detail, the total pressure loss estimated by the two models in the tilt section of the duct differs significantly, showing opposite trends with respect to the tilt angle. Next to this, it was found that the diffuser performance was affected by the mass flow rate ratio and inclination angle. Regarding the heat exchanger, it was found that the differences in total pressure drop and total temperature increase predicted by the two models originate from differences in heat exchanger inlet velocity and non-uniform velocity inlet profiles.

IV

Conclusion and Discussion

14

CONCLUSION & RECOMMENDATIONS

In this chapter, the conclusions of the results shown in chapters 11, 11 and 13 will be summarized, whereafter a discussion will be held elaborating on recommendations for future research.

14.1. CONCLUSION

In Chapter 11, the results of the longitudinal multipass condenser were discussed. Here, an optimization was performed to see if adding multiple passes with variable geometry can outperform a single-pass condenser with similar constant geometry in terms of pressure drop. From the results, it was concluded that the optimiser found an optimum in increasing the heat exchanger blockage factor and increasing the heat exchanger size without varying the geometry per pass. Naturally, this showed that for the considered thermodynamic conditions the multipass heat exchangers were not outperforming the single pass baseline condenser in terms of cold side pressure drop. On top of that, it was concluded that the hot side pressure drop increased significantly, as the same amount of working fluid now has to pass through less flow area.

In Chapter 12, the results of the lumped parameter model were discussed. Here, first, a sensitivity study was performed on the drag recovery factor and ram air duct length for varying duct geometrical parameters. It was concluded that the inclination angle was the most space-efficient way of increasing the drag recovery factor, while the diffuser area ratio has a similar effect but imposes a more significant penalty on the ram air duct length. Next to this, it was found that there is a range of mass flow rate ratios that have similar performance for a given diffuser area ratio and inclination angle. Finally, it was concluded that the fin height had a weaker effect on the drag recovery factor than the duct geometry parameters, yet the results show how its optimum value depends on the duct geometry parameters.

Next to this, in Chapter 12, an investigation into the preliminary optimal design of a ram air duct was performed. In this investigation ram air ducts featuring different heat exchanger types were optimized for varying maximum length constraints. It was found that among the investigated heat exchanger types, the inline plain tube bundle and the flat tube offset strip fin heat exchanger showed the highest drag recovery factors. Between the two types, the inline plain tube bundle showed a lower overall mass of the ram air duct. Furthermore, it was found that the two highest-performing heat exchanger types reached their unconstraint optimum ram air duct design in the least required space. To assess the effect of an ingested boundary layer, optimisations of the ram air duct were performed using a single heat exchanger type for varying diffuser-blocked area fractions. It was found that general guidelines can be proposed for the optimal duct design for diffuser-blocked area fractions of about $B > 0.02$. Namely, operating the duct at a mass flow rate ratio that offers maximum pre-diffusion without extra spillage drag, a maximum heat exchanger inclination angle and increasing the diffuser area ratio according to the maximum available space.

In Chapter 13, the results of the detailed physics model were discussed. Here, verification of the porous media modelling was performed by comparing the change of thermodynamic quantities across the porous zone with the predictions of *HeXaCode* [63]. This investigation showed mean deviations of $\sim 5\%$ for the static pressure $\sim 0.8\%$ for the static temperature and $\sim 0.4\%$ for the velocity. Hereafter, a grid convergence study was

performed to investigate if the main solution variables of the numerical simulation were grid-independent. This study showed for the chosen grid size asymptotic grid convergence indices of 1.002, 1.035 and 1.001 for the effective outlet area fraction E_3, the total pressure drop across the duct ΔP_t and total temperature increase across the duct ΔT_t, respectively.

Furthermore, in Chapter 13, a per-station comparison between the DPM and LPM was performed on the found optimal geometry from the constrained optimization. Here, it was found that both models agreed well on the drag recovery factor, while there were relatively large differences in diffuser total pressure drop and added total pressure drop due to inclining the heat exchanger and heat exchanger total pressure drop. Next to this, it was shown that the velocity showed to be relatively non-uniform while the static pressure, static temperature and density had close to uniform profiles.

Finally, in Chapter 13, a multiple design point comparison between the DPM and LPM was performed. Here, it was found that DPM and LPM are in good agreement in terms of drag recovery for a wide range of duct designs with a mean absolute difference of 1.081%. This shows that the lumped parameter model can be used to achieve similar net drag predictions of the ram air duct compared to a two-dimensional CFD with orders of magnitude lower computational costs. Furthermore, it was found that the diffuser and tilt components combined showed similar differences in total pressure drop between the models when compared to the heat exchanger total pressure drop differences. On top of that, it was found that the most significant deviations in total pressure drop across the ram air duct coincide with an inclination angle higher and lower than $\theta = 60$. This is explained by the fact that the pressure drop due to heat exchanger inclination showed opposing trends between the models. The trends of the tilt section oppose the accumulated differences in the diffuser, and therefore, differences are compensated for $\theta \simeq 60$. On top of that, the diffuser and tilt components were shown to produce a significant difference in heat exchanger inlet velocity, thereby increasing the difference in heat exchanger static pressure drop. Furthermore, it was found that the effect of a non-uniform inlet velocity profile added to the differences in static pressure drop. Moreover, the non-uniform inlet velocity profile is also suspected to affect the differences in total temperature increase. Finally the difference in the tilt back and nozzle sections of the duct were minimal.

It should be reiterated, however, that the drag recovery factor reported by the DPM and LPM is based on a correlation for the drag estimation, idealised duct geometry, and inlet local Mach number equal to the freestream value. In the real-world application, the drag will most likely be different from that estimated by the correlation: The duct will be less ideally shaped to comply with spacial constraints, and the interaction with the turboshaft and its inlet lip will most likely deviate the local Mach number form the freestream value.

Summarizing all findings, the main research question can be answered by keeping the aforementioned connotations in mind. The net drag impact of a condenser in a waste heat recovery system for the IMOTHEP DRAGON concept using the Meredith effect is a positive thrust, thereby not imposing a drag penalty by installing this ram air duct but increasing the overall thrust of the aircraft. This, in turn, revives Meredith's claim [2] from 1935 and answers research question 1.

14.2. RECOMENDATIONS

Although the results are able to provide numerous insights into the design of a ram air duct for a condenser, there are some limitations that need to be adressed.

First of all, it should be considered to validate the DPM results. In particular, validation of the upstream heating i.e. turbulent kinetic energy production in the diffuser, diffuser model at such high inlet aspect ratios, and the diffuser performance and the coupled effect of the inclination angle with the diffuser and heat exchanger. Understandably, a full system validation by experimental simulation can possibly not belong to the options available. Therefore, the next best thing would be to use higher fidelity computational fluid dynamics analysis to construct a general enough database of duct simulations for varying inlet aspect ratio, diffuser area ratio and inclination angle. With this, the porous media model 2D simulations can be validated, and the results can be used to develop a high-fidelity model for the diffuser-tilt-heat-exchanger region. It should be noted that the inlet total pressure/ambient conditions have been kept constant.

Next to this, it is a recommendation to consider the dynamics of the diffuser and heat exchanger inclination anlge together. This recommendation is based on the fact that the diffuser performance is affected by the inclination of the heat exchanger and mass flow rate ratio. On top of that, this recommendation is based on the fact that the most significant differences between the DPM and LPM accumulated in the diffuser and tilt sections and, in particular, the estimation of the extra added pressure drop due to inclining the heat exchanger.

Furthermore, it is recommended to include non-uniformities in the LPM heat exchanger model. This recommendation is based on the fact that when the diffuser is placed in front of a heat exchanger, the flow will not be uniform, and results have shown that it affects the pressure drop estimation.

In addition, it is recommended to investigate the effect of turning vanes before the heat exchanger on the drag recovery factor. This recommendation is based on the fact that the DPM showed little to no static pressure increase before the heat exchanger. Applying the turning vanes can possibly increase the static pressure increase before the heat exchanger. Next to this, turning vanes before the heat exchanger can possibly reduce to total pressure losses associated with inclining the heat exchanger by offering a more gradual change in flow direction.

Another recommendation is to include the external aerodynamics in the analysis. Currently, the drag component and local Mach number are obtained from a correlation modelling a dissimilar intake and assuming a local Mach number ratio of 1. External aerodynamics analysis can improve the predictions of the intake performance and its effect on the flow since the correlation used is generally applied to intakes with lower mass flow rates, different intake aspect ratios, and more protruding intakes (this latter point is better understood when looking at the difference in intake shape between Figures 8.1 and 8.4). Regarding the second point, the external aerodynamic analysis will improve the estimation of the local Mach number, and as seen in Figure 12.2, will arguably have a large effect on the drag recovery factor.

Furthermore, as noted in the conclusion presented in Section 14.1, it must be noted that the translation from the current simplified ram air duct geometry to a real-world application design can alter the performance of the ram air duct. The main challenges to tackle here are that the inlet will most likely need to be somewhat curved around the inlet lip of the turboshaft engine and that there are more nuanced space constraints, such as that the diffuser could possibly not diverge symmetrically. Including these effects is essential in the translation from this simplified test case to a real design.

V

APPENDIX

A

XDSM ARCHITECTURES

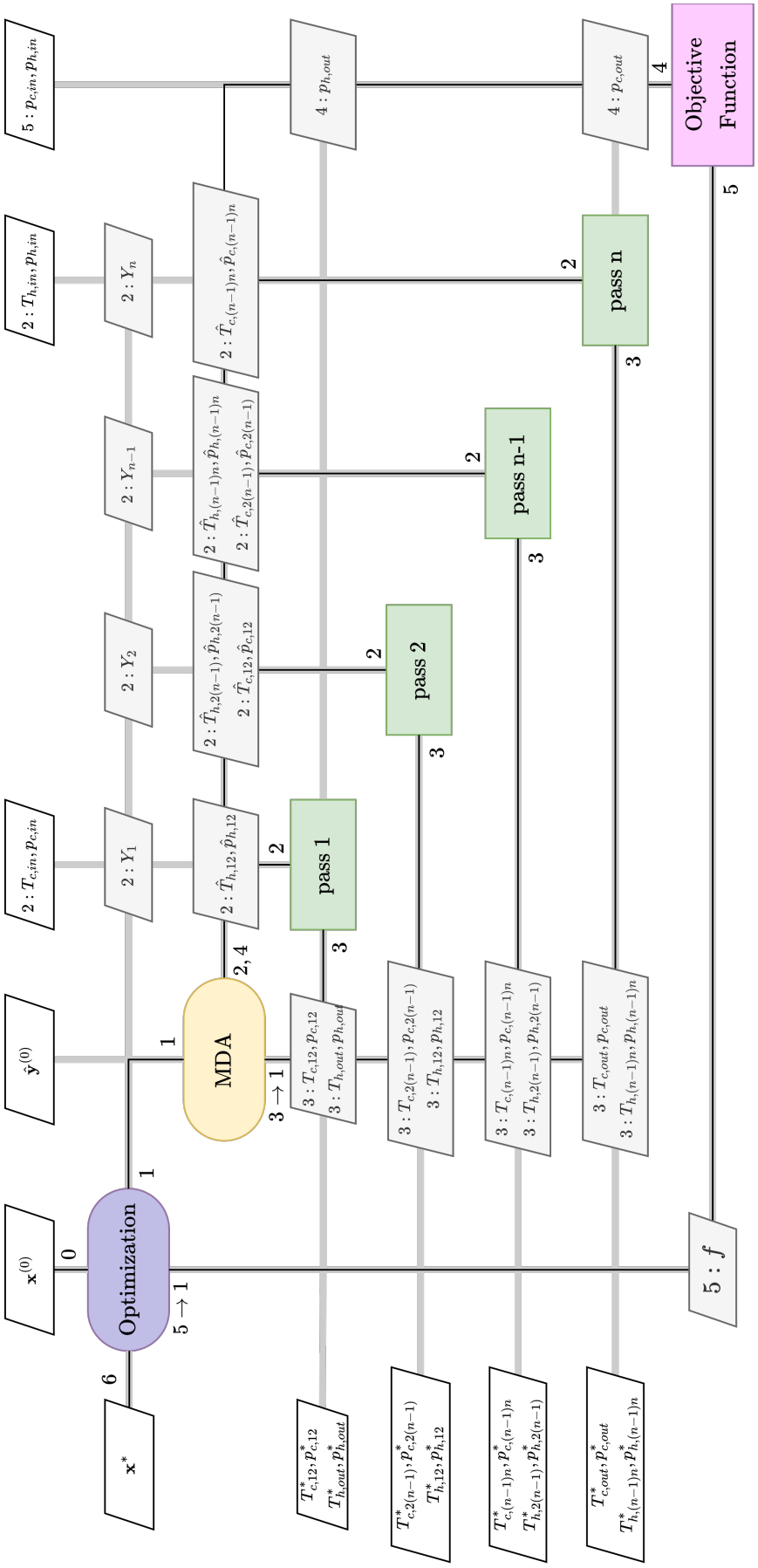

Figure A.1: MDF-Jacobi XDSM of longitudinal multi-pass heat exchanger

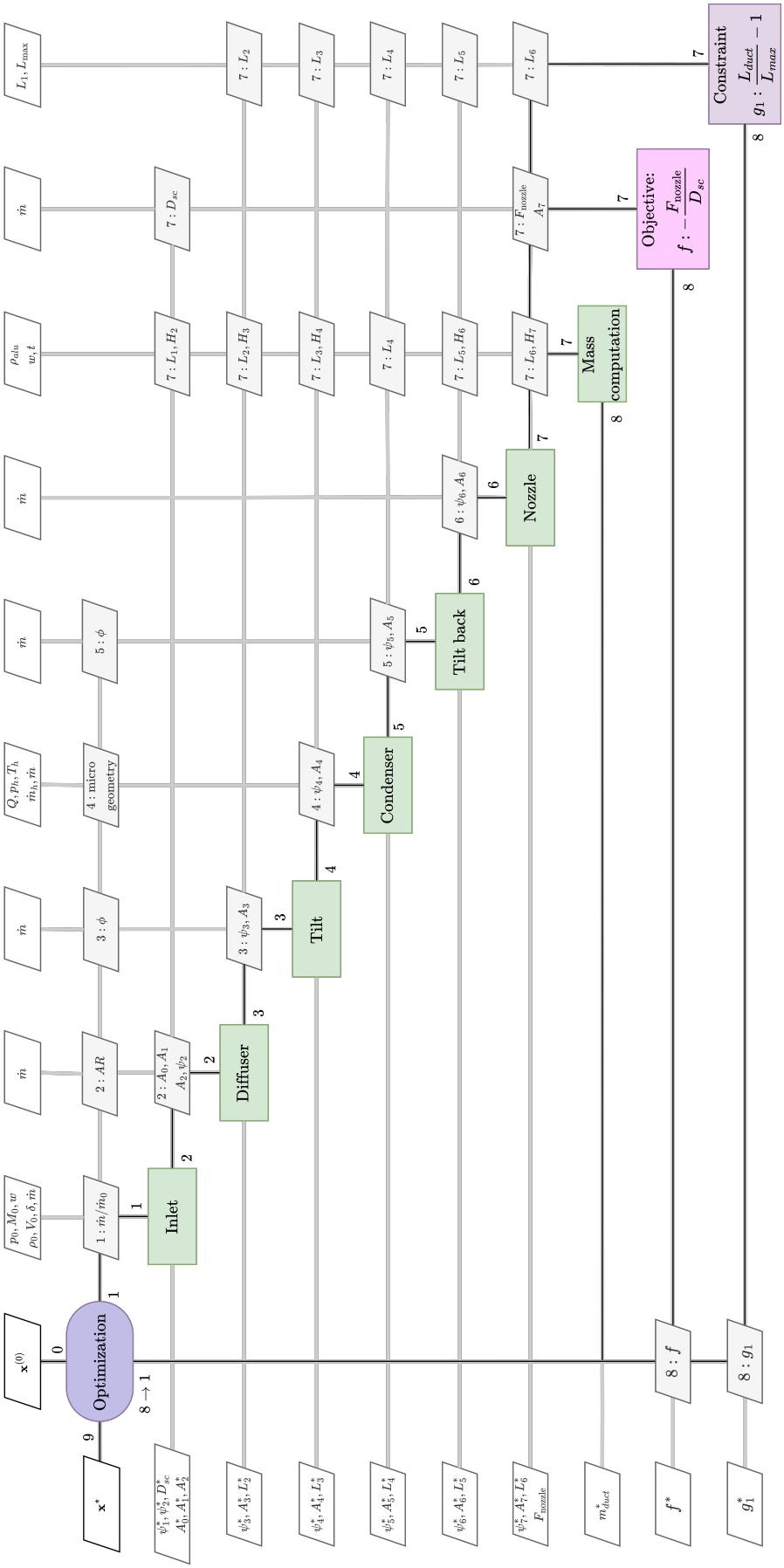

Figure A.2: MDF XDSM of lumped parameter model

B

CORRELATIONS & MODEL INPUTS

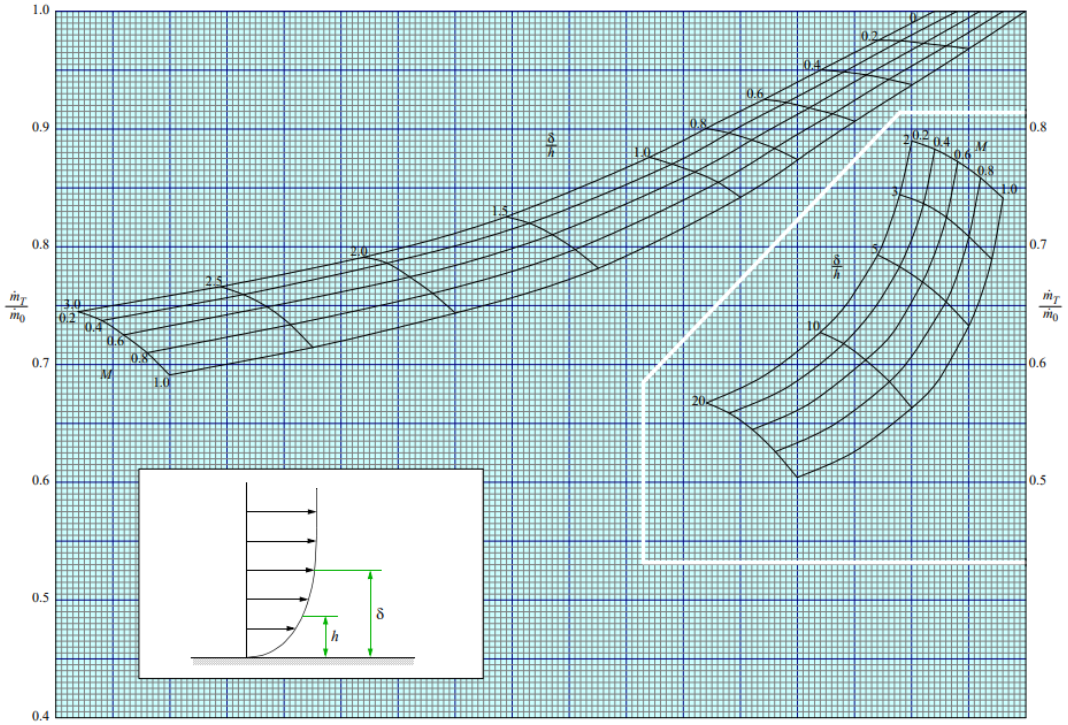

FIGURE 1 MASS FLOW RATIO

Figure B.1: Mass flow ratio, reproduced from [14]

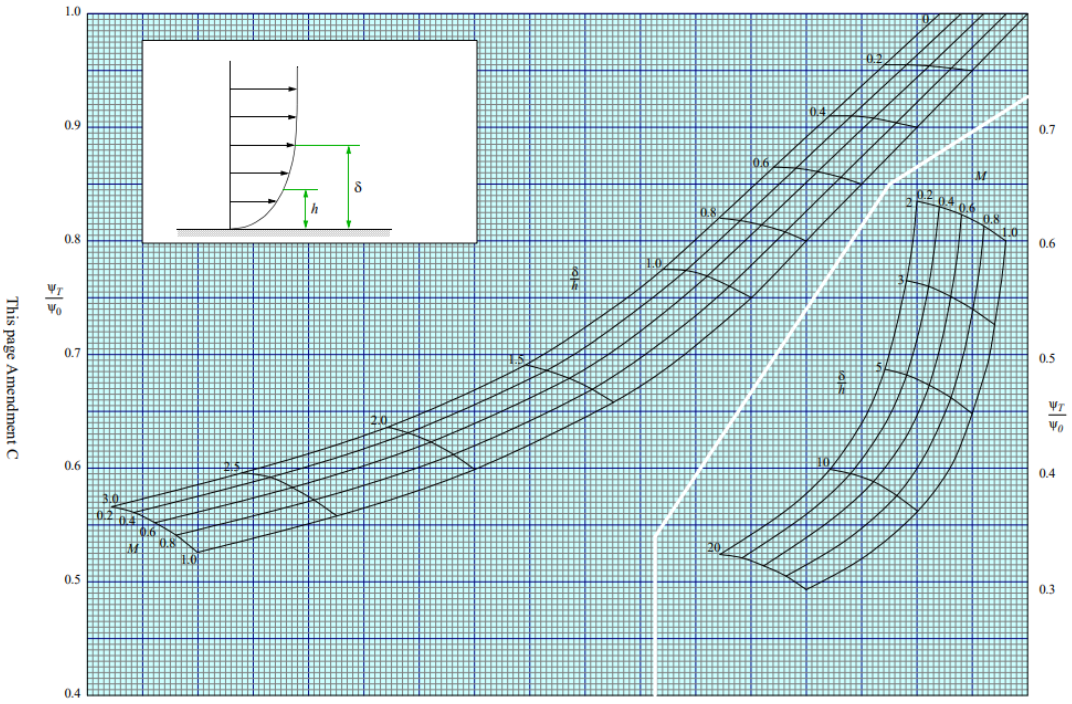

FIGURE 2 MOMENTUM FLOW RATIO

Figure B.2: Momentum flow ratio, reproduced from [14]

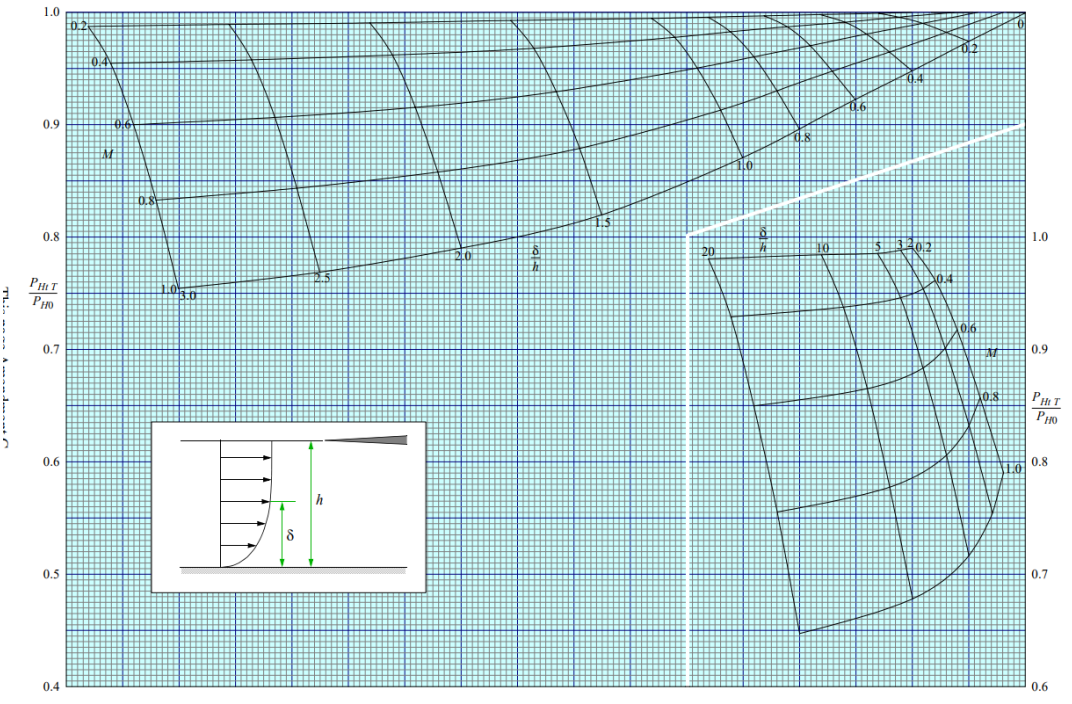

FIGURE 3 TOTAL PRESSURE RECOVERY

Figure B.3: Total pressure recovery, reproduced from [14]

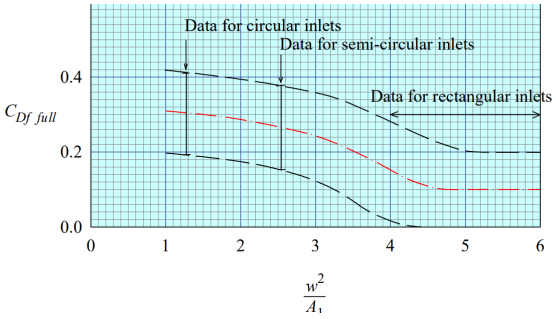

Figure B.4: Datum drag coefficient at full mass flow for scoop inlets, reproduced from [14]

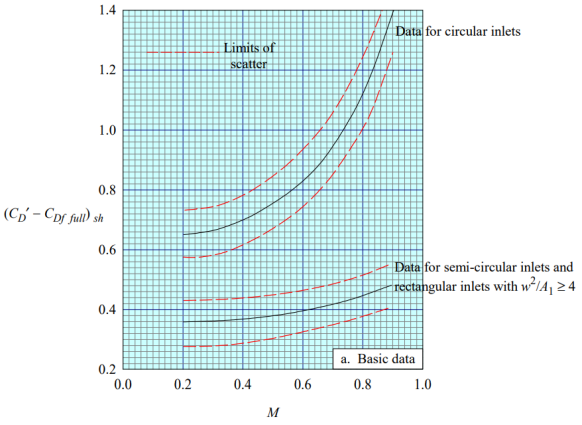

Figure B.5: Spillage drag at zero mass flow for sharp-lip scoop inlets, reproduced from [14]

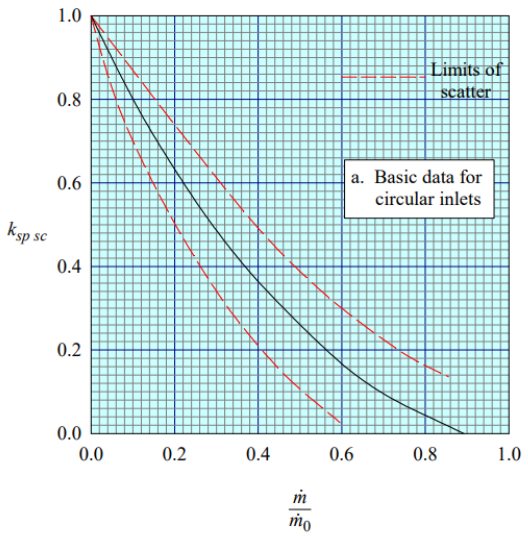

Figure B.6: Factor for spillage drag variation with mass flow ratio for circular scoop inlets, reproduced from [14]

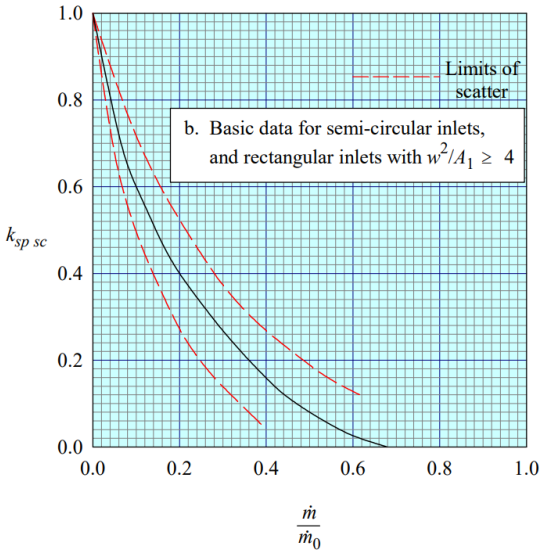

Figure B.7: Factor for spillage drag variation with mass flow ratio for semi-circular and rectangular scoop inlets, reproduced from [14]

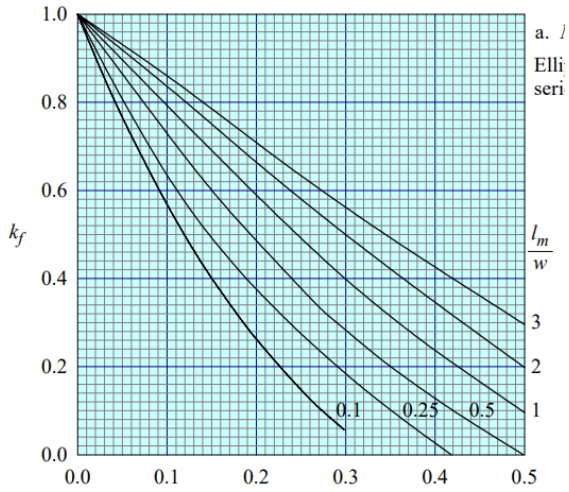

Figure B.8: Factor for the effect of the profile of the scoop fairing forebody on spillage drag, reproduced from [14]

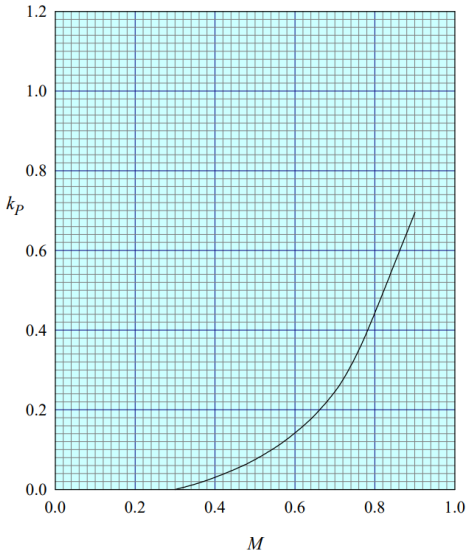

Figure B.9: Factor allowing for variation of $\Delta P_{Ht}/P_{H0}$ with mach number for scoop inlets, reproduced from [14]

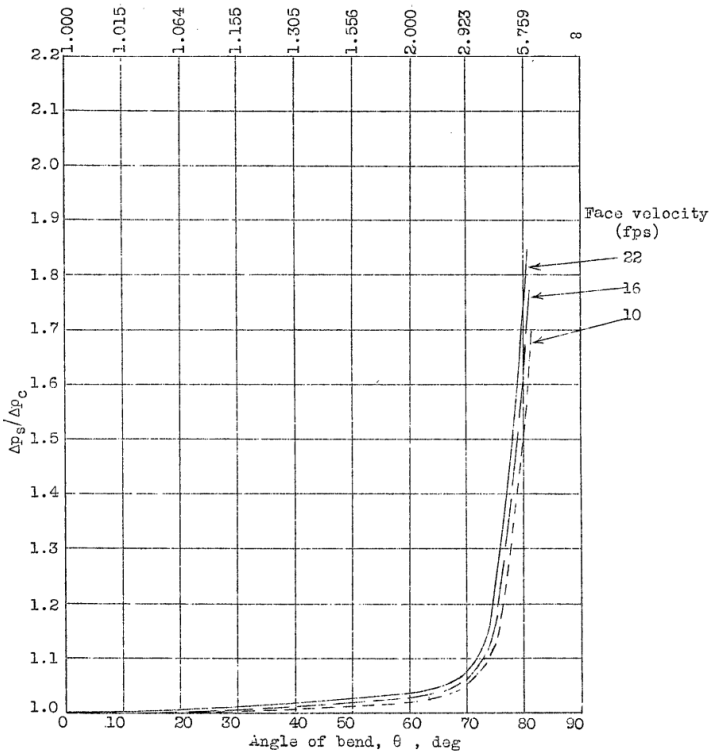

Figure B.10: Experimental data used for heat exchanger tilt model, reproduced from [19]

Micro geometry parameter	**FTOSF**	**FTLF**
Flow arrangement	*cross*	*cross*
Fin thickness	0.00018[m]	0.00018[m]
Microchannel wall thickness	0.0002[m]	0.0002[m]
Microchannel internal tube shape	*rectangle*	*rectangle*
Width of microchannel	0.00128[m]	0.00128[m]
Flat tube width	*variable*	*variable*
Flat tube height	0.002[m]	0.002[m]
Flat tube pitch stream wise	0.01[m]	0.01[m]
Fin height	*variable*	*variable*
Fin angle	-	0[deg]
Louver angle	-	29.6[deg]
Fin pitch	0.002[m]	0.0014322[m]
Louver pitch	-	0.001289[m]
Louver fin length	-	= 0.8*fin height*
Fin depth	0.004[m]	-
Micro geometry parameter	**PTBI**	**PTBS**
Flow arrangement	*cross*	*cross*
Internal tube shape	*circular*	*circular*
Major diameter tube	0.0018[m]	0.0018[m]
Transversal adimensional pitch	*variable*	*variable*
Longitudinal adimensional pitch	1.3[$-$]	= *transversal adimensional pitch*
Wall thickness tube	0.0002[m]	0.0002[m]
Tube arrangement	*inline*	*staggered*

Table B.1: Microgeometry specification of flat tube microchannel offset strip fin (FTOSF), flat tube microchannel louvered fin (FTLF), plain tube bundle inline (PTBI) and plain tube bundle staggered (PTBS) heat exchanger types.

DP	AR	θ	$\dot{m}/\dot{m}_0$	h_{fin}	DP	AR	θ	$\dot{m}/\dot{m}_0$	h_{fin}
DP0	3.8766	70	0.70	0.0129	DP45	2.51	70.00	0.60	0.012
DP1	2.01	55.00	0.50	0.012	DP46	3.00	50.00	0.60	0.012
DP2	2.01	60.00	0.50	0.012	DP47	3.00	55.00	0.60	0.012
DP3	2.01	65.00	0.50	0.012	DP48	3.00	60.00	0.60	0.012
DP4	2.01	70.00	0.50	0.012	DP49	3.00	65.00	0.60	0.012
DP5	2.51	50.00	0.50	0.012	DP50	3.00	70.00	0.60	0.012
DP6	2.51	55.00	0.50	0.012	DP51	3.50	50.00	0.60	0.012
DP7	2.51	60.00	0.50	0.012	DP52	3.50	55.00	0.60	0.012
DP8	2.51	65.00	0.50	0.012	DP53	3.50	60.00	0.60	0.012
DP9	2.51	70.00	0.50	0.012	DP54	3.50	65.00	0.60	0.012
DP10	3.00	50.00	0.50	0.012	DP55	3.50	70.00	0.60	0.012
DP11	3.00	55.00	0.50	0.012	DP56	3.99	50.00	0.60	0.012
DP12	3.00	60.00	0.50	0.012	DP57	3.99	55.00	0.60	0.012
DP13	3.00	65.00	0.50	0.012	DP58	3.99	60.00	0.60	0.012
DP14	3.00	70.00	0.50	0.012	DP59	3.99	65.00	0.60	0.012
DP15	3.50	50.00	0.50	0.012	DP60	3.99	70.00	0.60	0.012
DP16	3.50	55.00	0.50	0.012	DP61	2.51	70.00	0.65	0.012
DP17	3.50	60.00	0.50	0.012	DP62	3.00	50.00	0.65	0.012
DP18	3.50	65.00	0.50	0.012	DP63	3.00	55.00	0.65	0.012
DP19	3.50	70.00	0.50	0.012	DP64	3.00	60.00	0.65	0.012
DP20	3.99	50.00	0.50	0.012	DP65	3.00	65.00	0.65	0.012
DP21	3.99	55.00	0.50	0.012	DP66	3.00	70.00	0.65	0.012
DP22	3.99	60.00	0.50	0.012	DP67	3.50	50.00	0.65	0.012
DP23	3.99	65.00	0.50	0.012	DP68	3.50	55.00	0.65	0.012
DP24	3.99	70.00	0.50	0.012	DP69	3.50	60.00	0.65	0.012
DP25	2.01	70.00	0.55	0.012	DP70	3.50	65.00	0.65	0.012
DP26	2.51	55.00	0.55	0.012	DP71	3.50	70.00	0.65	0.012
DP27	2.51	60.00	0.55	0.012	DP72	3.99	50.00	0.65	0.012
DP28	2.51	65.00	0.55	0.012	DP73	3.99	55.00	0.65	0.012
DP29	2.51	70.00	0.55	0.012	DP74	3.99	60.00	0.65	0.012
DP30	3.00	50.00	0.55	0.012	DP75	3.99	65.00	0.65	0.012
DP31	3.00	55.00	0.55	0.012	DP76	3.99	70.00	0.65	0.012
DP32	3.00	60.00	0.55	0.012	DP77	2.51	70.00	0.70	0.012
DP33	3.00	65.00	0.55	0.012	DP78	3.00	55.00	0.70	0.012
DP34	3.00	70.00	0.55	0.012	DP79	3.00	60.00	0.70	0.012
DP35	3.50	50.00	0.55	0.012	DP80	3.00	65.00	0.70	0.012
DP36	3.50	55.00	0.55	0.012	DP81	3.00	70.00	0.70	0.012
DP37	3.50	60.00	0.55	0.012	DP82	3.50	55.00	0.70	0.012
DP38	3.50	65.00	0.55	0.012	DP83	3.50	60.00	0.70	0.012
DP39	3.50	70.00	0.55	0.012	DP84	3.50	65.00	0.70	0.012
DP40	3.99	50.00	0.55	0.012	DP85	3.50	70.00	0.70	0.012
DP41	3.99	55.00	0.55	0.012	DP86	3.99	55.00	0.70	0.012
DP42	3.99	60.00	0.55	0.012	DP87	3.99	60.00	0.70	0.012
DP43	3.99	65.00	0.55	0.012	DP88	3.99	65.00	0.70	0.012
DP44	3.99	70.00	0.55	0.012	DP89	3.99	70.00	0.70	0.012

Table B.2: Geometrical specification of design points.

C

SENSITIVITY DATA OF ALL HEAT EXCHANGER TYPES CONSIDERED

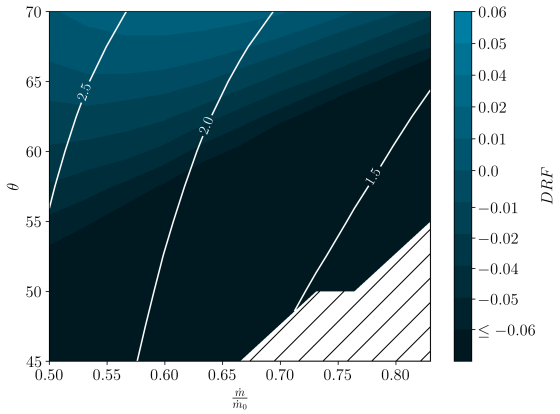

(a) Sensitivity to the inclination angle θ and mass flow rate ratio $\dot{m}/\dot{m}_0$.

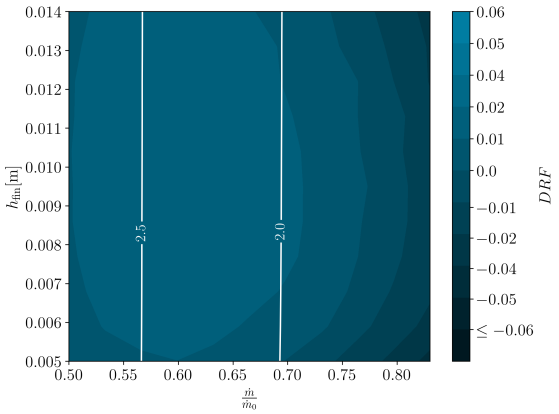

(b) Sensitivity to the fin height h_{fin} and mass flow rate ratio $\dot{m}/\dot{m}_0$.

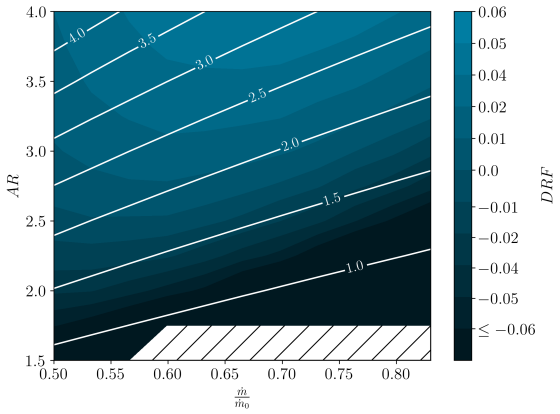

(c) Sensitivity to the diffuser area ratio AR and mass flow rate ratio $\dot{m}/\dot{m}_0$.

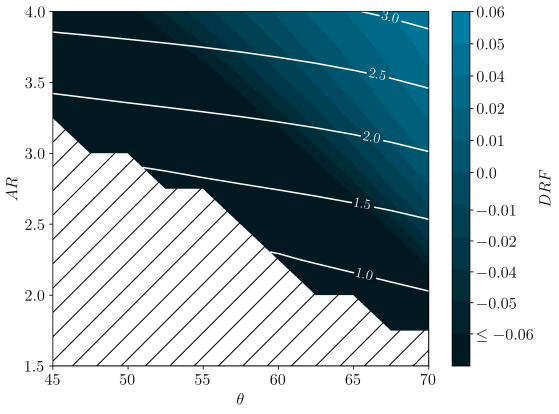

(d) Sensitivity to the diffuser area ratio AR and inclination angle θ.

Figure C.1: Drag Recovery Factor, Equation 8.1, sensitivity w.r.t the geometrical input variables for the flat tube louvred fin heat exchanger type. The white contour lines represent the duct length in meters.. The ranges used for the parameter sweep are shown in Table 8.2 as well as the constant values used to slice the multivariable design space.

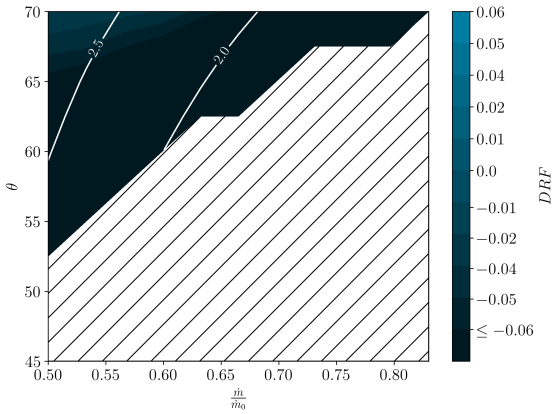

(a) Sensitivity to the inclination angle θ and mass flow rate ratio $\dot{m}/\dot{m}_0$.

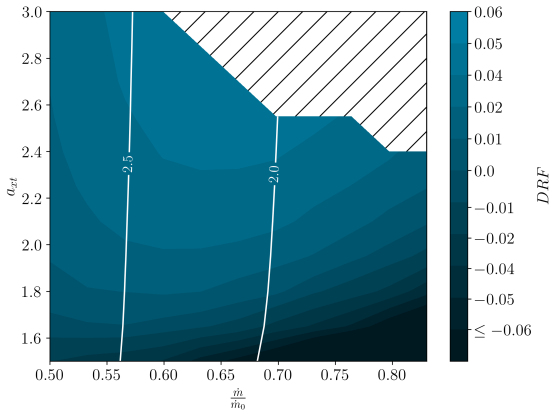

(b) Sensitivity to the fin height a_{xt} and mass flow rate ratio $\dot{m}/\dot{m}_0$.

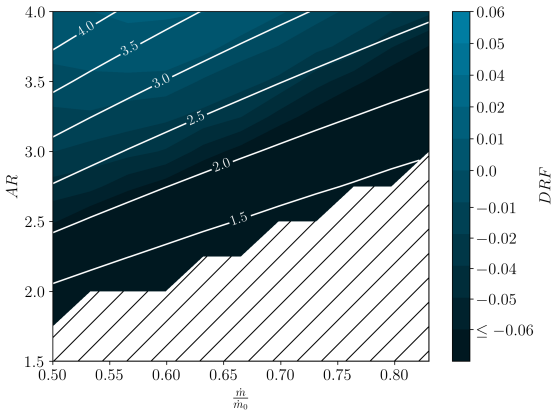

(c) Sensitivity to the diffuser area ratio AR and mass flow rate ratio $\dot{m}/\dot{m}_0$.

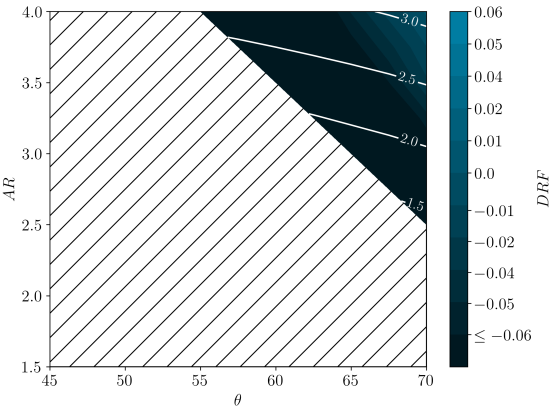

(d) Sensitivity to the diffuser area ratio AR and inclination angle θ.

Figure C.2: Drag Recovery Factor, Equation 8.1, sensitivity w.r.t the geometrical input variables for the inline plain tube bundle heat exchanger type. The white contour lines represent the duct length in meters.. The ranges used for the parameter sweep are shown in Table 8.2 as well as the constant values used to slice the multivariable design space.

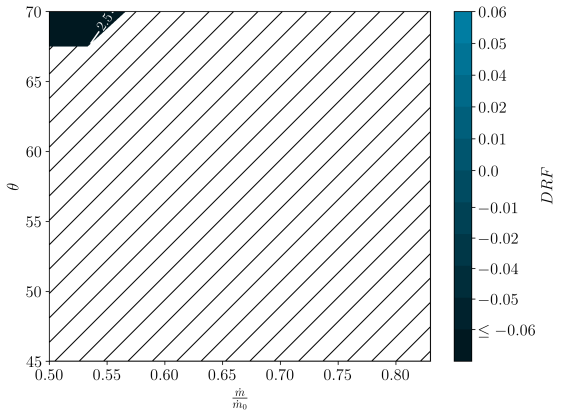

(a) Sensitivity to the inclination angle θ and mass flow rate ratio $\dot{m}/\dot{m}_0$.

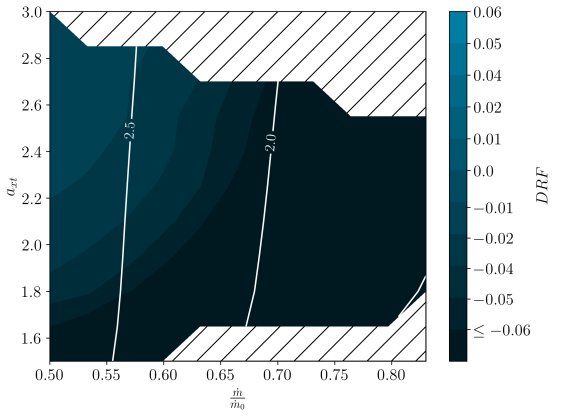

(b) Sensitivity to the fin height a_{xt} and mass flow rate ratio $\dot{m}/\dot{m}_0$.

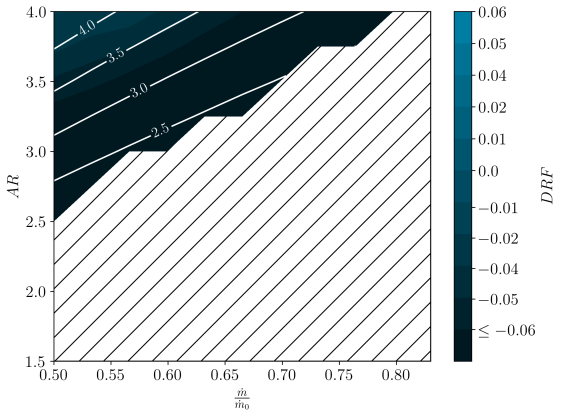

(c) Sensitivity to the diffuser area ratio AR and mass flow rate ratio $\dot{m}/\dot{m}_0$.

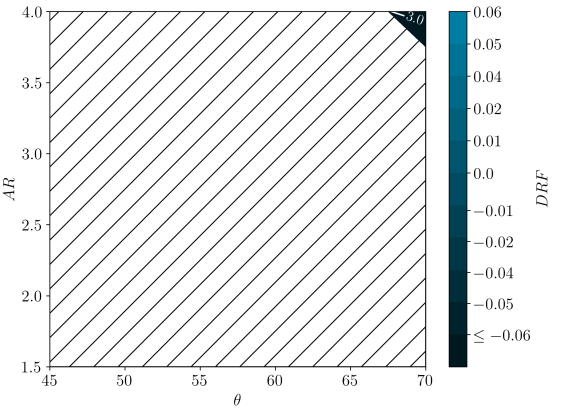

(d) Sensitivity to the diffuser area ratio AR and inclination angle θ.

Figure C.3: Drag Recovery Factor, Equation 8.1, sensitivity w.r.t the geometrical input variables for the staggered plain tube bundle heat exchanger type. The white contour lines represent the duct length in meters.. The ranges used for the parameter sweep are shown in Table 8.2 as well as the constant values used to slice the multivariable design space.

D

VERIFICATION DATA

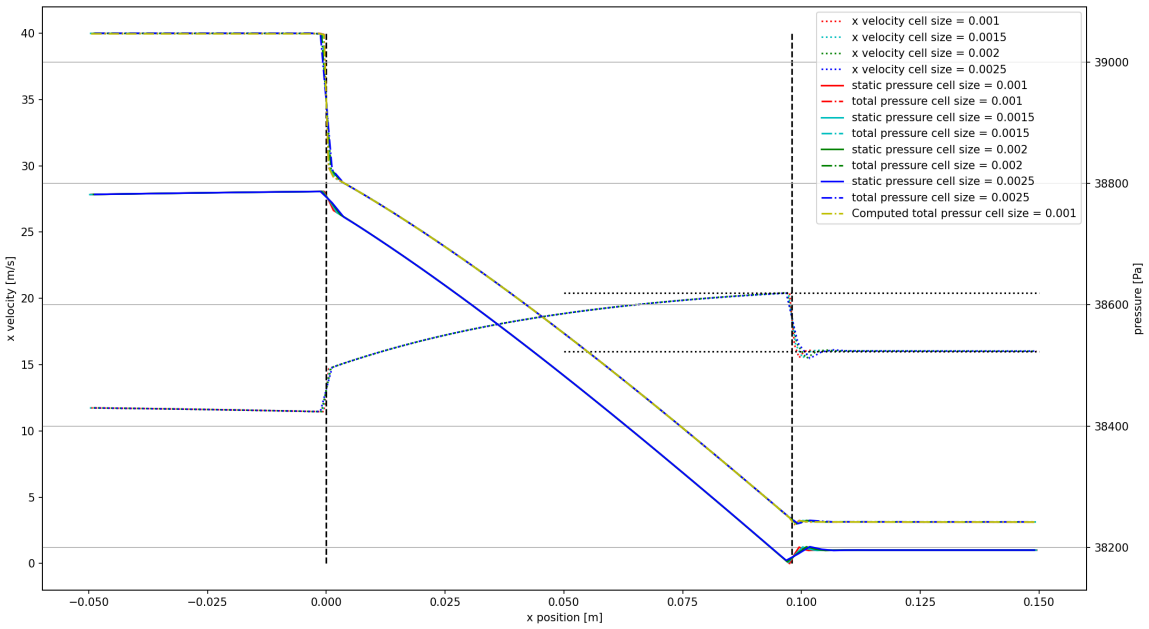

Figure D.1: Profile plot of straight duct test case for multiple grid sizes

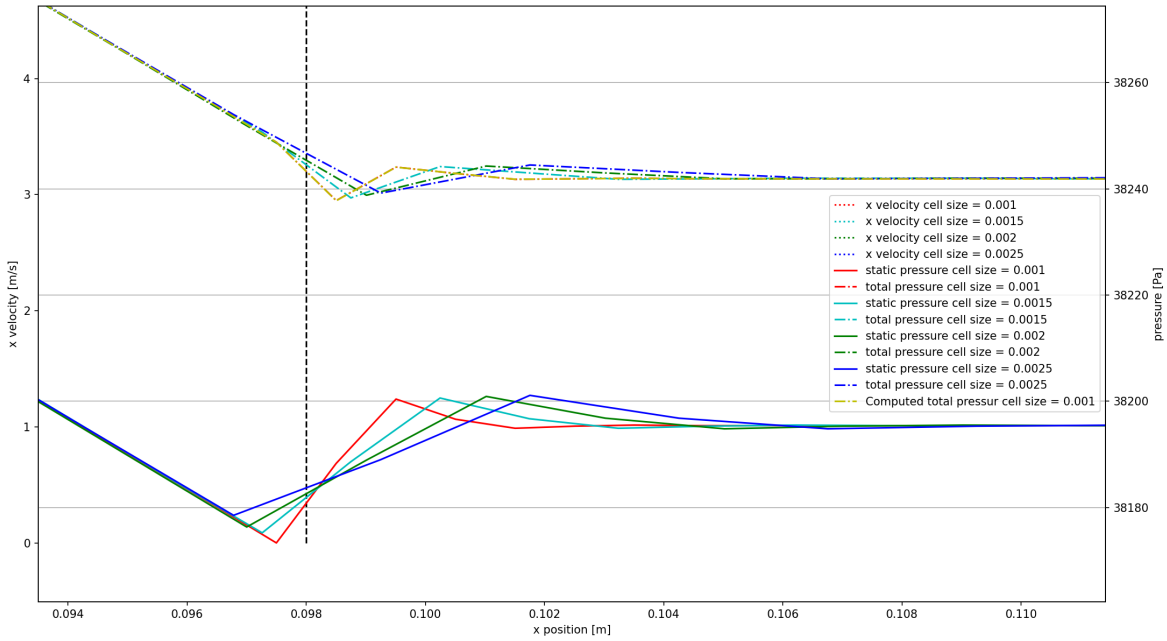

Figure D.2: Profile plot of straight duct test case for multiple grid sizes zoomed in on pressure oscillations

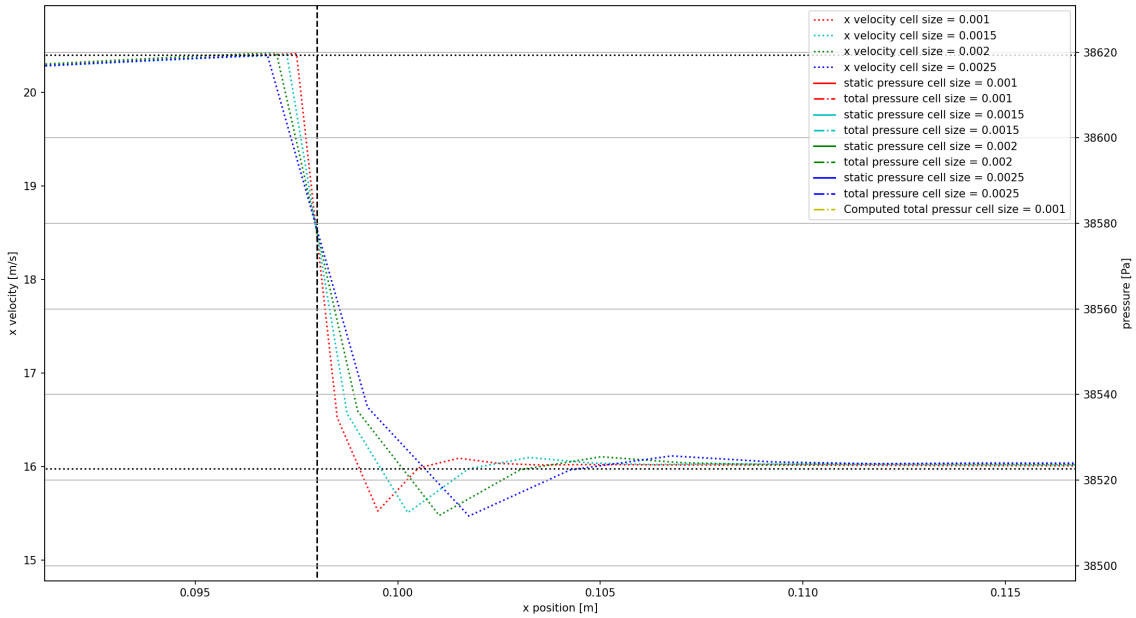

Figure D.3: Profile plot of straight duct test case for multiple grid sizes zoomed in on velocity oscillations

	ΔP_t	N_{cells}	r	GCI	$GCI_{\text{asymptotic}}$	p	$\Delta P_{t,\text{extrapolated}}$
Grid 2	1.577e+03	2009678	1.3	4.50%			
Grid 4	1.55e+03	1142241	1.6	6.02%	0.966	1.15	1.63e+03
Grid 6	1.50e+03	454358	-	-			
Grid 4	1.555e+03	1142241	1.6	6.35%			
Grid 6	1.50e+03	454358	1.5	10.93%	1.035	1.11	1.63e+03
Grid 8	1.43e+03	201302	-	-			
Grid 6	1.503e+03	454358	1.5	9.54%			
Grid 8	1.43e+03	201302	1.5	16.57%	1.052	1.23	1.62e+03
Grid 10	1.30e+03	88931	-	-			
	ΔP_t	N_{cells}	r	GCI	$GCI_{\text{asymptotic}}$	p	$\Delta P_{t,\text{extrapolated}}$
Grid 1	1.586e+03	2682439	1.3	4.74%			
Grid 3	1.57e+03	1567523	1.4	6.15%	0.997	0.98	1.65e+03
Grid 5	1.53e+03	752811	-	-			
Grid 3	1.568e+03	1567523	1.4	6.28%			
Grid 5	1.53e+03	752811	1.6	9.09%	1.016	0.97	1.65e+03
Grid 7	1.48e+03	311985	-	-			
Grid 5	1.534e+03	752811	1.6	7.01%			
Grid 7	1.48e+03	311985	1.5	12.31%	1.040	1.19	1.62e+03
Grid 9	1.38e+03	131956	-	-			
Grid 7	1.475e+03	311985	1.5	11.11%			
Grid 9	1.38e+03	131956	1.5	20.68%	1.070	1.29	1.61e+03
Grid 11	1.23e+03	59930	-	-			

Table D.1: Grid convergence study over 11 grids. ΔP_t represents the total pressure difference between the inlet and outlet and $\Delta P_{t,\text{extrapolated}}$ its extrapolated value. N_{cells} is the number of grid elements, r the refinement ration between two successive grids. GCI is the grid convergence index in percent and its asymptotic value is provided by $GCI_{\text{asymptotic}}$, where a value close to unity indicates a grid independent solution. The order achieved in the simulation is given by p.

	ΔT_t	N_{cells}	r	GCI	$GCI_{\text{asymptotic}}$	p	$\Delta T_{t,\text{extrapolated}}$
Grid 2	-1.003e+02	2009678	1.3	0.05%			
Grid 4	-1.00e+02	1142241	1.6	0.08%	0.971	1.53	-1.00e+02
Grid 6	-1.00e+02	454358	-	-			
Grid 4	-1.003e+02	1142241	1.6	0.07%			
Grid 6	-1.00e+02	454358	1.5	0.15%	1.001	1.63	-1.00e+02
Grid 8	-1.00e+02	201302	-	-			
Grid 6	-1.002e+02	454358	1.5	0.06%			
Grid 8	-1.00e+02	201302	1.5	0.21%	1.001	2.92	-1.00e+02
Grid 10	-9.97e+01	88931	-	-			

	ΔT_t	N_{cells}	r	GCI	$GCI_{\text{asymptotic}}$	p	$\Delta T_{t,\text{extrapolated}}$
Grid 1	-1.003e+02	2682439	1.3	1.45%			
Grid 3	-1.00e+02	1567523	1.4	1.48%	0.998	0.08	-1.01e+02
Grid 5	-1.00e+02	752811	-	-			
Grid 3	-1.003e+02	1567523	1.4	0.05%			
Grid 5	-1.00e+02	752811	1.6	0.10%	0.998	1.65	-1.00e+02
Grid 7	-1.00e+02	311985	-	-			
Grid 5	-1.003e+02	752811	1.6	0.04%			
Grid 7	-1.00e+02	311985	1.5	0.15%	1.001	2.68	-1.00e+02
Grid 9	-9.99e+01	131956	-	-			
Grid 7	-1.002e+02	311985	1.5	0.29%			
Grid 9	-9.99e+01	131956	1.5	0.60%	1.003	1.74	-1.00e+02
Grid 11	-9.94e+01	59930	-	-			

Table D.2: Grid convergence study over 11 grids. ΔT_t represents the total temperature difference between inlet and outlet and $\Delta T_{t,\text{extrapolated}}$ its extrapolated value. N_{cells} is the number of grid elements, r the refinement ration between two successive grids. GCI is the grid convergence index in percent and its asymptotic value is provided by $GCI_{\text{asymptotic}}$, where a value close to unity indicates a grid-independent solution. The order achieved in the simulation is given by p.

	E_3	N_{cells}	r	GCI	$GCI_{\text{asymptotic}}$	p	$E_{3,\text{extrapolated}}$
Grid 2	6.885e-01	2009678	1.3	0.00%			
Grid 4	6.89e-01	1142241	1.6	0.00%	0.000	33.20	6.89e-01
Grid 6	6.89e-01	454358	-	-			
Grid 4	6.887e-01	1142241	1.6	0.00%			
Grid 6	6.89e-01	454358	1.5	0.00%	1.002	14.43	6.89e-01
Grid 8	6.87e-01	201302	-	-			
Grid 6	6.887e-01	454358	1.5	0.22%			
Grid 8	6.87e-01	201302	1.5	0.60%	1.003	2.43	6.90e-01
Grid 10	6.81e-01	88931	-	-			

	E_3	N_{cells}	r	GCI	$GCI_{\text{asymptotic}}$	p	$E_{3,\text{extrapolated}}$
Grid 1	6.885e-01	2682439	1.3	0.94%			
Grid 3	6.89e-01	1567523	1.4	0.91%	0.945	0.11	6.83e-01
Grid 5	6.89e-01	752811	-	-			
Grid 3	6.886e-01	1567523	1.4	0.02%			
Grid 5	6.89e-01	752811	1.6	0.05%	0.909	2.55	6.88e-01
Grid 7	6.88e-01	311985	-	-			
Grid 5	6.888e-01	752811	1.6	0.02%			
Grid 7	6.88e-01	311985	1.5	0.13%	1.001	4.16	6.89e-01
Grid 9	6.85e-01	131956	-	-			
Grid 7	6.882e-01	311985	1.5	0.23%			
Grid 9	6.85e-01	131956	1.5	0.89%	1.005	3.19	6.89e-01
Grid 11	6.72e-01	59930	-	-			

Table D.3: Grid convergence study over 11 grids. E_3 represents the effective area fraction at the outlet of the diffuser and $E_{3,\text{extrapolated}}$ its extrapolated value. N_{cells} is the number of grid elements, r the refinement ration between two successive grids. GCI is the grid convergence index in percent and its asymptotic value is provided by $GCI_{\text{asymptotic}}$, where a value close to unity indicates a grid-independent solution. The order achieved in the simulation is given by p.

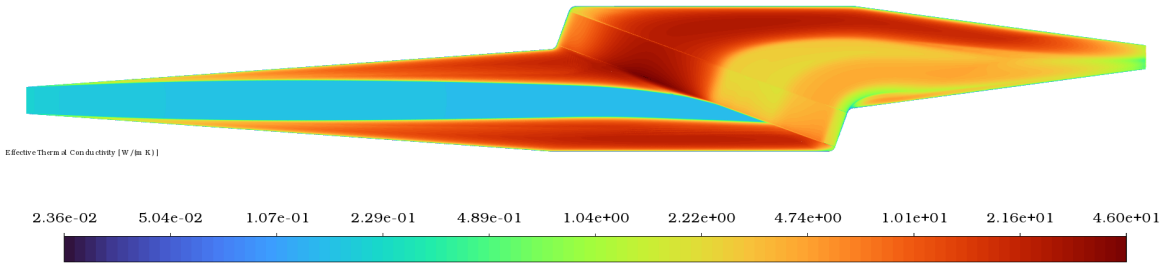

Figure D.4: Effective thermal conductivity contour of DP0

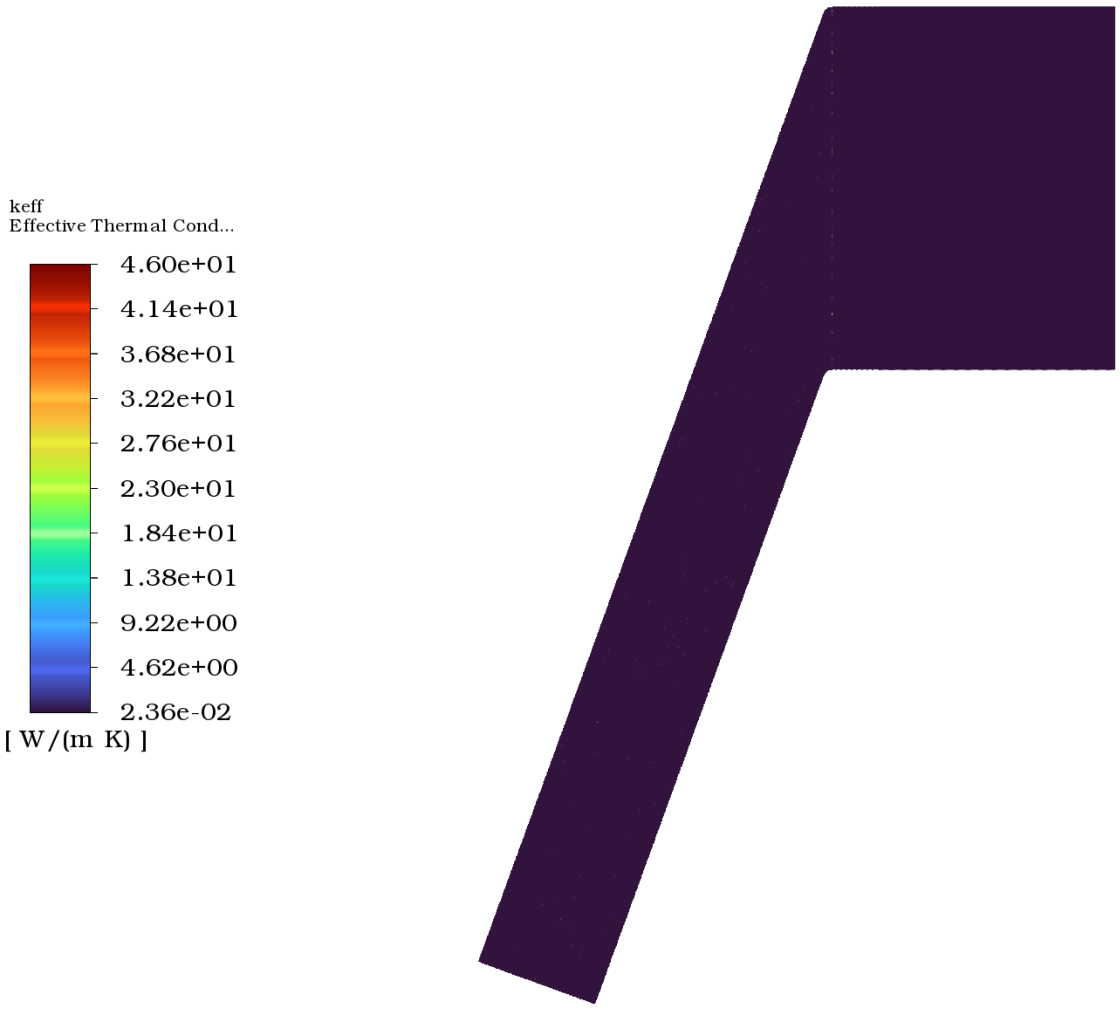

Figure D.5: Effective thermal conductivity contour of the inclined straight duct test case using the same colour scale ranges as Figure D.4

BIBLIOGRAPHY

[1] A. R. Khan, *P-51d mustangs of the 52nd fighter group,* World War II Pictures in Details (2022), from National Archives and Records Administration, 342-C-K-2741.

[2] F. W. Meredith, *Cooling of aircraft engines with special reference to ethylene glycol radiators enclosed in ducts*, Tech. Rep. (Aeronautical Research Committee, 1935).

[3] E. Commission, D.-G. for Mobility, Transport, D.-G. for Research, and Innovation, *Flightpath 2050 – Europe's vision for aviation – Maintaining global leadership and serving society's needs* (Publications Office, 2011).

[4] KCORC, *Airborne energy harvesting for aircraft,* (2020).

[5] H. Kellermann, M. Lüdemann, M. Pohl, and M. Hornung, *Design and optimization of ram air-based thermal management systems for hybrid-electric aircraft,* Aerospace **8** (2021).

[6] G. Warwick, *Onera dragon, airliner concepts: A step change in efficiency,* Aviation Week Network (2019), photo credit Onera.

[7] R. K. Shah and D. P. Sekulik, *Fundamentals of Heat Exchanger Design* (John Wiley & Sons inc., 2003).

[8] Z. Chu and W. Zhang, *Moving-boundary and finite volume coupling algorithm for heat exchanger with fluid phase change,* International Journal of Heat and Mass Transfer **131**, 313 (2019).

[9] M. Quintard, *Introduction to Heat and Mass Transport in Porous Media*, Tech. Rep. (North Atlantic Treaty Organization & Sience and Technology Organization, 2016).

[10] D. Missirlis, S. Donnerhack, O. Seite, C. Albanakis, A. Sideridis, K. Yakinthos, and A. Goulas, *Numerical development of heat transfer and pressure drop porosity model for a heat exchanger for aero engine applications,* Applied Thermal Engineering **30**, 1341 (2010).

[11] D. Bhakta, *Environmental control system inlet boeing 787-9 dreamliner,* Air Team Images Blog (2020).

[12] A. H. Sacks and R. S. Spreiter, *Theoretical Investigation of Submerged Inlets at Low Speeds*, Tech. Rep. (National Advisory Committee for Aeronautics, 1951).

[13] L. Henriksson, E. Dahl, P. Gullberg, and L. Löfdahl, *Experimental investigation of heat transfer rates and pressure drops through compact heat exchangers-where the heat exchanger is angled relative to the incoming airflow,* (2014).

[14] R. Gilbey, H. Garner, A. Condeminas, E. Boyd, K. Burgin, J. Dovey, J. Flower, A. Hipp, R. Jordan, J. Kloos, J. Pedersen, I. Rettie, R. Sanderson, A. Sewell, F. Stanhope, and H. Vogel, *ESDU 86002 Drag and Pressure Recovery Characteristics of Auxiliary Air Inlets at Subsonic Speeds CONTENTS - Amendment D*, Tech. Rep. (ESDU, 2004).

[15] F. M. White, C. Ng, and S. Saimek, *Fluid Mechanics* (McGraw Hill, 2011).

[16] L. R. Reneau, J. P. Johnston, and S. J. Kline, *Performance and Design of Straight, Two-Dimensional Diffusers,* Journal of Basic Engineering **89**, 141 (1967).

[17] G. Sovran and E. Klomp, *Experimentally Determined Optimum Geometries for Rectilinear Diffussers with Rectangular Conical or Annular Cross Section*, Tech. Rep. (General Motors Research Laboratories, 1968).

[18] ONERA, *Onera dragon concept,* Youtube (2019), screenshot taken from Youtube image.

[19] M. R. Nichols, *Investigation of Flow Trough an Intercooler Set at Various Angles to the Supply Duct*, Tech. Rep. (National Advisory Committee for Aeronautics, 1942).

[20] J. Seddon and E. L. Goldsmith, *Intake Aerodynamics: an Account of the Mechanics of Flow in and Around the Air Intakes of Turbine-engined and Ramjet Aircraft and Missiles* (Collins, 1985) p. 442.

[21] F. Yin and A. G. Rao, *Performance analysis of an aero engine with inter-stage turbine burner,* The Aeronautical Journal **121**, 1605–1626 (2017).

[22] S. Lecompte, H. Huisseune, M. V. D. Broek, B. Vanslambrouck, and M. D. Paepe, *Review of organic rankine cycle (orc) architectures for waste heat recovery,* Renewable and Sustainable Energy Reviews **47** (2015).

[23] P. Schmollgruber, D. Donjat, M. Ridel, I. Cafarelli, O. Atinault, C. François, and B. Paluch, *Multidisciplinary design and performance of the onera hybrid electric distributed propulsion concept (dragon),* (American Institute of Aeronautics and Astronautics Inc, AIAA, 2020) pp. 1–27.

[24] B. Gothert, *The drag of Airplane Radiators with Special References to Air Heating,* Tech. Rep. 896 (National Advisory Committee for Aeronautics, 1939).

[25] S. Jafari and T. Nikolaidis, *Thermal management systems for civil aircraft engines: Review, challenges and exploring the future,* Applied Sciences **8** (2018).

[26] B. T. Schiltgen, J. L. Freeman, and D. W. Hall, *Aeropropulsive interaction and thermal system integration within the eco-150: A turboelectric distributed propulsion airliner with conventional electric machines,* (American Institute of Aeronautics and Astronautics Inc, AIAA, 2016) pp. 1–18.

[27] M. Drela, *Aerodynamics of heat exchangers for high-altitude aircraft,* Journal of Aircraft **33**, 176 (1996).

[28] L. Piancastelli, L. Frizziero, and G. Donnici, *The meredith ramjet: An efficient way to recover the heat wasted in piston engine cooling,* ARPN Journal of Engineering and Applied Sciences **10** (2015).

[29] E. M. Greitzer, C. S. Tan, and M. B. Graf, *Internal Flow: Concepts and Applications* (Cambridge University Press, 2014).

[30] M. J. Moran, H. N. Shapiro, D. D. Boettner, and M. B. Bailey, *Fundamentals of Engineering Thermodynamics Eighth Edition,* 8th ed. (Wiley, 2014).

[31] A. Scoccimarro, *Preliminary design methods for the thermal management of fuel cell powered aeroengines,* Tech. Rep. (2023).

[32] E. Crosthwait, I. Kennon, and H. Roland, *Preliminary Design Methodology for Air-induction Systems* (Systems Engineering Group, Research and Technology Division, Air Force Systems Command, 1967).

[33] P. Malan and E. C. Brown, *Inlet drag prediction for aircraft conceptual design,* Journal of Aircraft **31**, 616 (1994).

[34] W. J. Bräunling, *Flugzeugtriebwerke: Grundlagen, Aero-Thermodynamik, Ideale und Reale Kreisprozesse, Thermische Turbomaschinen, Komponenten, Emissionen und Systeme* (Springer, Berlin, Germany, 2015).

[35] J. R. Henry, S. W. Wilbur, and W. C. C., *Summary of Subsonic-Diffuser Data,* Tech. Rep. (National Advisory Committee for Aeronautics, 1965).

[36] J. D. Mattingly, W. H. Heiser, and D. T. Pratt, *Aircraft Engine Design, Second Edition* (American Institute of Aeronautics and Astronautics, Inc., 2002).

[37] F. Pittaluga, *A set of correlations proposed for diffuser performance prediction,* Mechanics Research Communications **8**, 161 (1981).

[38] J. John, *Gas Dynamics,* Allyn and Bacon series in mechanical engineering (Allyn and Bacon, 1969).

[39] W. M. Kays and A. L. London, *Compact Heat Exchangers (3rd Edition)* (Scientific International, 2018).

[40] P. Walsh and P. Fletcher, *Gas Turbine Performance* (John Wiley & Sons, Ltd, 2004).

[41] B. Zohuri, *Compact Heat Exchangers Selection, Application, Design and Evaluation* (Springer, 2017).

[42] D. Sekulic, *Compact heat exchangers,* (Springer International Publishing, 2017) pp. 1–20.

[43] W. X. Chu, K. Bennett, J. Cheng, Y. T. Chen, and Q. W. Wang, *Thermo-hydraulic performance of printed circuit heat exchanger with different cambered airfoil fins,* Heat Transfer Engineering **41**, 708 (2020).

[44] D. Bacellar, V. Aute, O. Abdelaziz, and R. Radermacher, *Design of novel air-to-refrigerant heat exchangers using approximation assisted optimization,* in *ASME 2014 Verification & Validation Symposium* (2014).

[45] D. Bacellar, V. Aute, Z. Huang, and R. Radermacher, *Design optimization and validation of high-performance heat exchangers using approximation assisted optimization and additive manufacturing,* Science and Technology for the Built Environment **23**, 896 (2017).

[46] H. Kang, U. Han, H. Lim, H. Lee, and Y. Hwang, *Numerical investigation and design optimization of a novel polymer heat exchanger with ogive sinusoidal wavy tube,* International Journal of Heat and Mass Transfer **166** (2021).

[47] J. D. Domingos, *Analysis of complex assemblies of heat exchangers,* International Journal of Heat and Mass Transfer **12**, 537 (1969).

[48] A. Pignotti and P. I. Tamborenea, *Thermal Effectiveness of Multiple Shell and Tube Pass TEMA E Heat Exchangers,* Journal of Heat Transfer **110**, 54 (1988).

[49] H. Darcy, *Les fontaines publiques de la ville de Dijon exposition et application... par Henry Darcy* (Victor Dalmont, 1856).

[50] A. Hazen, *Some physical properties of sands and gravels, with special reference to their use in filtration.* (1893).

[51] A. Dupuit, *Etudes theoriques et pratiques sur le mouvement des aux dans les canaux decouverts les terrains permeables,* Victor Dalmount, Paris (1863).

[52] M. Musto, N. Bianco, G. Rotondo, F. Toscano, and G. Pezzella, *A simplified methodology to simulate a heat exchanger in an aircraft's oil cooler by means of a porous media model,* Applied Thermal Engineering **94**, 836 (2016).

[53] K. Hooman and H. Gurgenci, *Porous medium modeling of air-cooled condensers,* Transport in Porous Media **84**, 257 (2010).

[54] S. Ahlinder, *On Modelling of Compact Tube Bundle Heat Exchangers as Porous Media for Recuperated Gas Turbine Engine Applications Cottbus zur Erlangung des akademischen Grades eines DoktorIngenieurs vorgelegt von*, Ph.D. thesis, Brandenburgischen Technischem Universität Cottbus (2006).

[55] Z. zhong Li, Y. dong Ding, Q. Liao, M. Cheng, and X. Zhu, *An approach based on the porous media model for numerical simulation of 3d finned-tubes heat exchanger,* International Journal of Heat and Mass Transfer **173** (2021).

[56] B. A. amd J.L. Lage, *A general two-equation macroscopic turbulence model for incompressible flow in porous media,* International Journal of Heat and Mass Transfer **40**, 3013 (1997).

[57] G. Laruelle, *Icas 2002 congress air intakes: Role, constraints and design,* (2002).

[58] P. C. Simon and K. L. Kowalski, *Charts of Boundary-layer Mass Flow and Momentum for Inlet Performance Analysis*, Tech. Rep. (National Advisory Committee for Aeronautics, 1955).

[59] M. Rütten, L. Krenkel, and M. Freund, *Parametric design, comparison and evaluation of air intake types for bleedless aircraft,* (American Institute of Aeronautics and Astronautics Inc., 2009).

[60] J. L. Frank and R. A. Taylor, *Comparison of Drag, Pressure Recovery, and Surface Pressure of a Scoop Type Inlet and an NACA Submerged Inlet at Transonic Speeds*, Tech. Rep. (National Advisory Committee for Aeronautics, 1951).

[61] M. Sinnett, *787 no-bleed systems,* (2007).

[62] A. Lambe and J. Martins, *A unified description of mdo architectures,* in *9th World Congress on Structural and Multidisciplinary Optimization* (2011).

[63] F. Beltrame, D. Krempus, P. Colonna, and C. de Servi, *Reduced order modelling of optimized heat exchangers for maximum mass-specific performance of airborne orc waste heat recovery units,* in *7th International Seminar on O.R.C. Power Systems* (2023).

[64] P. Virtanen, R. Gommers, T. E. Oliphant, M. Haberland, T. Reddy, D. Cournapeau, E. Burovski, P. Peterson, W. Weckesser, J. Bright, S. J. van der Walt, M. Brett, J. Wilson, K. J. Millman, N. Mayorov, A. R. J. Nelson, E. Jones, R. Kern, E. Larson, C. J. Carey, İ. Polat, Y. Feng, E. W. Moore, J. VanderPlas, D. Laxalde, J. Perktold, R. Cimrman, I. Henriksen, E. A. Quintero, C. R. Harris, A. M. Archibald, A. H. Ribeiro, F. Pedregosa, P. van Mulbregt, and SciPy 1.0 Contributors, *SciPy 1.0: Fundamental Algorithms for Scientific Computing in Python,* Nature Methods **17**, 261 (2020).

[65] GREThh, *Echtherm,* .

[66] S. Hickel, *Lecture notes in computational fluid dynamics for aerospace engineers,* (2022).

[67] F. R. Menter, *Two-equation eddy-viscosity turbulence models for engineering applications,* AIAA Journal **32**, 1598 (1994).

[68] I. H. Bell, J. Wronski, S. Quoilin, and V. Lemort, *Pure and pseudo-pure fluid thermophysical property evaluation and the open-source thermophysical property library coolprop,* Industrial & Engineering Chemistry Research **53**, 2498 (2014), http://pubs.acs.org/doi/pdf/10.1021/ie4033999 .

[69] P. J. Roache, *Verification of codes and calculations,* AIAA Journal **36**, 696 (1998).

[70] I. B. Celik, U. Ghia, P. J. Roache, C. J. Freitas, H. Coleman, and P. E. Raad, *Procedure for Estimation and Reporting of Uncertainty Due to Discretization in CFD Applications,* Journal of Fluids Engineering **130**, 078001 (2008).

[71] D. Krempus, F. Beltrame, M. Majer, C. D. Servi, R. Vos, and P. Colonna, *Orc waste heat recovery system for the turboshaft engines of turbo-electric aircraft.* in *aerospace Europe Conference 2023, Vol.10th EUCASS, 9th CEAS* (2023).